Unconventional Control of Electromagnetic Waves with Applications in Electrically Small Antennas, Nondiffracting Waves, and Metasurfaces

by

Nikolaos Chiotellis

A dissertation submitted in partial fulfillment
of the requirements for the degree of
Doctor of Philosophy
(Electrical Engineering)
in the University of Michigan
2019

Doctoral Committee:

Professor Anthony Grbic, Chair
Associate Professor Ehsan Afshari
Professor David Blaauw
Associate Research Scientist Adib Nashashibi
Assistant Professor Bogdan Ioan Popa

Nikolaos Chiotellis

nchiot@umich.edu

ORCID iD: 0000-0001-8154-308X

©Nikolaos Chiotellis 2019

To everyone that accompanied me in this amazing journey
and made it a part of my life I will fondly look back on

ACKNOWLEDGMENTS

First and foremost, I would like to thank my advisor, Professor Anthony Grbic, for giving me the opportunity to work with him and for his mentorship throughout the years. I truly admire his work ethic, his determination and endurance, and his unique ability to inspire students during the inadvertent lows of the PhD degree. He has opened doors for me I could never have dreamt of.

I also want to acknowledge the members of my thesis committee: Associate Professor Ehsan Afshari, Professor David Blaauw, Associate Research Scientist Adib Nashashibi, and Assistant Professor Bogdan Ioan Popa. Their useful suggestions, comments and remarks made this dissertation better and more complete.

I would also like to acknowledge the numerous people I have crossed paths with throughout my education: school teachers, college professors, classmates, coworkers, collaborators, and the RadLab family. They have imparted me with a piece of their vast knowledge, without which this dissertation would not have been possible.

On a personal level, I would like to thank my mother, Anastasia, for her immense sacrifices that have made me the person I am today. She has done everything in her power to open up a wide array of possibilities to my sister and me. She has always been there for us, not caring about anything else other than our well-being. All of our successes can be ultimately traced back to her. My sister, Christina, has always motivated me to be the best person I can be, and achieve whatever I set my eye on. Her integrity, perseverance, and honesty really make her stand out.

I want to thank all the friends I have made throughout the years, both in Greece as well as in the US, for everything we have been through together. I hope I have been able to give back to them as much as they have given me. I consider them to be the crown jewels of my life, and the fact that I am in their lives my greatest accomplishment.

Finally, I would like to thank my fiancée, Liz, for her endless support and for making my life better in so many different ways. I never imagined I would find a partner that is so loving, generous, and caring. My time with her has been magical, and I am looking forward to soon opening up a new chapter in our shared life.

TABLE OF CONTENTS

LIST OF FIGURES

LIST OF TABLES

LIST OF APPENDICES

LIST OF ABBREVIATIONS

AFE Analog Front-end

ESA Electrically Small Antenna

GPS Global Positioning System

IML Impedance Matching Layer

IoT Internet of Things

ISM Industrial, Scientific and Medical

MoM Method of Moments

MRR Medium Range Radio

PCB Printed Circuit Board

PEC Perfect Electric Conductor

PV Photovoltaic

QCTO Quasiconformal Transformation Optics

TE Transverse Electric

TM Transverse Magnetic

ABSTRACT

Although electromagnetics is a well-established field within physics and engineering, it is also a rather dynamic one. Our ever increasing need for connectivity and the rise of medical and military applications constantly create new challenges for researchers in electromagnetics. In this thesis, unconventional methods are proposed for tackling some of these challenges by manipulating the electromagnetic fields in different regions: reactive near field, radiative near field, and far field.

The first topic examined pertains to the development of antennas for Internet of Things (IoT) nodes with extremely small form factors and low power consumption. As a result, they require small and relatively efficient antennas that can be tightly integrated within the node. The antennas should be able to operate with lossy and metallic components in their near field, while maintaining adequate performance. A type of antenna, called a 3D loop, is designed to fulfill these specifications, and is used in two compact IoT systems.

The second thrust aims at developing devices that generate Bessel beams and X waves in their radiative near field. Bessel beams are a class of exotic beams with nondiffracting and self-healing properties. Here, two radiator designs are presented, capable of generating Bessel beams with minimal deviation of their parameters over a broad bandwidth. This allows the generation of nondiffracting and nondispersive pulses (X waves) that remain highly localized within the device's radiative near field.

The final topic examined aims at analytically modeling the electromagnetic properties of patterned metallic sheets. Such sheets are the building blocks of metasurfaces, which are two dimensional devices that manipulate the properties of a propagating wavefront (amplitude, phase, polarization). Having analytical models for sheets that realize arbitrary

electromagnetic properties significantly expedites their design, as opposed to relying on databases of simulated geometries.

CHAPTER 1

Introduction

In this thesis, we present unconventional methods to solve modern problems in electromagnetics. Our research efforts have focused on three topics, each requiring the manipulation of electromagnetic fields in a different region (reactive near field, radiative near field, and far field). To a large degree, the progress reported here is enabled by recent advancements in electronics, materials, and fabrication techniques.

1.1 Electrically Small Antennas

1.1.1 Background

An Electrically Small Antenna (ESA) is any antenna that has a small size compared to the wavelength of radiation. ESAs have been extensively studied in the past [1, 2]. Although the advantages of using an antenna that occupies a small volume or area are obvious, it is also known that their performance is fundamentally limited when their size becomes a small fraction of the operating wavelength [3]. Significant attention has been given to their quality factor, a quantity that is inversely proportional to the bandwidth of operation [4]. This is known as the Chu limit [5]. For narrowband applications, however, a more important parameter is the radiation efficiency of the antenna, which describes the ratio of radiated power to the power accepted by the antenna.

The already limited performance of ESAs is further degraded due to their integration within compact systems. The introduction of external components within the extreme near field of the antenna has a significant impact on its radiation efficiency, especially when the components are made either from lossy dielectrics or metals having high conductivity. The combination of inherent limitations of ESAs with the loss in performance from external components restricts the range over which these systems can operate. As a result, the engineer needs to choose the most appropriate antenna and carefully examine its placement in the system.

While developing compact systems requires us to overcome significant difficulties, there is a growing demand for such systems [6]. The advancement of Internet of Things (IoT) in recent years creates a need for small devices that are able to communicate wirelessly. Their use ranges from tags to sensors, and from location tracking devices to wearables. These devices should be able to communicate with a centralized node (a gateway) efficiently in order to exhibit adequate range and battery life.

1.1.2 Motivation

The work presented here is one part of a larger collaborative effort between research groups at the University of Michigan to build ultra low power IoT nodes that are able to communicate with a gateway and transmit low data rate information to it [7, 8, 9] or for location tracking [10, 11, 12]. The main challenge addressed here is designing efficient antennas with extremely small form factors that can operate in an adverse near field environment (in the presence of lossy or metallic components).

Two elementary antennas are examined first: an electric dipole (straight wire), and a magnetic dipole (loop). Analytical and simulation results are compared for the two antennas to deduce which one suits the application better. Once it is found that magnetic dipoles have superior performance, a variation of them, the 3D loop, is developed. These loops can be fabricated using standard Printed Circuit Board (PCB) techniques and can be assembled with the other components of the system in a straightforward fashion. Their performance is not degraded significantly by the presence of these components in their near field. The use of these antennas is showcased in two applications: a Global Positioning System (GPS) receiver (1.575 GHz), and an Industrial, Scientific and Medical (ISM) band transceiver (915 MHz) for low bit rate communication in an indoor environment.

1.1.3 Goals

The goals of this work are:

- To determine which type of ESA (electric or magnetic dipole) performs better for mm-scale and cm-scale IoT nodes.
- To develop a variation of magnetic dipoles (which are found to perform better in this framework) that can be integrated within the IoT node with acceptable performance.
- To perform parametric studies to determine the tradeoffs between size and radiation efficiency.

- To design and experimentally validate an ESA for a GPS receiver with dimensions $10 \times 10 \times 6$ mm^3.
- To design and experimentally validate an ESA for an IoT node with dimensions $3.41 \times 3.62 \times 3.8$ mm^3, after determining which ISM band is the most suitable for this specific application.

1.1.4 Publications

This work was presented in the following published or submitted articles:

1. **N. Chiotellis**, L.-X. Chuo, H. Kim, Y. Chen, H.-S. Kim, D. D. Wentzloff, D. Blaauw, and A. Grbic, "Electrically small loop antennas for compact IoT devices," *under review*.
2. H. Kim, **N. Chiotellis**, E. Ansari, M. Faisal, T. Jang, A. Grbic, H.-S. Kim, D. Blaauw, and D. D. Wentzloff, "A receiver/antenna co-design for a 1.5 mJ per fix fully-integrated 10x10x6mm^3 GPS logger," in *Custom Integrated Circuits Conference (CICC), 2018 IEEE*. IEEE, 2018, pp. 1-4.
3. T. Jang, G. Kim, B. Kempke, M. B. Henry, **N. Chiotellis**, C. Pfeiffer, D. Kim, Y. Kim, Z. Foo, H. Kim, A. Grbic, D. Sylvester, H.-S. Kim, D. D. Wentzloff, and D. Blaauw, "Circuit and system designs of ultra-low power sensor nodes with illustration in a miniaturized GNSS logger for position tracking: Part II - Data communication, energy harvesting, power management, and digital circuits," *IEEE Transactions on Circuits and Systems I: Regular Papers*, vol. 64, no. 9, pp. 2250-2262, 2017.
4. T. Jang, G. Kim, B. Kempke, M. B. Henry, **N. Chiotellis**, C. Pfeiffer, D. Kim, Y. Kim, Z. Foo, H. Kim, A. Grbic, D. Sylvester, H.-S. Kim, D. D. Wentzloff, and D. Blaauw, "Circuit and system designs of ultra-low power sensor nodes with illustration in a miniaturized GNSS logger for position tracking: Part I - Analog circuit techniques," *IEEE Transactions on Circuits and Systems I: Regular Papers*, vol. 64, no. 9, pp. 2237-2249, 2017.
5. L.-X. Chuo, Y. Shi, Z. Luo, **N. Chiotellis**, Z. Foo, G. Kim, Y. Kim, A. Grbic, D. D. Wentzloff, H.-S. Kim, and D. Blaauw, "7.4 A 915MHz asymmetric radio using Q-enhanced amplifier for a fully integrated 3x3x3mm^3 wireless sensor node with 20m non-line-of-sight communication," in *Solid-State Circuits Conference (ISSCC), 2017 IEEE International*. IEEE, 2017, pp. 132-133.

6. Y. Chen, **N. Chiotellis**, L.-X. Chuo, C. Pfeiffer, Y. Shi, R. G. Dreslinski, A. Grbic, T. Mudge, D. D. Wentzloff, D. Blaauw, and H.-S. Kim, "Energy-autonomous wireless communication for millimeter-scale Internet-of-Things sensor nodes," *IEEE Journal on Selected Areas in Communications*, vol. 34, no. 12, pp. 3962-3977, 2016.

1.2 Nondiffracting Waves

1.2.1 Background

Nondiffracting waves get their name from their rather interesting nondiffracting property, which means that their intensity does not diminish as they propagate [13]. Nondiffracting waves produced by finite apertures are inherently a radiative near field effect. In other words, they maintain their nondiffracting property within a specific distance, called the nondiffracting range.

Researchers have theoretically predicted and experimentally realized multiple classes of nondiffracting waves that will be reviewed in Chapter 3 [14, 15, 16, 17]. Our attention has mostly focused on a class of nondiffracting waves called Bessel beams [18]. These beams take their name from the Bessel functions that mathematically describe them. Bessel functions are well-known solutions to differential equations, including the Helmholtz equation in cylindrical coordinates. Bessel beams have also been shown to be self-healing, meaning that they recover their field profile after encountering an obstacle [13].

Bessel beams have been extensively studied in terms of theory. Experimentally, however, there have only been a few demonstrations so far, and most of them were done at optical frequencies [19, 20, 21, 22, 23, 24, 25, 26, 27]. Bessel beams are challenging to generate at microwave frequencies because of the size of the equipment needed (often involving separate antenna and lensing systems). At the same time, Bessel beams and their time domain counterparts, Bessel pulses and X waves, have been shown to have numerous applications, including medical ultrasonic imaging, tissue characterization, nondestructive evaluation of materials [28], optical conveyors [29], electron microscopy [30], microfabrication of dielectrics [31], exerting forces on biological cells [32], and optical communications [33].

1.2.2 Motivation

Nondiffracting waves are examined to demonstrate control of electromagnetic waves in the radiative near field (Fresnel zone). We introduce two new methods of generating Bessel

beams at microwave frequencies. The first Bessel beam radiator developed is based on refractive optics, while the second one employs metamaterials to achieve a similar effect and even allow paraxial Bessel beams [34, 35, 36, 37]. Both radiators exhibit a 50% fractional bandwidth.

The main contribution of this work, however, is the devices' ability to produce Bessel beams over an appreciable bandwidth with little change in the beams' characteristics. This allows the generation of X waves, short localized microwave pulses that do not diffract and do not disperse, meaning that they do not spread in time [38]. X waves are composed of a spectrum of Bessel beams, which are nondiffracting. The nondispersive property is derived from the fact that all the frequency components that make up the pulse propagate with very similar characteristics [13]. Such pulses have obvious medical and military applications among others.

1.2.3 Goals

Our efforts in the field of nondiffracting waves aim at developing and experimentally validating two devices. The goals of this work can be grouped into two sets, each set pertaining to a distinct device.

1. Bessel beam and X wave radiator based on refractive optics [34, 35]:
    - To design a coaxially-fed device that generates Bessel beams using refractive optics to ensure its broad bandwidth.
    - To validate the design through full-wave simulations.
    - To fabricate the device using standard CNC machining.
    - To experimentally validate the generation of Bessel beams over a broad bandwidth.
    - To experimentally validate the generation of X waves through frequency as well as time domain measurements.
2. Bessel beam and X wave radiator based on metamaterials [36, 37]:
    - To design a coaxially-fed device that transforms the radiation of a monopole into a paraxial Bessel beam using an inhomogeneous, isotropic dielectric region.
    - To implement the inhomogeneous region using metamaterials.
    - To validate the device's performance through full wave simulations.

- To fabricate the design through 3D printing with low-loss filaments.
- To measure the device experimentally and compare the results with those obtained through simulation.

1.2.4 Publications

This work was presented in the following published articles:

1. **N. Chiotellis**, V. Mendez, S. M. Rudolph, and A. Grbic, "Experimental demonstration of highly localized pulses (X waves) at microwave frequencies," *Physical Review B*, vol. 97, no. 8, p. 085136, 2018.

2. **N. Chiotellis** and A. Grbic, "Metamaterial-based Bessel beam launcher," in Engineered Materials Platforms for Novel Wave Phenomena (Metamaterials), *2017 11th International Congress on*. IEEE, 2017, pp. 55-57.

3. **N. Chiotellis** and A. Grbic, "Metamaterial Bessel beam radiator," in *Antennas and Propagation & USNC/URSI National Radio Science Meeting, 2017 IEEE International Symposium on*. IEEE, 2017, pp. 1735-1736.

4. **N. Chiotellis** and A. Grbic, "A broadband, Bessel beam radiator," in *Antennas and Propagation & USNC/URSI National Radio Science Meeting, 2016 IEEE International Symposium on*. IEEE, 2016, pp. 873-874.

1.3 Metasurfaces

1.3.1 Background

Metasurfaces, the 2D equivalent of metamaterials, are subwavelength-textured surfaces that exhibit tailored electromagnetic properties. In recent years, they have found numerous applications that will be reviewed in an upcoming chapter [39, 40, 41, 42, 43, 44, 45, 46, 47, 48, 49, 50, 51]. Earlier work at the University of Michigan has investigated cascaded metasurfaces, consisting of metallic claddings separated by subwavelength dielectric spacers, to implement tailored electric, magnetic, and bianisotropic responses [52, 53, 54]. Although these devices have been used in the near field of radiating devices, they are most commonly used in far field applications, meaning that the incident, reflected and transmitted waves are assumed to be plane waves.

The design of cascaded metasurfaces relies on numerically calculating the electromagnetic properties (in this case, the sheet impedance) of the metallic claddings needed to implement a specific response, e.g controlling the phase, amplitude or polarization of the transmitted wave [53]. These properties are then realized through patterning of metallic sheets. This is achieved by simulating various metallic patterns in commercial electromagnetic software and choosing the appropriate one. A small section of the sheet, called a unit cell, is simulated for each geometry, under the assumption that the sheet consists of infinite such unit cells.

Choosing the right unit cell is not an easy task, especially for inhomogeneous metasurfaces that comprise hundreds or thousands of unit cells per design [54]. The designer needs to have experience in the range of sheet impedance values that can be achieved by each unit cell geometry. When a specific geometry has been decided on, extensive parametric studies need to be performed so that the dimensions of the unit cell realizing the required sheet impedance are found. This is a laborious, time- and resource-consuming process.

1.3.1.1 Motivation

Our efforts in manipulating plane waves have focused on expediting the design process of cascaded metasurfaces by developing analytical models for multiple unit cell geometries [55]. Specifically, we have developed analytical models for the sheet impedance tensor of various general-purpose geometries under arbitrary plane wave incidence in the long wavelength (metamaterial) limit. These models accelerate the design of metasurfaces, eliminating the need for extensive databases of unit cells.

A variety of unit cells are studied. In some of the unit cells, lumped components have been included, which broaden the range of sheet impedance values that can be achieved. These lumped components can be implemented in a distributed fashion using meandered lines for inductors and gaps for capacitors. Moreover, all geometries studied allow for non-diagonal components in the sheet impedance tensor. These are required in order to realize metasurfaces that exhibit cross polarizing effects. The models also take into account the angle of incidence and polarization of the incident wave, which widens their scope. Using these unit cells, arbitrary sheet impedance tensors can be realized.

The developed models are used to realize two metasurfaces for polarization control operating at 10 GHz: an asymmetric linear polarizer and a polarization rotator. The systematic approach for their implementation is presented, from ideal sheet impedances to patterned metallic sheets separated by dielectric spacers. Using the analytical models, the design process is rapid.

1.3.1.2 Goals

The goals of this work are:

- To develop analytical models for the sheet impedance of various unit cells consisting of metallic strips, and lumped components.
- To develop analytical models for complementary geometries through the use of Babinet's principle in tensorial form.
- To confirm the validity of these models by comparing them to simulation results of the same geometry.
- To use the developed models to design metasurfaces that manipulate the polarization of plane waves.

1.3.2 Publications

This work was presented in the following published articles:

1. **N. Chiotellis** and A. Grbic, "Analytical modeling of tensor metasurfaces," *JOSA B*, vol. 33, no. 2, pp. A51-A60, 2016.
2. **N. Chiotellis** and A. Grbic, "Towards the analytical design of bianisotropic metasurfaces," in *6th International Conference on Metamaterials, Photonic Crystals and Plasmonics META 2015*, pp. 1185-1186.
3. **N. Chiotellis** and A. Grbic, "Towards the analytical design of tensor metasurfaces," in *Antennas and Propagation & USNC/URSI National Radio Science Meeting, 2015 IEEE International Symposium on*. IEEE, 2015, pp. 1094-1095.

1.3.3 Thesis Outline

This thesis is divided into 6 chapters. Chapter 1 serves as an introduction to the research work outlined in this thesis.

Chapter 2 presents a class of ESAs for compact IoT nodes. Two elementary radiators are examined in this framework, an electric dipole (linear wire) and a magnetic dipole (loop). Analytical and simulation results on their radiation efficiency are given as a function of their size. It is found that magnetic dipoles perform better when the antenna size

is extremely small and the losses of the required matching components are taken into account. Based on this knowledge, the 3D loop is developed, which is compatible with standard PCB techniques. Having two solid metal sides, the 3D loop can be easily integrated with other system components, e.g. chips, batteries, or Photovoltaic (PV) cells, without a significant loss in performance. As a result, it is suitable for use in compact IoT nodes. Two such systems using 3D loops are outlined: a GPS receiver (1.575 GHz), and an ISM band transceiver (915 MHz). Simulation and experimental results on these two systems are compared.

Chapter 3 investigates the design of the Bessel beam radiator based on refractive optics. After the principle of operation is explained, simulation results showing the validity of this approach are presented. Experimental results from a fabricated prototype are also given, showing close agreement to simulation results and confirming the generation of Bessel beams at microwave frequencies. The device's ability to generate X waves is explored next, using experimental results in both the frequency and time domains.

Chapter 4 presents the Bessel beam radiator that employs metamaterials. The design process, based on Quasiconformal Transformation Optics (QCTO), is outlined first. Through this process, we obtain the dielectric constant profile of an inhomogeneous, isotropic dielectric region. This region is implemented using metamaterials, and, specifically, unit cells that are rotationally symmetric. Simulations are performed to verify that the metamaterial implementation yields the same results as the dielectric constant profile obtained through QCTO. The device is fabricated through 3D printing using multiple low-loss filaments. The fabricated prototype is experimentally measured, verifying that its performance agrees with simulation results, and validates the design procedure. Its ability to emit X waves is also verified.

Chapter 5 investigates the analytical modeling of the sheet impedance tensor of patterned metallic sheets used in cascaded metasurfaces. A simple unit cell, consisting of two metallic strips that intersect at an arbitrary angle, is studied first. Once its sheet impedance has been calculated, expressions are given for the sheet impedance of the same geometry where the strips are loaded with lumped components. The complementary geometry, which resembles a parallelogram patch, is also analyzed through the use of Babinet's principle. A unit cell consisting of three intersecting metallic strips and its loaded counterpart are studied next. Using these models and interpolation, the sheet impedance tensor of a more complicated unit cell, the sliced patch, is modeled. The derived expressions are compared to results obtained through simulation, and close agreement is observed in the long wavelength limit. Two cascaded metasurfaces that manipulate the polarization of plane waves at 10 GHz are designed using these models: an asymmetric linear polarizer, and a polarization

rotator.

Finally, concluding remarks are presented in Chapter 6.

CHAPTER 2

Electrically Small Antennas

In this chapter, the work performed on electrically small antennas is presented. The antennas are designed to maximize radiation efficiency. They are also specifically designed in such a way that other components placed on top or bottom (batteries, PV cells, chips, etc.) do not limit the antennas' ability to radiate. As a result, the antennas maintain their performance when stacked vertically within a volume-constrained system.

2.1 Chapter Introduction and Outline

The Internet of Things (IoT) is a global infrastructure for the information society, enabling advanced services by interconnecting physical and virtual objects based on existing and evolving interoperable information and communication technologies [56]. It is expected that by 2020, there will be $21 - 31$ billion IoT devices worldwide [6]. In terms of hardware, this translates into a need for smaller and more efficient devices that provide ubiquitous information and/or connectivity in a non pervasive manner. Antennas are integral to any wireless communication system while oftentimes being the single largest component in a wireless device. As a result, there is a growing demand for small antennas, tightly integrated within compact devices.

Depending on the size and frequency specifications of a system, the use of an ESA is sometimes required. Such antennas exhibit ka values less than 0.5, where k is the free space wavenumber and a is the smallest radius of a fictitious sphere enclosing the antenna [57]. Due to their small size, ESAs face significant limitations in terms of bandwidth, input impedance, and radiation efficiency among other characteristics [3].

Chu [5] developed expressions relating the minimum quality factor, Q, to the electrical size of an antenna, ka [57]:

$$Q = \frac{1}{(ka)^3}, \quad ka \ll 1. \tag{2.1}$$

The quality factor is inversely proportional to the bandwidth of the antenna, Δf:

$$Q = \frac{f_0}{\Delta f}, \tag{2.2}$$

where f_0 is the center frequency. This limit stipulates the maximum bandwidth for a given electrically-small size, or the smallest size for a given bandwidth.

The applications considered in this chapter are inherently narrowband, so bandwidth (or, equivalently, the Q-factor of the antenna) is not a major concern. Here, focus is placed on input impedance and efficiency, which can severely reduce the received/transmitted power. Fundamental limits on the efficiency of metallic ESAs have recently been examined [58].

Apart from these limitations that are intrinsic to ESAs, the overall performance of the communication system may also be degraded by the placement of the antenna. A way to minimize the volume of a system without sacrificing functionality is to vertically integrate its components [59]. This concept, originally developed for integrated circuits, can be applied to entire communication systems, consisting of circuits, antennas, batteries as well as other components. From an antenna perspective, this introduces the challenge of radiating between components that contain metallic surfaces or lossy dielectrics.

Using electrically-small electric and magnetic dipoles as the starting point, it will be shown how magnetic dipoles (loops) can provide superior performance once the losses inherent to impedance matching components are factored in (Sec. 2.2). A method for incorporating small 3D loops into compact cm- and mm-scale vertically integrated systems will be presented in Sec. 2.3. This method is compatible with PCB manufacturing techniques, making the antenna fabrication affordable and reliable. Based on this approach, the design of a differentially-fed, linearly polarized antenna for a cm-scale GPS receiver will be outlined in Sec. 2.4. The design of an extremely small 3D loop antenna will be shown in Sec. 2.5, intended for a mm-scale IoT device. In both cases, details of the system are also given. Finally, concluding remarks will be made in Sec. 2.6.

2.2 Electric vs Magnetic Dipoles

A comparison between mm-scale electric and magnetic dipoles will be presented in this section. The two antenna types will be compared in terms of their efficiency when they are non-resonant, as well as when a lumped component is used to achieve resonance (cancel out the imaginary part of their input impedance). It will be shown that magnetic dipoles perform better than electric ones, once the losses of lumped components needed for reso-

nance are taken into account.

2.2.1 Radiation efficiency of non-resonant dipoles

The radiation resistance of a small electric dipole (linear wire) with length l and wire with radius $b \ll l$ [57, 3] is

$$R_{e,R} \approx 5\,(kl)^2\,, \tag{2.3}$$

where k is the wavenumber. Its ohmic resistance is

$$R_{e,L} \approx \frac{l}{4\pi b\delta\sigma}, \tag{2.4}$$

where σ is the conductivity of the material in the wire and $\delta = \sqrt{\frac{2}{\sigma\omega\mu}}$ is the skin depth (ω denotes the angular frequency and μ denotes the permeability of the material). For copper, $\sigma = 5.8 \times 10^7$ S/m, and $\mu = \mu_0 = 4\pi \times 10^{-7}$ H/m.

The radiation efficiency of the electric dipole is

$$\eta_e = \frac{R_{e,R}}{R_{e,R} + R_{e,L}}. \tag{2.5}$$

The corresponding quantities for a small magnetic dipole (loop) of radius r using wire with radius $b \ll r$ are:

$$R_{m,R} \approx 20\pi^2\,(kr)^4\,, \tag{2.6}$$

$$R_{m,L} \approx \frac{r}{b\delta\sigma}, \tag{2.7}$$

$$\eta_m = \frac{R_{m,R}}{R_{m,R} + R_{m,L}}. \tag{2.8}$$

Values for η_e and η_m are presented in Fig. 2.1(a) and (b), respectively. The frequency range is chosen to be between 0.5 and 6 GHz and the wire radius is $b = 0.2$ mm. The length of the electric dipole assumes values between 1.5 and 10 mm. The radius of the magnetic dipole assumes values between 0.75 and 5 mm, so that the antennas have the same a values. The black curve signifies the electrically small limit ($ka < 0.5$). The radiation efficiency of electric dipoles, η_e, is significantly higher than that of magnetic dipoles, η_m, of comparable size.

The two dipole configurations are also simulated in ANSYS Electronics Desktop (for-

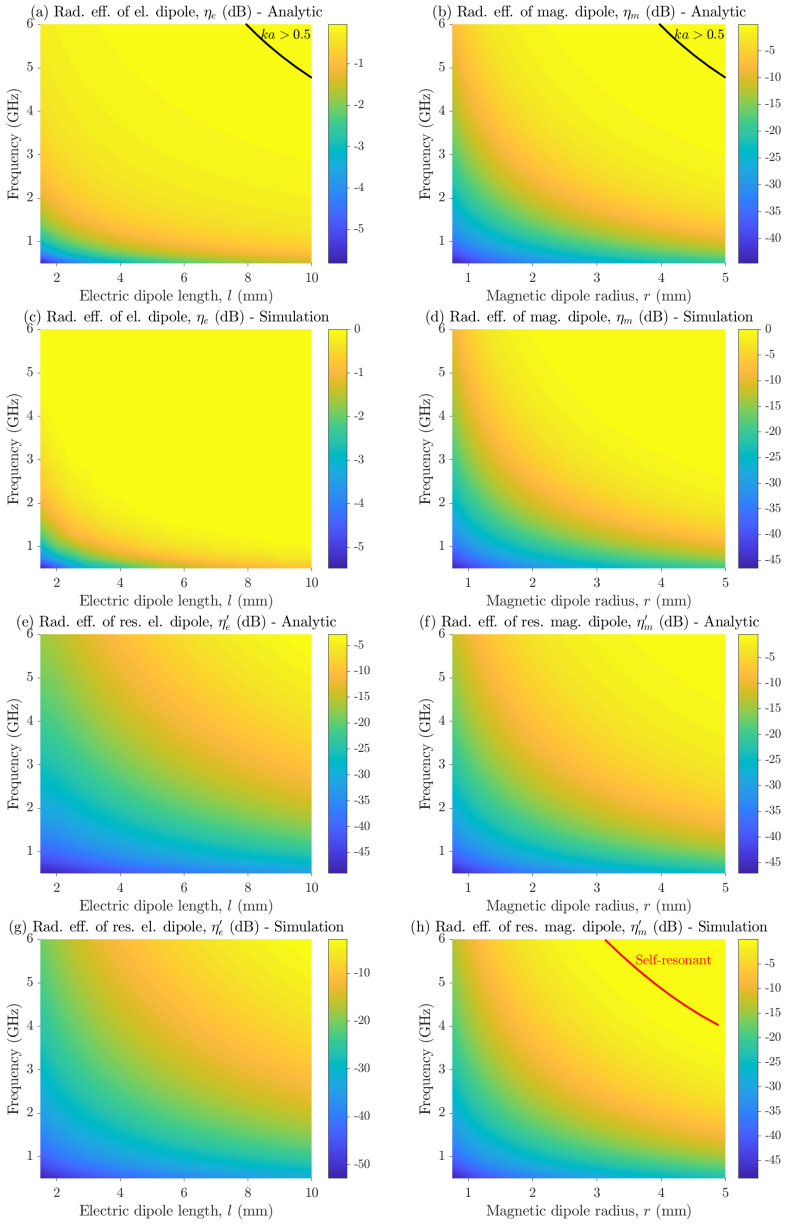

Figure 2.1: (a-b) Radiation efficiency of electric and magnetic dipoles as a function of size and frequency using the analytical formulation. The black curve corresponds to the electrically small limit: $ka < 0.5$. (c-d) Radiation efficiency of electric and magnetic dipoles using simulation results. (e-f) Radiation efficiency of resonant (zero input reactance) electric and magnetic dipoles using the analytical formulation. (g-h) Radiation efficiency of resonant electric and magnetic dipoles using simulation results. The red curve corresponds to the radius-frequency limit above which the loops are self-resonant.

merly HFSS). A gap of 0.2 mm is made in the wire to place the lumped port that excites the dipoles. The resulting values for η_e and η_m are presented in Fig. 2.1(c) and (d), respectively. Quite good agreement is observed between the analytical and simulation results.

2.2.2 Radiation efficiency of resonant dipoles

The input reactance of a small electric dipole is [57]

$$X_e \approx -120 \frac{\ln\left(\frac{l}{2b}\right) - 1}{\tan\left(\frac{kl}{2}\right)}. \tag{2.9}$$

In order to make the small electric dipole resonant, an inductor is required to cancel out its negative reactance. Specifically, the inductance, L, needed satisfies:

$$\omega L + X_e = 0 \Rightarrow L = -\frac{X_e}{\omega}. \tag{2.10}$$

It is assumed that the inductor does not have any other parasitics except for a series resistance, $R_{e,I}$, which is related to its Q-factor, Q_I, through:

$$R_{e,I} = \frac{\omega L}{Q_I}. \tag{2.11}$$

Assuming a series connection of the inductor with the electric dipole, the dipole's radiation efficiency when it is resonant (zero input reactance) is

$$\eta_e' = \frac{R_{e,R}}{R_{e,R} + R_{e,L} + R_{e,I}}. \tag{2.12}$$

The input reactance of a small circular loop is

$$X_m = \omega \mu_0 r \left[\ln\left(\frac{8r}{b}\right) - 2\right] + \frac{r}{b\delta\sigma}. \tag{2.13}$$

In order to make the small magnetic dipole resonant, a capacitor is required to cancel out its positive reactance. Specifically, the capacitance, C, needed satisfies:

$$-\frac{1}{\omega C} + X_m = 0 \Rightarrow C = \frac{1}{\omega X_m}. \tag{2.14}$$

It is assumed that the capacitor does not have any other parasitics except for a series resistance, $R_{m,C}$, which is related to its Q-factor, Q_C, through:

$$R_{m,C} = \frac{1}{\omega C Q_C}. \tag{2.15}$$

Assuming a series connection of the capacitor with the magnetic dipole, the dipole's radiation efficiency when it is resonant (zero input reactance) is

$$\eta'_m = \frac{R_{m,R}}{R_{m,R} + R_{m,L} + R_{m,C}}. \tag{2.16}$$

Values for η'_e and η'_m are presented in Fig. 2.1(e) and (f), respectively. In the analysis, it was assumed that the Q-factor of the inductors is

$$Q_I = 50, \tag{2.17}$$

while the Q-factor for the capacitors is

$$Q_C = 250. \tag{2.18}$$

These are typical values encountered in components designed for use in the examined frequency range. In all cases, the radiation efficiency of resonant magnetic dipoles, η'_m, is higher than that of resonant electric dipoles, η'_e, of comparable size.

In simulations, the efficiency of the two dipoles when resonant is also calculated. They are presented in Fig. 2.1(g) and (h), respectively. Similar to the analytical results, the radiation efficiency of resonant magnetic dipoles, η'_m, is found to be higher than that of resonant electric dipoles, η'_e in all examined cases. The red curve in Fig. 2.1(h) denotes the radius-frequency limit above which the loop is self-resonant. Over this limit, the magnetic dipole has a negative reactance, and an inductor is needed to cancel out its reactance and make it resonant.

2.3 2D vs 3D Loops

A conventional square loop antenna is shown in Fig. 2.2(a) [60]. This antenna geometry will be referred to as the 2D loop since the loop lies on a plane. The edge of the loop has length L and the width of the metallic strip (shown in orange) is W. The 2D loop antenna is printed on a substrate with thickness H (shown in light blue) and is excited by a lumped port in the gap G (shown in black). Without loss of generality, the edge length is set to $L = 10$ mm and the substrate material is chosen as Rogers RT/duroid® 5880, with dielectric constant $\varepsilon_r = 2.2$ and loss tangent tan$\delta = 0.0009$. The gap is chosen as $G = 0.2$ mm, and the width of the strip is set to $W = 1.5$ mm.

For the chosen parallelepiped geometry used here, the radius of the enclosing sphere, a is

$$a = \sqrt{\frac{L^2}{2} + \frac{H^2}{4}}. \tag{2.19}$$

The 2D loop antenna is simulated in Ansys Electronics Desktop. The height of the substrate, H, varies from 0.127 to 6.35 mm. The radiation efficiency of the 2D loop antenna is shown in Fig. 2.2(c). The height of the substrate appears to have an insignificant effect on the antenna's radiation efficiency, as expected. The loop is primarily magnetic in its near field, and, as a result, it is not affected by the presence of the substrate. In line with intuition, the efficiency increases with increasing frequency since the loop appears electrically larger. The black curve in Fig. 2.2(c) denotes the electrically small limit.

The proposed 3D loop antenna geometry is shown in Fig. 2.2(b). A dielectric substrate in the shape of a parallelepiped with a square base of edge length L and height H is covered by copper cladding on both sides. A small gap, G, on one side is used to excite the antenna with a lumped port (shown in black). Two vias of diameter D are placed close to two corners of the antenna, as shown in the drawing. They connect the top and bottom copper layers. The 3D antenna occupies the same volume as the 2D antenna, so the two designs are comparable in terms of electrical size.

The 3D loop antenna is also simulated in ANSYS Electronics Desktop. Similar to the 2D loop, the height, H, varies from 0.127 to 6.35 mm. The gap, G and the material of the substrate are the same as for the 2D loop, while the via diameter is $D = 1.5$ mm. The radiation efficiency of the 3D loop is shown in Fig. 2.2(d). It can be easily seen that in this case, height significantly affects the radiation efficiency. Specifically, efficiency increases monotonically with height, since the area of the loop, or, equivalently, its dipole moment, increases.

The main advantage of the proposed 3D loop antenna geometry is the significant increase in radiation efficiency in systems where the substrate height can be used to optimize the antenna's performance. The dashed purple curve in Fig. 2.2(d) denotes the height-frequency limit where the 3D antenna performs better than the 2D one. The exact position of this curve depends on the antenna parameters L, D and R and the substrate material. However, it constitutes a general trend that holds for different sets of such parameters. For example, when the height is $H = 4.89$ mm and the frequency is 2 GHz, the radiation efficiency of the 2D loop is -3.41 dB, whereas that of the 3D loop is -1.54 dB. In general, when the height of the antenna can be 2.9 mm or more, the 3D loop is more efficient than the 2D loop for the chosen set of parameters.

In Fig. 2.2(e-f), the radiation efficiencies of the two loops are presented when a lumped component is used to make them resonant. The red curve in Fig. 2.2(f) corresponds to the

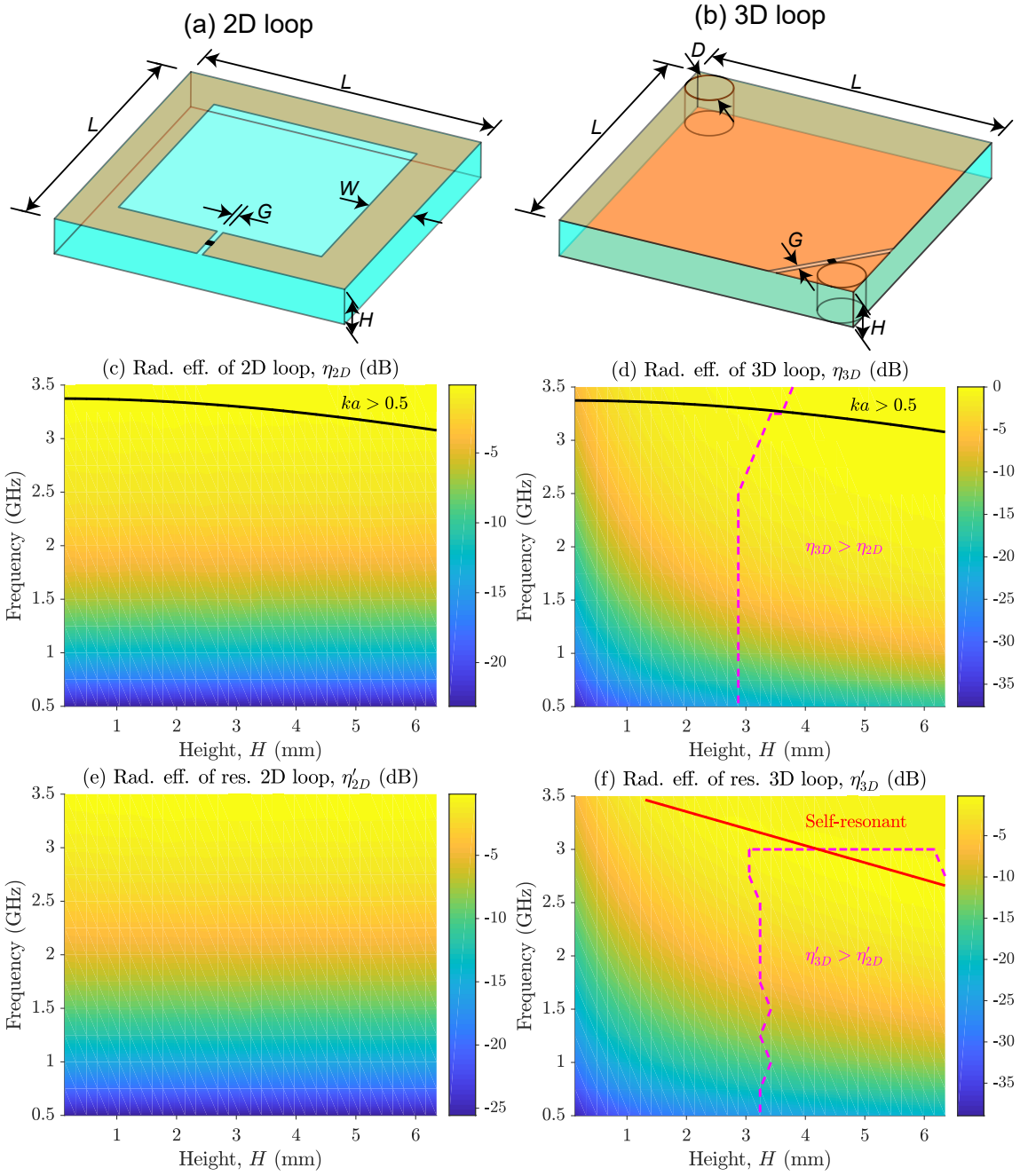

Figure 2.2: (a-b) 2D and 3D loop antenna geometries, and (c-d) their radiation efficiencies, η_{2D} and η_{3D}, as a function of frequency and height, H. The black curve corresponds to the electrically small limit: $ka < 0.5$. The dashed purple curve denotes the height-frequency limit above which the 3D loop is more efficient that the 2D loop. (e-f) Radiation efficiency of resonant 2D and 3D loops. The red curve corresponds to the height-frequency limit above which the 3D loop is self-resonant. The dashed purple curve denotes the height-frequency limit above which the resonant 3D loop becomes more efficient that the resonant 2D loop.

height-frequency limit above which the 3D loop is self-resonant, requiring an inductor to achieve resonance. The dashed purple curve in Fig. 2.2(f) denotes the height-frequency limit where the resonant 3D loop performs better than the resonant 2D loop. In general, when the height of the antenna can be 3.2 mm or more, the resonant 3D loop is more efficient than the resonant 2D loop.

The improvement in efficiency results from the fact the current can flow through a larger area in the 3D loop case, which reduces the resistive losses in the antenna. Moreover, the 3D loop antenna can prove to be beneficial in systems where components are stacked vertically instead of horizontally because the copper sheets act as a shield between the antenna and the rest of the circuit components. Finally, when placed on a horizontal ground plane, the 3D loop's far field performance benefits from the image current generated due to the current in the loop [57]. On the contrary, the 2D loop would exhibit a significant drop in radiation efficiency.

Although this geometry should be avoided in practice, the case where the 2D loop is placed between two conducting sheets is briefly investigated. This would occur when the antenna is placed between PCBs that either have continuous ground planes or appear as such due to highly dense traces on the horizontal layers facing the antenna. Specifically, the configuration in Fig. 2.3(a) is simulated, which occupies the same volume as the 2D and 3D loops (Fig. 2.2(a-b)).

Keeping all parameters the same as before, its radiation efficiency when resonant is presented in Fig. 2.3(b). Its efficiency for $H = 4.89$ mm at 2 GHz is -11.64 dB. The 3D loop (Fig. 2.2(b)), which also has metal on both sides, performs significantly better. Its efficiency, presented in Fig. 2.2(d), is higher in all examined cases. As a result, not only can the 3D loop outperform the 2D one when its height exceeds a certain threshold, but it can also address the challenge of efficiently radiating between conducting sheets, a situation typically encountered in vertically stacked systems.

2.4 GPS Antenna

The findings of Sec. 2.2 and 2.3 are used to design 3D loops for two practical systems. The first one, presented in this section, is a cm-scale GPS receiver [12]. Its size is limited to $10 \times 10 \times 6$ mm^3, including the antenna. It is more than four times smaller than the one presented in [10, 11] in terms of volume. Earlier GPS loggers [61] and commercially available ones [62] are significantly larger: $40 \times 68 \times 18$ mm^3 and $72 \times 45 \times 20$ mm^3, respectively.

The antenna design, having a ka value of 0.241, is shown in Fig. 2.4 with its dimensions

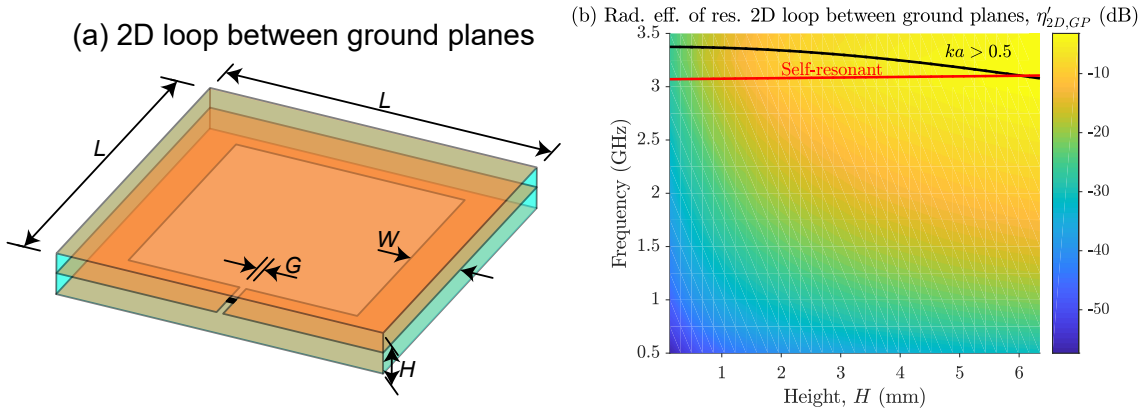

Figure 2.3: (a) 2D loop between two conducting sheets (ground planes), and (b) its radiation efficiency when resonant. The black curve corresponds to the electrically small limit: $ka < 0.5$. The red curve corresponds to the height-frequency limit above which this loop is self-resonant.

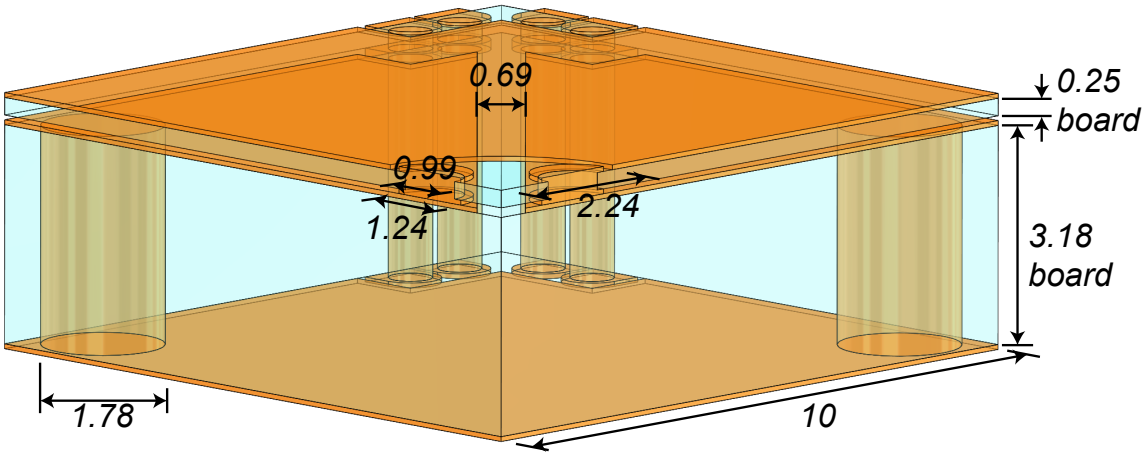

Figure 2.4: The proposed 3D loop GPS antenna with its dimensions in mm. It consists of two boards (0.25 and 3.18 mm thick), made of Rogers RT/duroid® 5880. The two 0.99 mm vias in the front are connected to the differential feed of the AFE. The top and bottom metal layers of the 3.18 mm thick board and the 1.78 mm vias form the radiating loop.

in mm. It exhibits mirror symmetry across the middle. It consists of two PCBs, one with a thickness of 0.25 mm and the other with a thickness of 3.18 mm. Both boards are made using Rogers RT/duroid® 5880 substrates.

The top layer of the 0.25 mm thick board contains a metallic cladding from which a region with radius 2.24 mm centered at the front corner is removed. The two sides of this board are connected through two metallic castellated (half) vias (0.99 mm via diameter, 1.24 mm pad diameter). The bottom layer of this board does not contain any additional metal, other than that needed for the via pads.

The top layer of the 3.18 mm thick board contains a metallic cladding from which a diagonal strip that is 0.69 mm wide is removed. The two sides of this board are connected through two metallic vias (1.78 mm via diameter), placed 0.1 mm away from the board edge. The bottom layer of this board is a solid metal layer.

A set of four vias can be seen in the back that go through both boards and provide connectivity between components that may be placed on top and bottom of the antenna. They do not affect its RF performance. The antenna is linearly polarized, has a ka value of 0.176, and exhibits the well-known radiation pattern of a magnetic dipole.

The two boards are electrically connected by soldering the castellated vias of the thin board to the top layer of the thick board. These vias act as the feed, and are connected to the differential output of the Analog Front-end (AFE). Fig. 2.5 shows the current on the GPS antenna when it is excited differentially. The current flows down the left 0.99 mm via, to the left of the antenna, then down the left 1.78 mm via. It crosses the bottom metal plane to the right side of the antenna, and goes up the 1.78 mm via. It then travels towards the right 0.99 mm via and reaches the other terminal of the feed.

From Fig. 2.2(d), the efficiency of a 3D loop occupying the same volume is -4.57 dB. The efficiency of the antenna presented in Fig. 2.4 is -5.11 dB according to simulation. A small trade off in terms of efficiency is made in order to make the design symmetric across a plane (to accommodate for a differential feed) and to shield the diagonal gap from any boards placed on top of the antenna (which will introduce parasitic capacitance).

Fig. 2.6(a) and (b) present the top and bottom views of the fabricated antenna prototype, respectively. The radiation efficiency of the fabricated anntenna was measured using the modified Wheeler cap method [63] when its terminals were connected to a semi-rigid coaxial cable with a bazooka balun. The measured radiation efficiency is -4.8 dB, which is slightly higher than what was expected from simulation. The discrepancy is attributed to the connector used (open ended coaxial cable with a bazooka balun), which will also radiate a small amount of the input power.

The input impedance of the GPS antenna is shown in Fig. 2.7. The blue solid lines

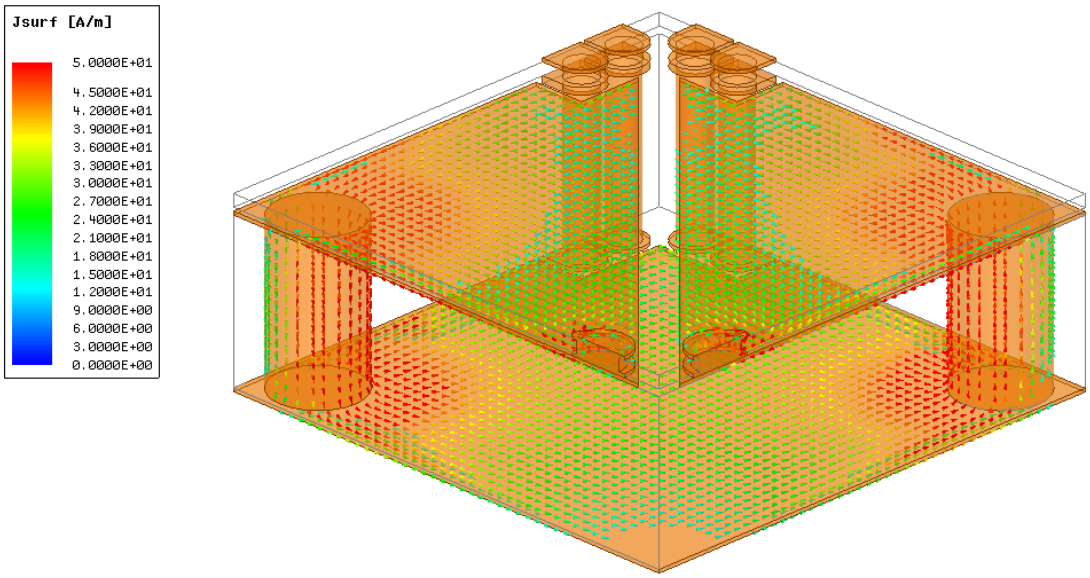

Figure 2.5: The current that flows through the GPS antenna when excited differentially. The current flows down the left 0.99 mm via, to the left of the antenna, then down the left 1.78 mm via. From there, it crosses the bottom metal plane to the right side of the antenna, and goes up the 1.78 mm via. It then travels towards the right 0.99 mm via and reaches the other terminal of the feed. The top metal layer of the 0.25 mm thick board is not depicted.

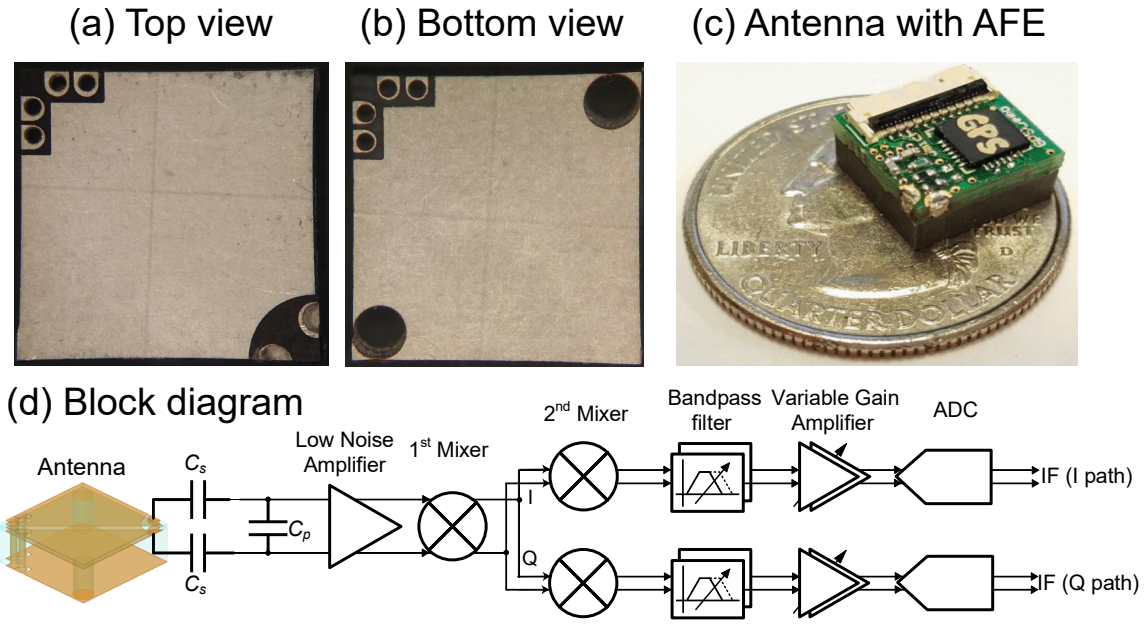

Figure 2.6: (a) Top, and (b) bottom view of the fabricated GPS antenna. (c) The GPS antenna with the PCB containing the AFE, on a US quarter. (d) Block diagram of the antenna, matching capacitors and the AFE.

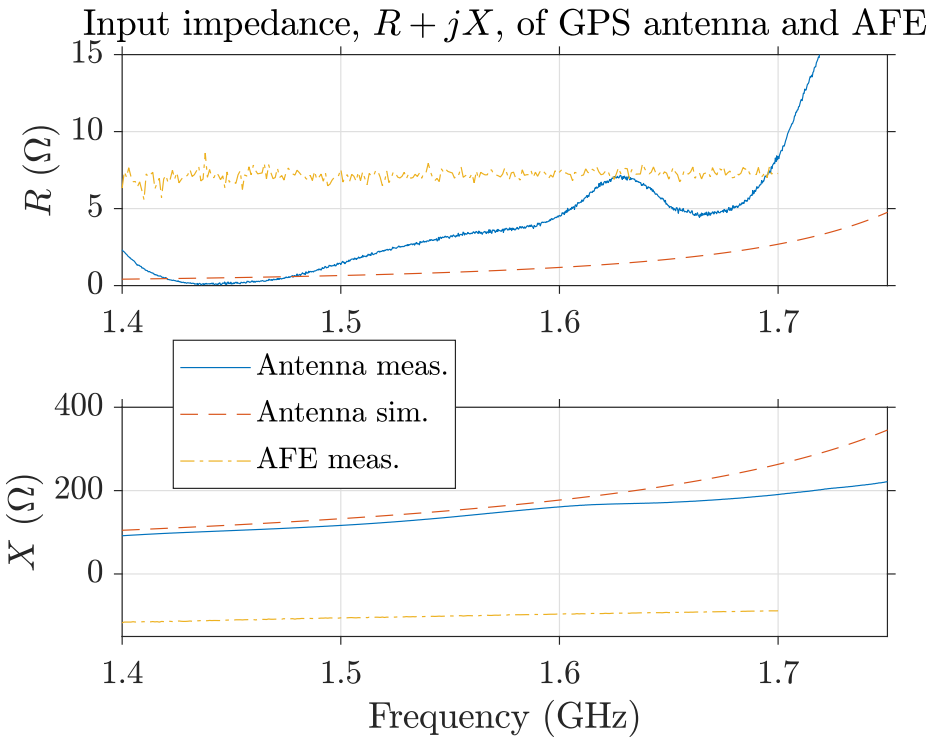

Figure 2.7: The input impedance of the GPS antenna and the AFE. The antenna is inductive and can be conjugately matched to the AFE using only lumped capacitors.

correspond to the measured resistance and reactance of the GPS antenna, while the red dashed lines correspond to simulation values. The impedance of the AFE (the design of which was presented in [12]) is shown using the yellow dot-dashed lines. Using the selected measurement setup, it was difficult to accurately measure low resistance values of the antenna.

Fig. 2.6(c) shows the antenna when it is connected to the PCB containing the AFE. A US quarter is also shown for comparison. The block diagram of the system is shown in Fig. 2.6(d). It includes the antenna, three matching capacitors, a low noise amplifier (LNA), an active Gilbert cell double balanced mixer for down-conversion to 200.7 MHz, two I/Q passive mixers for down-conversion to 4.3 MHz, two intermediate frequency (IF) bandpass filters, a variable gain amplifier (VGA), and two 2 bit analog-to-digital converters (ADC) with 10.74 MHz sampling rate.

Instead of matching both the antenna and the AFE to $50\,\Omega$, the antenna is conjugately matched to the AFE using capacitors. Two lumped capacitors are placed in series with the antenna, each with capacitance $C_s = 2.6$ pF. A lumped capacitor with capacitance $C_p = 0.4$ pF is then placed in parallel. The losses in these matching components lower the antenna's radiation efficiency to -5.25 dB. The system also contains a low-noise amplifier

(LNA), three mixers, two bandpass filters, two variable-gain amplifiers (VGA), and two analog-to-digital converters (ADC).

2.5 Medium Range Radio Antenna

In this section, the antenna for a second communication system is presented. The specifications set by the funding agency required that this system should be able operate across 20 m in an indoor environment, including a layer of wall. Eventually, a mesh of such systems would be deployed in an indoor environment to monitor a quantity such as temperature, pressure, humidity, etc.

The primary goal is to achieve such operation using a mm-scale device with volume $3.41 \times 3.62 \times 3.8$ mm^3, which includes the antenna, batteries, photovoltaic (PV) cell, and integrated circuits. Since this system has limited range, the name MRR is chosen for it. Aspects of this system, namely the modulation scheme and the implementation of the circuits, have been presented in [7] and [8], respectively. The antenna for this system will be shown to be a multi-turn 3D loop.

2.5.1 Carrier Frequency Selection

As opposed to GPS, where the carrier frequency is set, the frequency of operation of a communication system can be chosen to optimize a system's performance. Three ISM frequency bands serve as candidates for the MRR system: 915 MHz, 2.4 GHz, and 5.8 GHz. The path loss between the transmitting and receiving antennas as a function of frequency, f, is calculated in dB:

$$PL(f) = -20\log_{10}\left(\frac{\lambda}{4\pi}\right) + N\log\left(d\right) - \eta_R(f) - D_R + WL(f), \tag{2.20}$$

where:

- λ is the wavelength in meters,
- N is the loss coefficient,
- d is the distance in meters,
- η_R is the radiation efficiency of the receiving antenna in dB,
- D_R is the directivity of the receiving antenna in dB, and
- WL is the loss introduced by one layer of wall in dB.

Table 2.1: Radiation efficiency and directivity of receiving 3D loop antenna

	915 MHz	2.4 GHz	5.8 GHz
η_R (dB)	-30.73	-16.86	-4.18
D_R (dB)	2.19	2.06	1.86

The loss coefficient, N, is assumed to be 30 to model any additional losses that are specific to an indoor environment such as shadowing or multipath [64, 7]. The distance is set to $d = 20$ m to comply with the specifications of the problem. The receiving antenna will be assumed to be a resonant 3D loop (Fig. 2.2(b) with $L = 3.5$ mm, $H = 1.58$ mm, $D = 0.4$ mm, $G = 0.2$ mm). The radiation efficiency, η_R, and directivity, D_R, values for this antenna at the three possible frequencies (obtained through simulation in ANSYS Electronics Desktop) are summarized in Tab. 2.1. The angular or polarization dependence is not taken into account in this treatise.

The loss from a layer of wall depends on the wall material [65, 66, 67]. Using the results in Fig. 6 of [66], the following linear models for the loss resulting from a 12 in. wall (expressed in dB) are extracted (f in GHz):

$$\begin{aligned} \text{Adobe brick: } WL(f) &= 4.48f - 0.57, \\ \text{Cinderblock brick: } WL(f) &= 5f + 5, \\ \text{Reinforced concrete: } WL(f) &= 10.65f - 1.95, \\ 0.5 \text{ GHz} \leq f &\leq 6 \text{ GHz}. \end{aligned} \tag{2.21}$$

Fig. 2.8 shows the path loss for the line-of-sight (LOS) case, as well as for the three wall materials, as a function of frequency. When operating within LOS, selecting a higher carrier frequency ensures a smaller overall path loss. The increased radiation efficiency of the antenna at higher frequencies compensates for the increased free space path loss. On the other hand, when communicating through a wall, lower frequencies result in a lower overall path loss. In those cases, the increased loss introduced by the wall at higher frequencies prevails over the increased radiation efficiency. As a result, the 915 MHz ISM band is chosen for the MRR.

2.5.2 Antenna Design and System Integration

The antenna for the MRR is presented in Fig. 2.9. Similar to the GPS antenna (Fig. 2.4), it consists of two boards made using RT/duroid® 5880 material. The thicker board measures

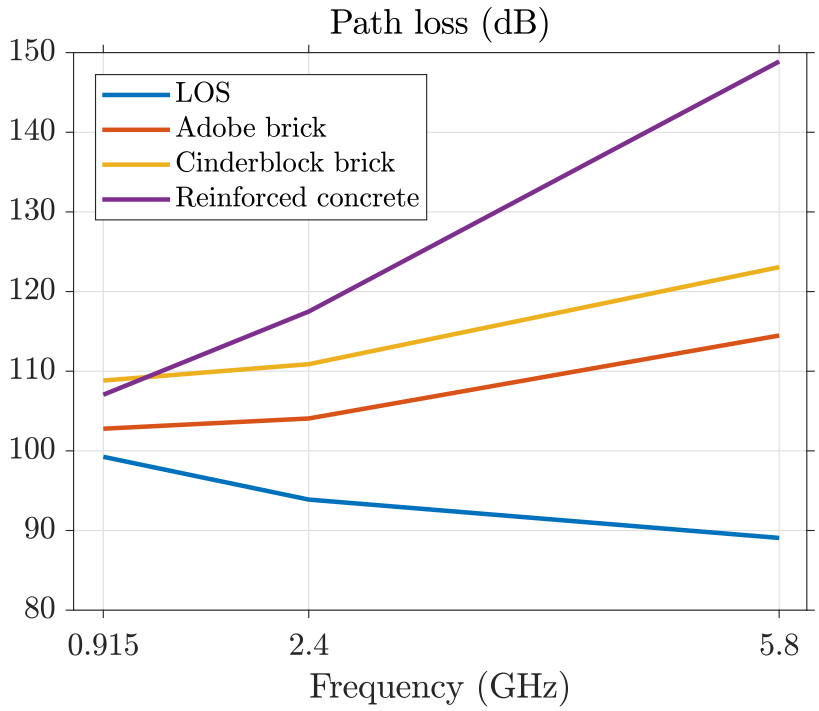

Figure 2.8: The path loss (in dB) at 20 m, in an indoor environment, using a 3.5x3.5x1.58 mm^3 3D loop antenna in LOS and non-LOS (12 in. walls of different materials) scenarios.

$3.62 \times 3.41 \times 1.58$ mm^3, while the thiner one measures $3.31 \times 3.41 \times 0.38$ mm^3. The antenna is extremely small, exhibiting a ka value of only 0.051. Its radiation efficiency, obtained through simulation, is -26.86 dB before matching.

The two boards are connected through the castellated vias of diameter 0.32 mm (pad diameter of 0.52 mm) that serve as the feed for the RF signal. The two boards also have a set of five full vias (with 0.25 mm diameter and 0.46 mm pad diameter), which provide connectivity between PCBs placed on the top and bottom of the antenna. Such PCBs contain the rest of the components in the system: integrated circuits, batteries, and a PV cell.

The 1.58 mm thick board forms a 4-turn loop that is responsible for radiation. The higher number of turns leads to a higher inductance, meaning that a smaller capacitance is needed to achieve resonance. Given the finite tunability of (absolute) capacitance that can be achieved on chip, this increases the range over which the resonant frequency can be tuned. The 0.38 mm thick board connects the integrated circuits to the terminals of this loop.

Photos of the fabricated antenna are shown in Fig. 2.10(a-b). The system, including the antenna, integrated circuits (chips), batteries, and PV cell, is shown in Fig. 2.10(c-d). The details of this system, as well as the experimental results obtained from it, were presented

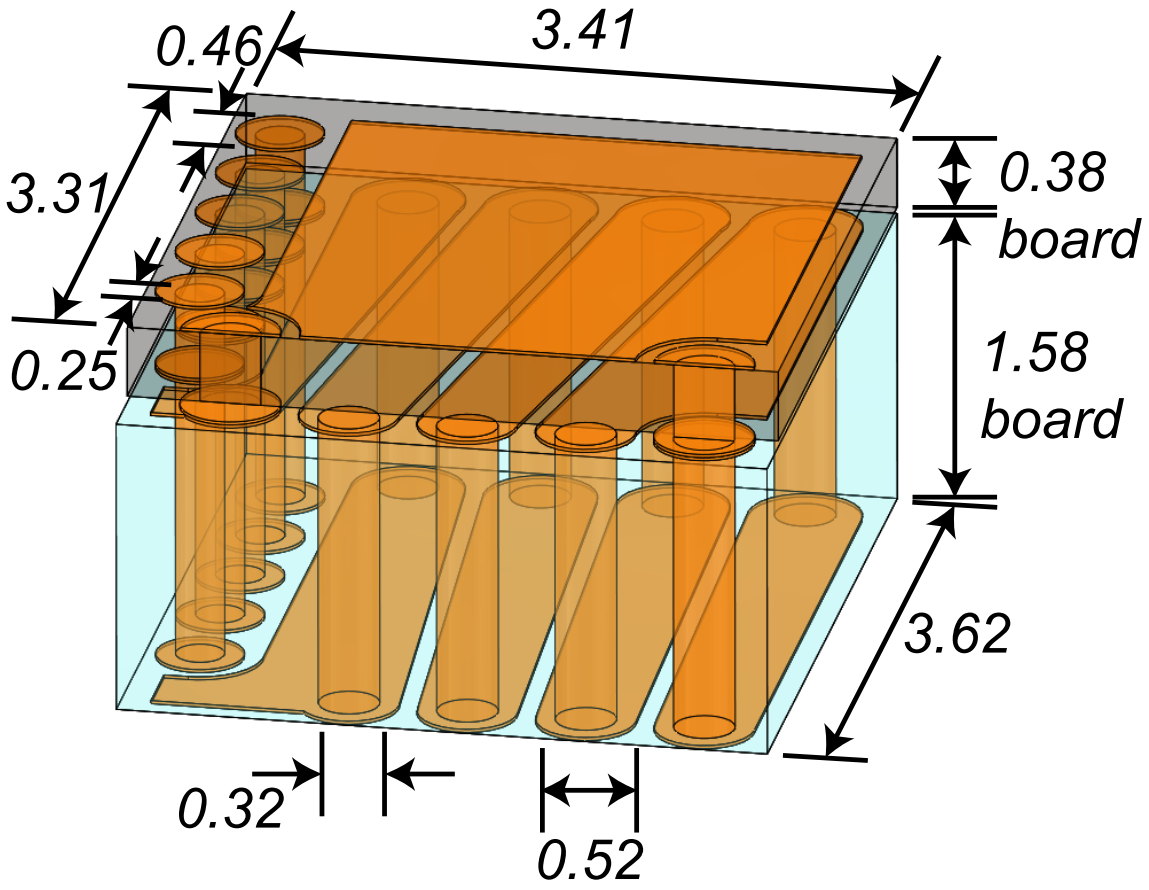

Figure 2.9: A 3D loop antenna for the MRR system. Dimensions are given in mm. It consists of two boards (0.25 and 1.58 mm thick), made using Rogers RT/duroid® 5880. The two short vias in the front are connected to the PCB containing the circuits.

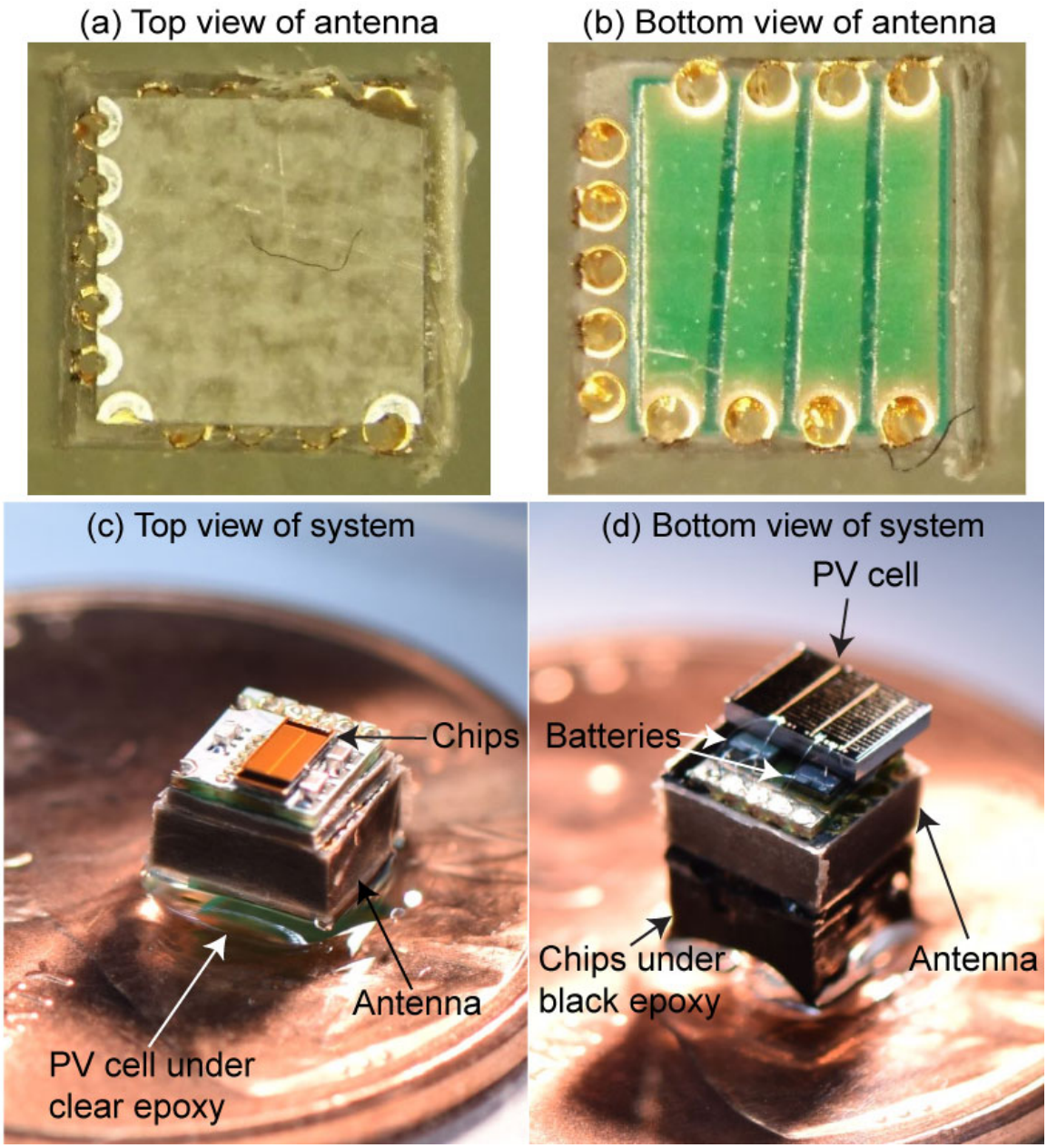

Figure 2.10: (a) Top, and (b) bottom view of the fabricated MRR antenna. (c) Top, and (d) bottom view of the MRR system, including the antenna, integrated circuits (chips), batteries and the PV cell.

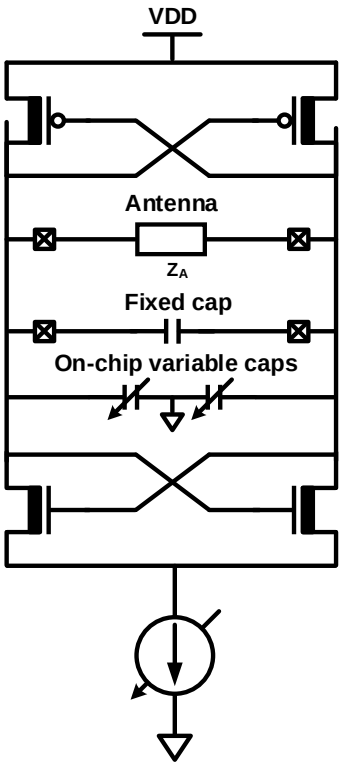

Figure 2.11: The schematic of the tranceiver's circuit, used in the MRR system.

in [8]. An audio sensor node using the proposed antenna has also been developed [9].

The transceiver circuit, shown in Fig. 2.11, is co-designed with the 3D loop antenna to ensure an overall efficient operation [8]. In transmit (TX) mode, instead of using a traditional power amplifier and phase-locked loop, a cross-coupled driver delivers power directly to the antenna. The antenna forms the inductor in the tank circuit of the oscillator. A combination of fixed and variable capacitors is utilized to ensure that the antenna resonates at 915 MHz. By modulating the tail current of the cross-coupled transistors (turning it on or off), the RF carrier and on-off keying signal are simultaneously generated [68]. The low losses in the antenna (compared to a commercially available surface-mount inductor) lower the power consumption of the oscillator, making it energy-efficient.

In receive (RX) mode, the TX transistors are reused together with the low-loss 3D loop antenna to obtain a passive voltage gain (Q times boosting) and filtering [69], thereby replacing a power-hungry low-noise amplifier and bulky off-chip filters. The antenna forms the inductor in the LC resonant network resulting in a high-swing voltage signal at the terminals of this LC network [70]. Due to the mechanism of voltage amplification (resonance), the architecture of the system differs from the conventional super-regenerative

receiver [68].

Due to the extremely small size of the antenna, it is impractical to measure its input impedance by connecting it to a semi-rigid coaxial cable and a bazooka balun, as was done for the GPS antenna. Instead, a simple FR4 PCB was designed to connect the antenna terminals to the VNA using a U.Fl connector and U.Fl to SMA coaxial cable. The schematic of this simple PCB, shown in Fig. 2.12(a), contains:

- two lumped components in series, denoted by Z_s,
- a lumped component in parallel, denoted by Z_p, and
- the antenna, denoted by Z_A.

In the first configuration examined, the series component, Z_s, was a short, while the parallel component, Z_p, was an open. This can be verified in Fig. 2.12(b), where solder bridges are used in place of the series component, and the parallel component is absent. This configuration allows the measurement of the antenna impedance as seen by the circuit. The simulated and measured values of resistance and reactance are presented in Fig. 2.12(c). The experimental results show reasonable agreement with those from simulation.

In the second configuration, the antenna is matched to $50\,\Omega$ using lumped capacitors to show how it can be used in conventional $50\,\Omega$ systems. Specifically, the series components were chosen to be 0.3 pF capacitors, while the parallel component was 0.8 pF. A photo of the PCB with these components is shown in Fig. 2.12(d). The values of the components were chosen such that a match is achieved at 913 MHz according to simulation. The simulated and measured input reflection coefficient, S_{11}, is shown in Fig. 2.12(e). The minimum value of measured S_{11} is observed at 942.5 MHz, 3.23% higher than simulation. This deviation is expected given that the reactance of the fabricated antenna prototype was measured to be slightly different from the simulated valued (Fig. 2.12(c)) as a result of the antenna fabrication tolerances.

The simulated radiation efficiency of the antenna in the second configuration is -28.66 dB at 913 MHz. Using the modified Wheeler cap method [63], the measured radiation efficiency of the antenna in the second configuration is -28.84 dB at 942.5 MHz.

2.5.3 Radiation Pattern

The radiation patterns of the MRR antenna are investigated using the second configuration, which is the only one that is matched to $50\,\Omega$. The placement of the antenna together with the coordinate system is shown in Fig. 2.13.

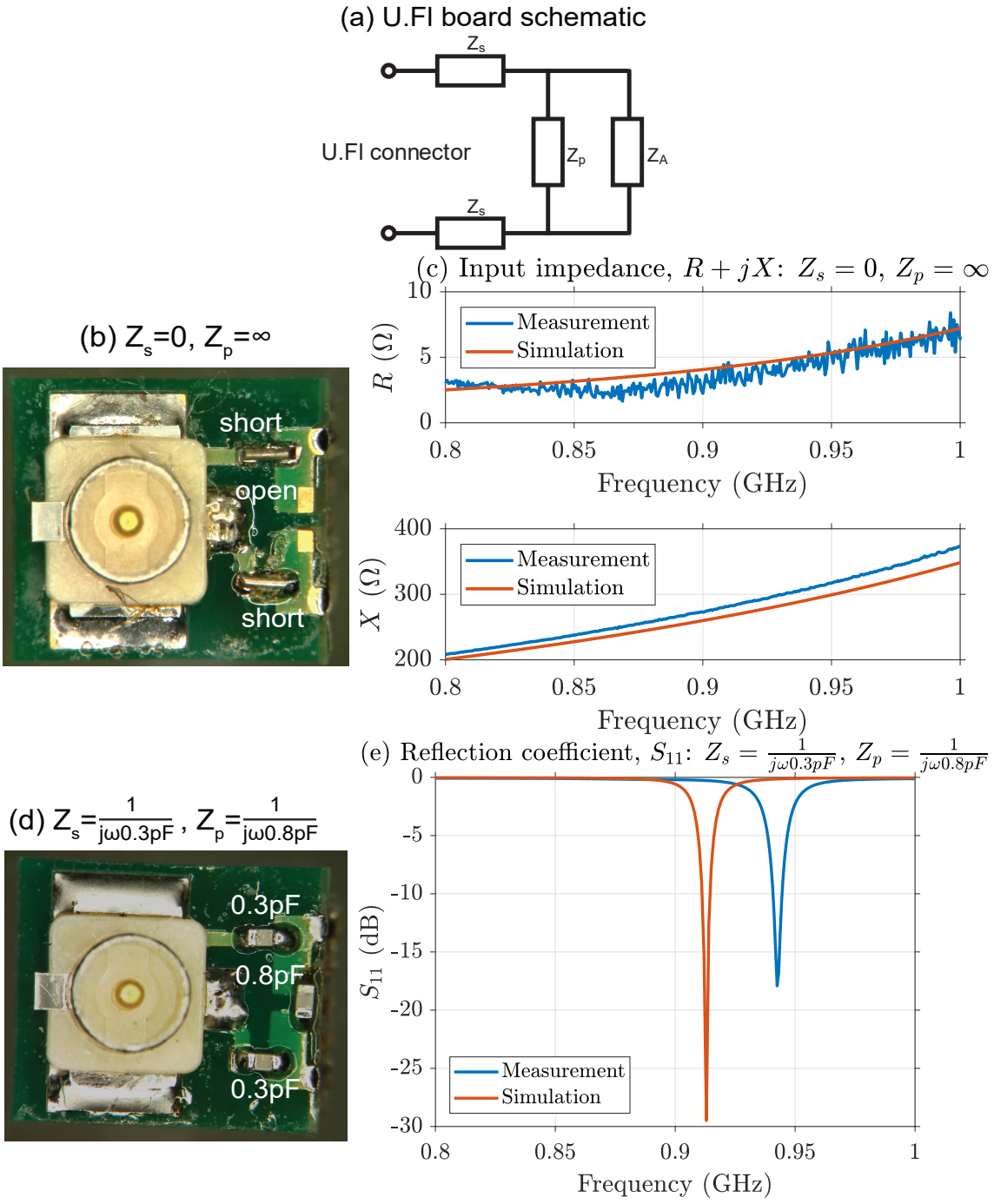

Figure 2.12: (a) The schematic of the PCB that is used to measure the input impedance of the antenna for the MRR system. (b) Photo of the PCB in the first configuration: $Z_s = 0$, and $Z_p = \infty$. (c) Input impedance measured using the first configuration. (d) Photo of the PCB in the second configuration: $Z_s = \frac{1}{j\omega 0.3pF}$, and $Z_p = \frac{1}{j\omega 0.8pF}$. (e) Input reflection coefficient measured using the second configuration.

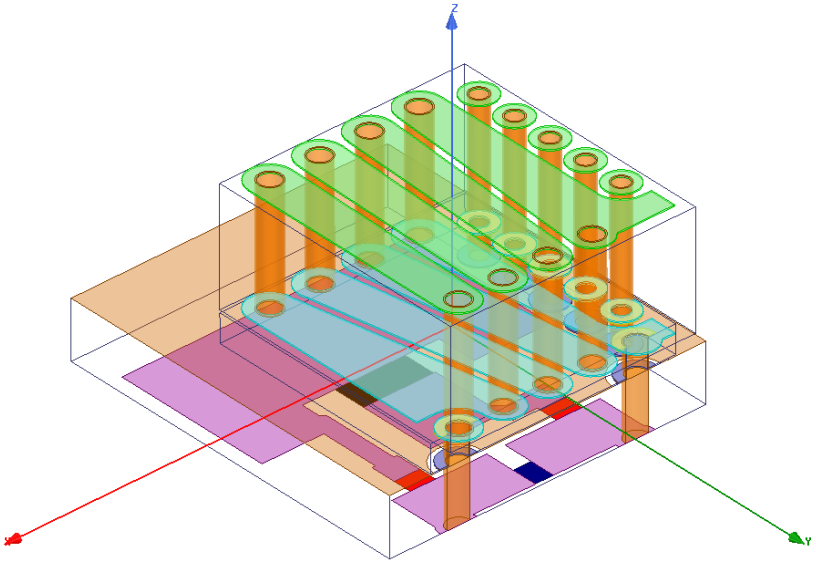

Figure 2.13: The MRR antenna in the second configuration with its coordinate system for radiation pattern simulations and measurements.

Fig. 2.14 presents the radiation pattern of the antenna along the xy-plane as a function of ϕ. The antenna constitutes a magnetic dipole along the $\widehat{x}$-axis. As a result, a donut shaped radiation pattern is expected on this plane. The blue line corresponds to the $\widehat{\theta}$-polarized field from simulation, while the red line corresponds to the $\widehat{\phi}$-polarized field. The presence of the additional PCB containing the U.Fl connector and matching components causes the peak to shift away from $\phi = 90°$. The measured radiation patterns are shown in yellow and purple dots.

Fig. 2.15 presents the radiation pattern of the antenna along the yz-plane as a function of θ. A uniform radiation pattern is expected on this plane. Again, the blue line corresponds to the $\widehat{\theta}$-polarized field from simulation, while the red line corresponds to the $\widehat{\phi}$-polarized field. The measured radiation patterns are shown in yellow and purple dots.

2.6 Chapter Summary

Using well-known equivalent circuits for electric and magnetic dipole antennas that are electrically small, it was shown that magnetic dipoles exhibit higher radiation efficiency when losses associated with matching components are taken into account. The design concept of 3D loops was introduced, which exhibit higher radiation efficiency than 2D (planar) loops when their height exceeds a certain threshold and are easier to integrate in volume-constrained, vertically stacked systems that may include PCBs with ground planes.

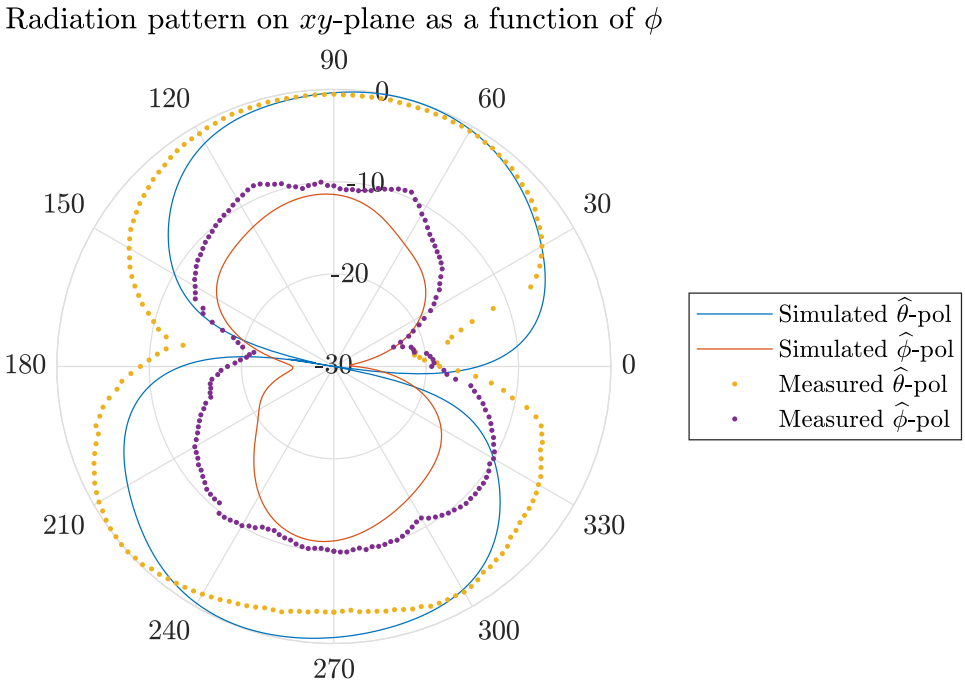

Figure 2.14: The radiation pattern of the MRR antenna in the second configuration on the xy-plane (see Fig. 2.13 for antenna placement).

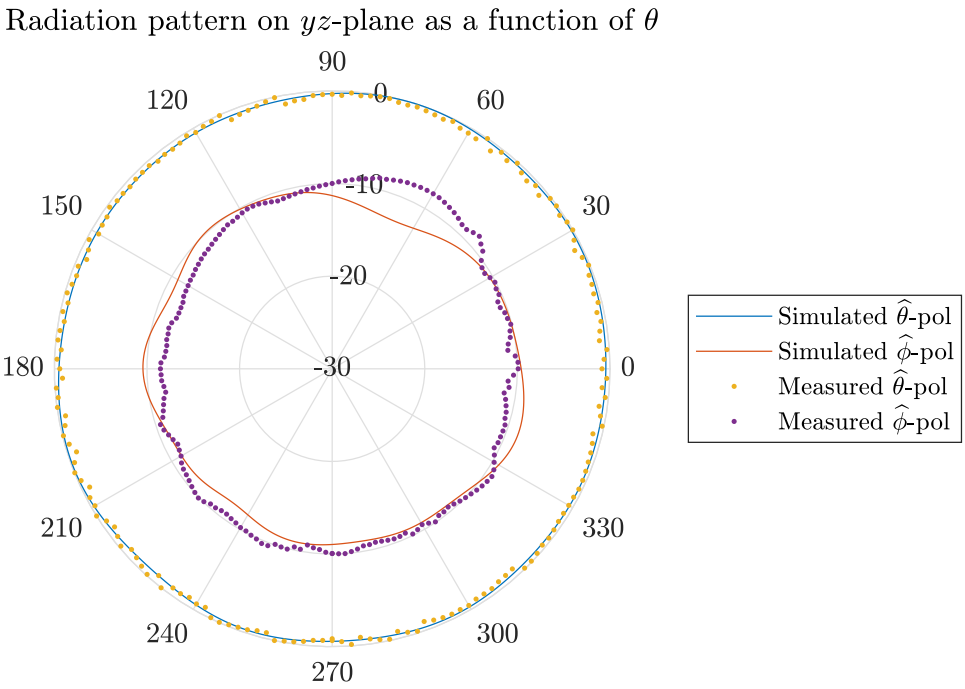

Figure 2.15: The radiation pattern of the MRR antenna in the second configuration on the yz-plane (see Fig. 2.13 for antenna placement).

Two examples were presented where 3D loops were used in practical, extremely compact communication systems. The first example was a single-turn 3D loop antenna for a $10 \times 10 \times 6$ mm^3 GPS receiver. The antenna with $ka = 0.176$ was conjugately matched to the input of the analog frontend using lumped capacitors. The second example was a multi-turn 3D loop antenna ($ka = 0.051$) for a $3.41 \times 3.62 \times 3.8$ mm^3 transceiver operating at 915 MHz. The frequency of operation was chosen to ensure the smallest path loss for a signal propagating 20 m in an indoor environment through a wall. The antenna was tightly integrated with the circuits of the transceiver to ensure an acceptable overall performance.

The ESAs presented here, combined with ultra-low power transceiver circuits, pave the way for IoT devices that provide ubiquitous and seamless connectivity in extremely compact form factors and in complex propagation environments.

CHAPTER 3

Nondiffracting Waves: Refractive Optics Bessel Beam Radiator

In the previous chapter, we investigated electrically small antennas operating in a constrained reactive near field environment. Multiple components were placed in close proximity to the antennas, requiring a design that is able to radiate as part of a compact, vertically stacked system.

In this chapter as well as the following one, we shift our attention from the reactive near field to the radiative near field. Specifically, we study nondiffracting waves and pulses, which can only exist in the radiative near field (Fresnel zone). Two radiators are introduced, which manipulate the fields created by monopoles and convert them into localized waves and pulses.

3.1 Chapter Introduction and Outline

Since the seminal work of Brittingham [14], numerous advancements have been made in the area of localized waves [13]. Such waves resist diffraction and, as a result, maintain their field profile as they propagate. Brittingham introduced focus wave modes as packet-like solutions to Maxwell's equations that remain focused as they propagate. Ziolkowski addressed the issue of infinite energy possessed by these solutions by superimposing them to construct electromagnetic directed-energy pulse trains of finite energy [15].

In his work on electromagnetic missiles, Wu manipulated the rise time of a radiating aperture to generate fields that decay slower than $1/r$ [16]. He did so by effectively extending the radiative near field (where such phenomena can occur) to larger distances. Electromagnetic bullets, introduced by Moses and Prosser, are solutions to the wave equation that are confined to a cone [17]. These energy packets have the classical $1/r$ field decay, but remain localized along a ray path.

Durnin revolutionized the field of localized waves by introducing Bessel beams, which are superluminal, monochromatic solutions to the wave equation that do not diffract [18]. Although ideal Bessel beams cannot be generated, since they require infinite energy, their truncated counterparts are realizable and resist diffraction over a specified distance called the nondiffracting range. In Appendix A, truncated Bessel beams are compared to conventional Gaussian beams to demonstrate the practical significance of this nondiffracting property. A Bessel beam propagating along an axis results from the interference of all the plane waves that form a specific angle, called the cone angle, with the axis. This angle determines the phase and group velocity of the wave, and, together with the size of the aperture, determine the nondiffracting range.

The electric and magnetic fields of a Transverse Magnetic (TM), radially polarized Bessel beam in cylindrical coordinates are [20]:

$$\begin{aligned} E_\rho = j\frac{k_z}{k_\rho}J_1(k_\rho\rho)e^{-jk_z z}, E_\phi = 0, E_z = J_0(k_\rho\rho)e^{-jk_z z}, \\ H_\rho = 0, H_\phi = j\frac{k_0}{\eta_0 k_\rho}J_1(k_\rho\rho)e^{-jk_z z}, H_z = 0. \end{aligned} \tag{3.1}$$

For a TE, azimuthally polarized Bessel beam

$$\begin{aligned} E_\rho = 0, E_\phi = -j\frac{k_0}{k_\rho}J_1(k_\rho\rho)e^{-jk_z z}, E_z = 0, \\ H_\rho = j\frac{k_z}{\eta_0 k_\rho}J_1(k_\rho\rho)e^{-jk_z z}, H_\phi = 0, H_z = \frac{1}{\eta_0}J_0(k_\rho\rho)e^{-jk_z z}. \end{aligned} \tag{3.2}$$

Since their discovery, Bessel beams have been used in many practical applications. Originally, researchers envisioned using them for medical ultrasonic imaging, tissue characterization and nondestructive evaluation of materials [28]. More recent applications include optical conveyors [29], electron microscopy [30], microfabrication of dielectrics [31], exerting forces on biological cells [32], and optical communications [33].

Bessel beams can be generated through a range of techniques. At microwave frequencies, axicons [19], leaky wave antennas [20, 21], cascaded metasurfaces [22], and GRIN lenses [23] have been used, among other techniques. At optical frequencies, researchers have employed axicons [24], plasmonic metasurfaces [25], localized modes [26], and holography [27].

A superposition of Bessel beams with a common cone angle over a range of frequencies yields localized pulses known as X waves, first introduced by Lu and Greenleaf [38]. All frequency components of an X wave travel at the same velocity. As a result, these pulses

resist both diffraction (spatial spreading) and dispersion (temporal spreading), and remain confined as they propagate.

Although multiple techniques/structures have been suggested for the generation of Bessel beams, little progress has been made on the generation of X waves outside of optical frequencies [71, 72]. At microwave frequencies, a radial line slot antenna was proposed in [73], whose bandwidth is limited by the frequency dispersion of the radial waveguide. In general, the minimum cone angle that can be achieved with leaky wave structures is also limited by their high attenuation rate for radiation near broadside. A microwave system using a circular slit and a parabolic mirror was used in [74] to verify the superluminal behavior of X waves. The mirror acts as a lens, applying a Fourier transform to the field of the slit, resulting in the generation of a Bessel beam profile.

In order to generate X waves at microwave frequencies, a device must exhibit a large bandwidth and minimal dispersion within that bandwidth. Designing a directly fed radiator would be advantageous since it would occupy less space than an illuminated transmissive or reflective device. Finally, the device should operate efficiently.

Ultrawideband systems such as those used in radars, medical imaging, or digital communications, employ broadband antennas designed to operate in the far field [75]. In general, the radiating elements of these systems have low directivity. On the contrary, antennas operating in the radiative near field (Fresnel zone) have been developed for narrowband applications, e.g. radiometry [76], RFID [77] and focusing systems [78]. Here, a radiator with 50% fractional bandwidth is developed to generate spatially confined fields in the Fresnel zone. Unlike the earlier works [72, 71, 74], the radiated beam exhibits a well-defined TM polarization and the modal purity of a single dominant Bessel beam mode, as described in (3.1). When fed with a broadband pulse, the radiator emits nondispersive, nondiffracting X waves.

To the best of the authors' knowledge, this is the first device capable of generating X waves where the fields have been experimentally measured. The generated X waves exhibit polarization purity: a well-defined $\mathrm{TM_z}$ polarization. The radiator exhibits 2° of cone angle dispersion over a 50% fractional bandwidth. The radiator presented in [79] exhibits 24° of cone angle dispersion over a 21% fractional bandwidth.

This chapter is organized as follows. The design of the radiator is outlined in Sec. 3.2. The device's ability to generate Bessel beams over a broad bandwidth is presented in Sec. 3.3. Simulation as well as experimental results are given. In Sec. 3.4, the device's ability to generate X waves is shown, using both frequency and time domain experimental results. Finally, Sec. 3.5, summarizes the findings.

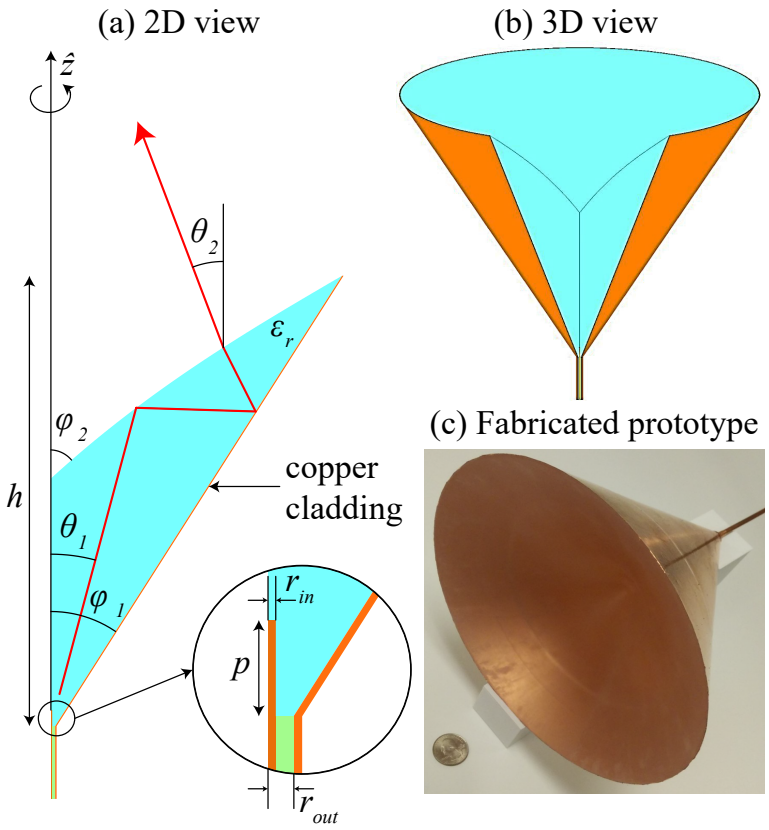

Figure 3.1: (a) Cross-sectional view of the Bessel beam radiator with ray tracing diagram, (b) 3D view of device, and (c) picture of the fabricated prototype. A U.S. quarter is also shown for comparison.

3.2 Design of Bessel Beam Radiator

The design of the proposed Bessel beam radiator is depicted in Fig. 3.1(a). The radiator generates TM-polarized φ-invariant Bessel beams. As a result, its design is rotationally symmetric about the z-axis. The device is fed by a coaxial cable with inner and outer radii equal to r_{in} and r_{out}, respectively, as shown in the inset of Fig. 3.1(a). The green region corresponds to the insulator within the coaxial cable. The inner conductor of the coaxial cable is extended by a length p to form an electrically small monopole. The outer conductor of the coaxial cable is flared outwards, forming an angle φ_1 with respect to the z-axis. The blue region, into which the monopole radiates, is filled with a material of dielectric constant ε_r. At every point along the curved air-dielectric interface, the tangent line forms an angle φ_2 with respect to the z-axis. The height of the device is h. A cutaway three-dimensional view of the design is shown in Fig. 3.1(b). An earlier version of this device having a straight interface was presented in [34]. The radiator presented here exhibits higher spectral purity in the spatial domain.

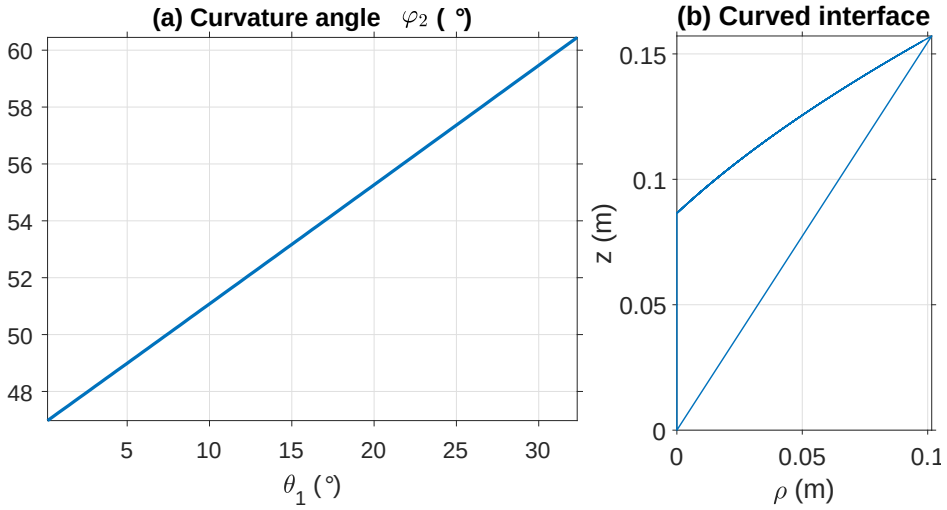

Figure 3.2: (a) Curvature angle φ_2 as a function of ray angle θ_1 that maintains a constant cone angle $\theta_2 = 20°$, and (b) the curved interface resulting from the changing φ_2 angle.

Consider a ray emanated by the radiating monopole at an angle θ_1 with respect to the z-axis (shown in red in Fig. 3.1(a)). The ray is totally internally reflected at the air-dielectric interface by appropriately selecting the dielectric constant ε_r. It is then directed toward the copper cladding of the device and reflected back toward the interface. When it reaches the interface for a second time, the ray forms a much smaller angle with the air-dielectric interface, and exits at an angle θ_2 with respect to the z-axis. Assuming that a unique curvature angle φ_2 corresponds to each ray angle θ_1 (an assumption that can be shown to hold when the range of φ_2 is small), the cone angle, θ_2, can be written as:

$$\theta_2(\theta_1) = 90° - \varphi_2(\theta_1) - \sin^{-1}\left(\sqrt{\varepsilon_r}\cos(3\varphi_2(\theta_1) - 2\varphi_1 - \theta_1)\right). \tag{3.3}$$

The dielectric constant of the material is chosen to be $\varepsilon_r = 2.53$, which corresponds to Rexolite®: a low-loss polymer (tan$\delta = 0.00066$ at 10 GHz). The cone half-angle is set to $\varphi_1 = 32.5°$ for impedance matching purposes. Eq. (3.3) is then numerically solved for ray angles ranging from $\theta_1 = 0°$ to $\theta_1 = \varphi_1 = 32.5°$ to find the curved interface that yields a constant cone angle of $\theta_2 = 20°$. Using this approach, the curvature angle φ_2 was found to change linearly with ray angle θ_1, as shown in Fig. 3.2(a). Using this curvature angle, the shape of the interface was calculated, and is presented in Fig. 3.2(b).

The resulting near field radiator is shown in Fig. 3.1(a). The device is fed with an RG402 coaxial cable ($r_{in} = 0.455$ mm, $r_{out} = 1.485$ mm), the center conductor of which has been extended by $p = 5.6$ mm, as shown in the inset of Fig. 3.1(a). The height of the

overall structure is $h = 157.15$ mm.

The dielectric structure was fabricated using standard CNC machining (milling/lathing). The outer cladding was realized by applying a copper foil (3M$^{\text{TM}}$ 1126) to the dielectric structure and electrically connecting it to the outer conductor of the coaxial cable. A picture of the fabricated device is shown in Fig. 3.1(c).

3.3 Bessel Beam Generation

The ability of the device presented in the previous section to generate TM Bessel beams is demonstrated next. The radiated electric field has both longitudinal (z directed) and radial (ρ directed) components, as outlined in (3.1).

The longitudinal electric field of a nonapodized TM Bessel beam is a zeroth-order (φ-invariant) Bessel distribution

$$E_z(\rho, z) = J_0(k_0 \sin\theta_2 \rho) e^{j(\omega t - k_0 \cos\theta_2 z)}, \tag{3.4}$$

where k_0 is the free space wavenumber and θ_2 is the cone angle. A dependence of θ_2 on frequency results in beam dispersion. The geometrical optics design of the curved air-dielectric interface helps minimize dispersion (approximately 2° between 19 and 29 GHz), a phenomenon that results in degraded X waves [73].

In Fig. 3.3, the magnitude of the fields generated by the radiator are presented at four frequencies: 19, 22, 25 and 29 GHz. Each row corresponds to one of these frequencies in increasing order from top to bottm. The simulated field components shown are the radial electric field (E_ρ) in the first column, and the longitudinal electric field (E_z) in the second column. COMSOL Multiphysics®, a commercial finite element solver, was used to simulate the axially symmetric device. The measured E_z is plotted in the third column. The fields were measured using a coaxially fed electric monopole acting as a probe, attached to a three-dimensional translation unit and a vector network analyzer (see Fig. 3.4). The simulated azimuthal magnetic field (H_ϕ) is plotted in the fourth column.

The radial electric field exhibits the same spatial distribution as the azimuthal magnetic field having a null along the z-axis, as shown in (3.1) and expected from theory [20]. E_z possesses an apodized version of the profile given by (3.4), within the nondiffracting range of the device. The dielectric region preserves the polarization of the wave emitted by the coaxial cable. That is, the radial electric field in the coaxial cable excites a TM_z polarized Bessel beam. It is important to note that the radiated fields do not change significantly with frequency, meaning the device exhibits minimal dispersion.

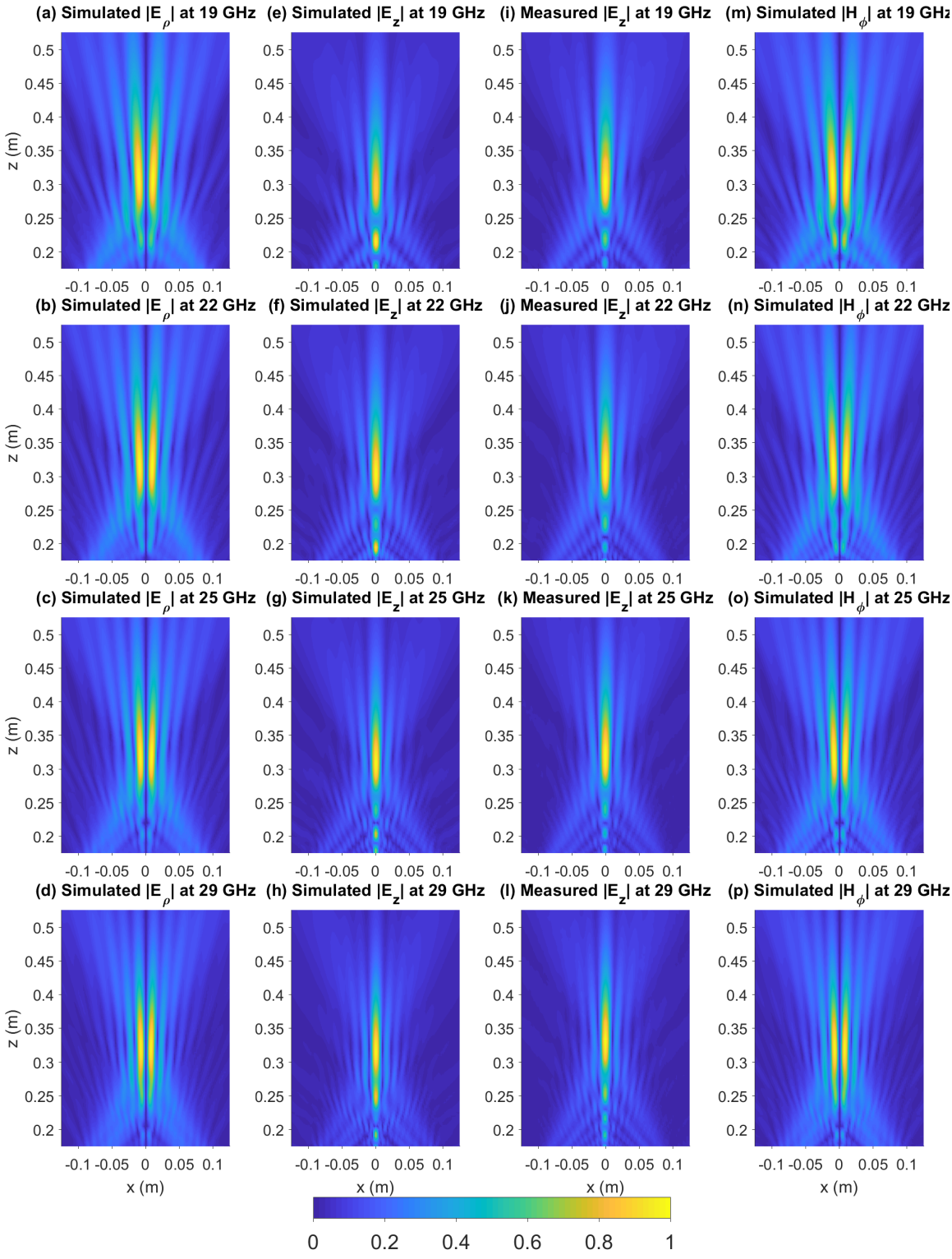

Figure 3.3: Magnitude of the fields generated by the Bessel beam radiator at 19, 22, 25 and 29 GHz along the $y = 0$ plane: (a-d) simulated $|E_\rho|$, (e-h) simulated $|E_z|$, (i-l) measured $|E_z|$, and (m-p) simulated $|H_\phi$.

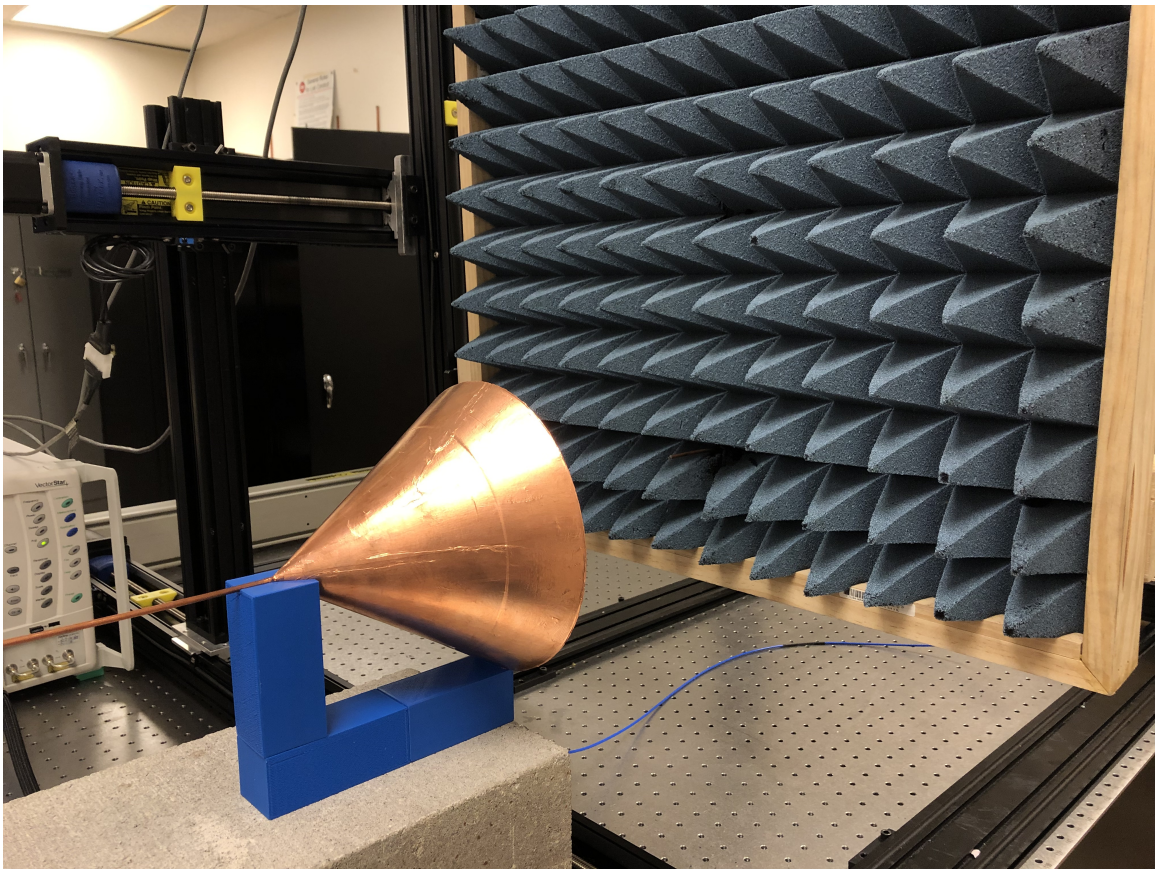

Figure 3.4: Measurement setup used to scan the $\widehat{z}$-directed electric field emitted by the radiator. The fields were measured using a coaxially fed electric monopole acting as a probe, attached to a three-dimensional translation unit. The probe and radiator were connected to the two ports of the vector network analyzer.

In Fig. 3.5, the magnitude of the simulated E_ρ (first column) and simulated and measured E_z (second and third columns, respectively) along the $z = 0.325$ m plane are shown at the same four frequencies. In Fig. 3.6(a-d), the E_z quantities are plotted along the $y = 0$ line of the same plane, for a clearer comparison. Finally, Figs. 3.6(e-h) presents the angular distribution of the fields generated by the radiator, obtained by performing a spatial Fourier transform of E_z along the $z = 0.325$ m plane. All quantities have been normalized between 0 and 1.

From the angular distribution plot, it is evident that the radiator exhibits high purity in its spatial spectrum. By squaring the angular distribution of simulated E_ρ and integrating between the two local minima surrounding the peak, it is found that over 89% of the radiated power contributes to the Bessel beam with the prescribed cone angle. Moreover, this angle does not change significantly with frequency (approximately 2° over the entire bandwidth of operation) meaning that all frequency components of a pulse emanated by

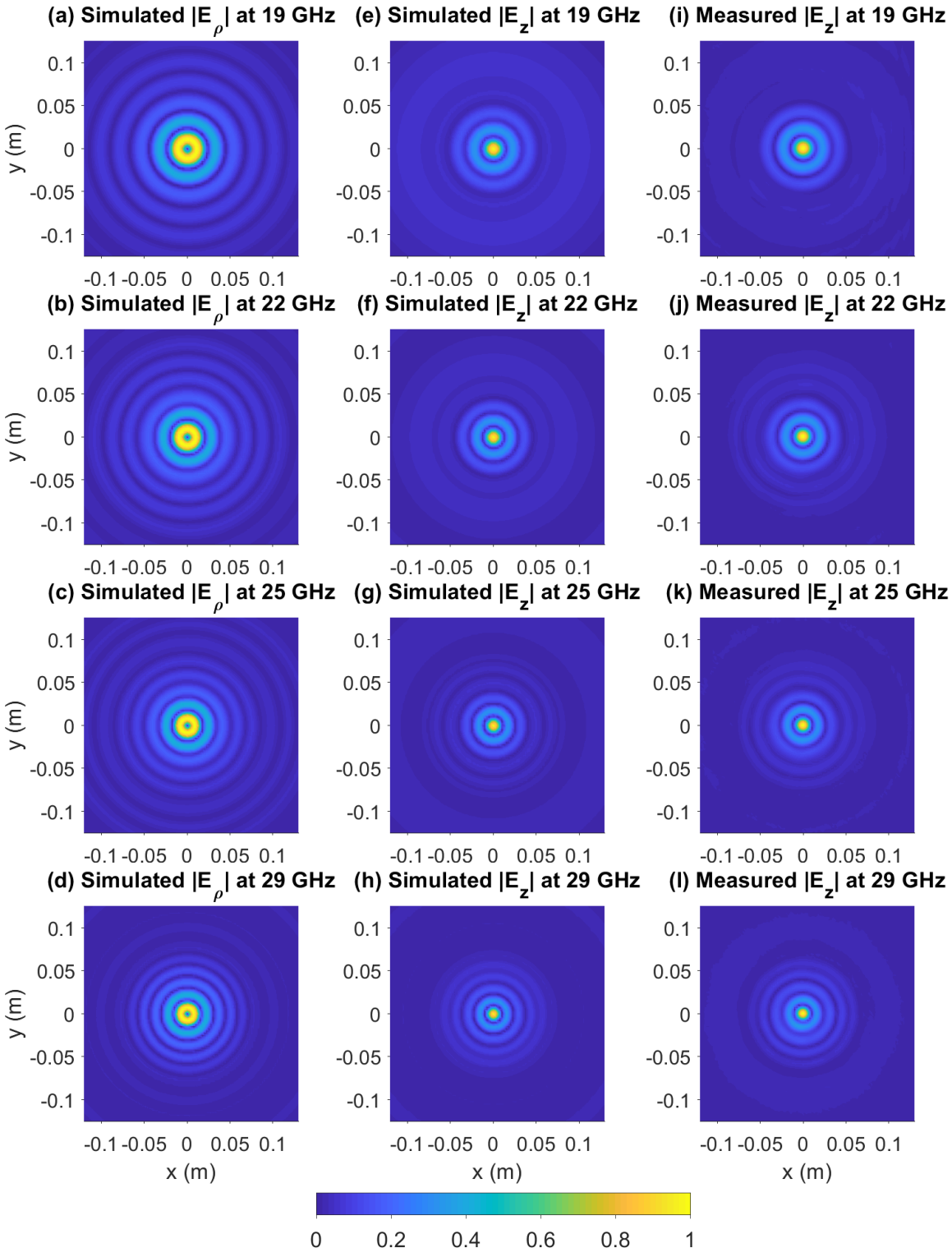

Figure 3.5: Magnitude of the fields generated by the Bessel beam radiator at 19, 22, 25 and 29 GHz along the $z = 0.325$ m plane: (a-d) simulated $|E_\rho|$, (e-h) simulated $|E_z|$, and (i-l) measured $|E_z|$.

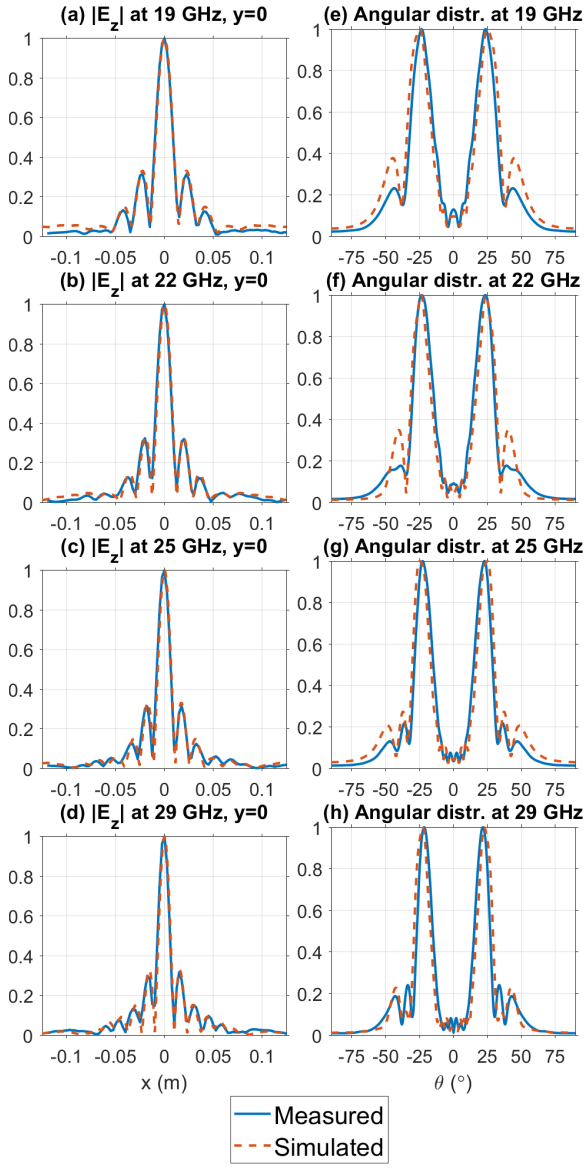

Figure 3.6: Fields generated by the Bessel beam radiator at 19, 22, 25 and 29 GHz along the $z = 0.325$ m plane: (a-d) simulated and measured $|E_z|$ at $y = 0$, and (e-h) simulated and measured angular distribution of E_z.

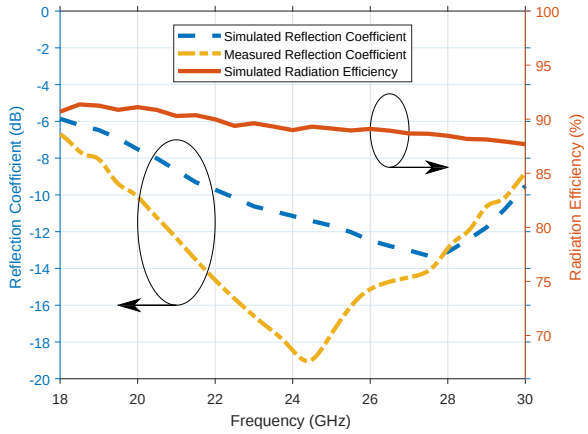

Figure 3.7: Simulated (blue) and measured (yellow) reflection coefficient of the radiator (left axis), as well as radiation efficiency (red—right axis), as a function of frequency.

the radiator possess approximately the same phase and group velocity: $v = c/\cos\theta_2$, where c is the speed of light. As a result, the pulse stays confined as it propagates.

In Fig. 3.7, the simulated and measured input reflection coefficients (S_{11}) of the structure are plotted as a function of frequency (left vertical axis). The conical flare acts as a wideband impedance matching mechanism, resulting in low reflections. The measured reflection coefficient is lower than the simulated one, due to the losses in the Rexolite region (the loss tangent is higher in this frequency range compared to its value at 10 GHz), and the slightly smoother transition from the coaxial cable to the Bessel beam radiator compared to simulation. The radiation efficiency of the structure is calculated in COMSOL as the ratio of power exiting the structure over the power that is input into it (right vertical axis). It can be seen that the radiator is highly efficient.

3.4 X Wave Generation

An X wave is a pulse consisting of different frequency Bessel beams with the same cone angle. The wave function describing an X wave (E_z for a TM_z Bessel beam) is [73]:

$$E_z(\rho, z, t) = \int_{-\infty}^{\infty} F(k_0) J_0\left(k_0 \sin\theta_2 \rho\right) e^{jk_0(ct - \cos\theta_2 z)} dk_0, \tag{3.5}$$

where $F(k_0)$ are the spectral coefficients. For simplicity, assume that the frequency spectrum of the excitation signal applied to the input of the radiator is uniform from 22 to 29 GHz (widest bandwidth that can be obtained from the arbitrary waveform generator available to the authors). This leads to the input waveform pulse shown in Fig. 3.8(a).

Using the experimentally measured E_z along the $y = 0$ plane (captured at $N_f = 935$

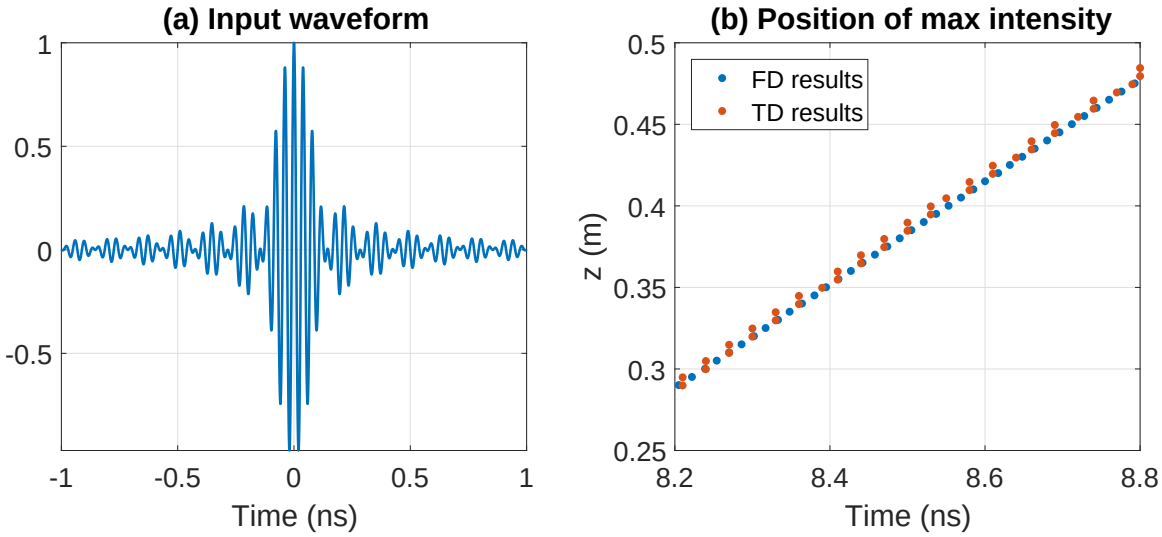

Figure 3.8: (a) Uniform spectrum waveform (22-29 GHz) that is used to observe an X wave, and (b) position of maximum intensity along the z-axis as a function of time for both frequency domain and time domain results.

frequency points between 22 and 29 GHz), the field generated under the pulse excitation of Fig. 3.8(a) is calculated. Specifically, for every point along the $y = 0$ plane, E_z can be calculated for any time t as

$$E_z(x, z, t) = \sum_{i=1}^{N_f} E_z(x, z, \omega_i) e^{j\omega_i t}, \tag{3.6}$$

where $E_z(x, z, \omega_i)$ denotes the measured field at each angular frequency ω_i at (x, z) [73]. The intensity of E_z (normalized between 0 and 1) is plotted in Fig. 3.9(a-d) at four different times (t = 8.07, 8.30, 8.52, and 8.75 ns). A detailed treatment of the effects of finite bandwidth, frequency dispersion and aperture on the shape of the emitted pulses can be found in Appendix B. The real part of E_z (normalized between -1 and 1) is plotted in Fig. 3.9(e-h). The generated fields are rotationally symmetric about the z-axis, meaning that a bulletlike pulse is emitted. The X wave is highly confined in the transverse plane and propagates with little dispersion and diffraction in the longitudinal direction within the nondiffracting range of the radiator: $z = 0.16$ to 0.44 m. Once the pulse has passed this range (see last row of Fig. 3.9), the effects of dispersion begin to appear.

To further showcase the radiator's ability to produce X waves, measurements were also taken in the time domain. These experiments were performed at the U.S. Naval Reseach Laboratory (NRL) by Scott Rudolph and Victor Mendez. The longitudinal electric field was again observed in the region above the radiator when excited with the waveform shown

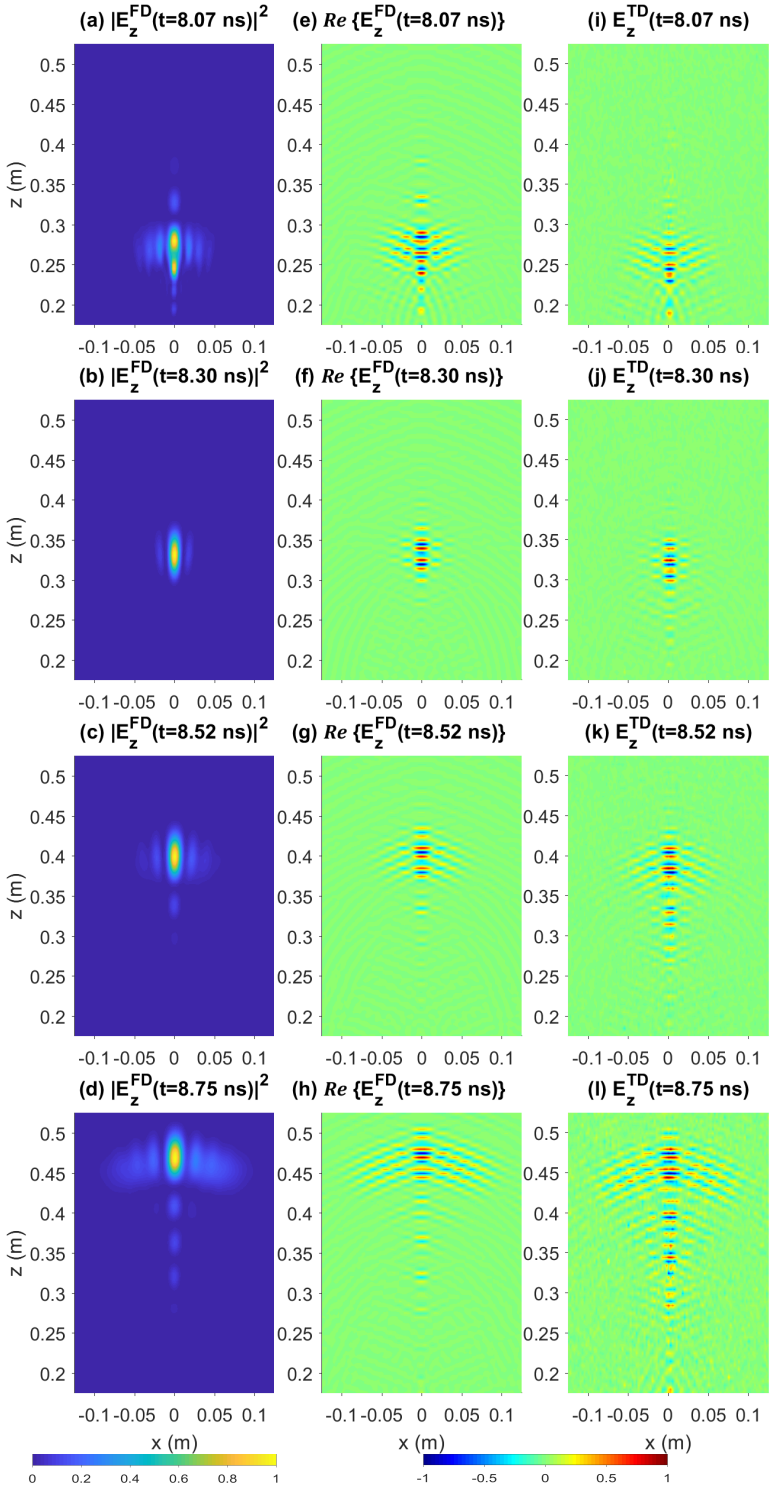

Figure 3.9: (a-d) Instantaneous intensity of E_z in the region above the radiator based on frequency domain measurement results. The evolution of the X wave can be seen at four different time steps. (e-h) Real part of E_z. (i-l) E_z in the region above the radiator based on time domain measurement results.

in Fig. 3.8(a). The details of the experimental procedure and the post-processing operations are given in Appendix C. The X wave emitted by the radiator as a result of this sub-nanosecond input signal is presented at four time steps in Fig. 3.9(i-l).

The superluminal behavior of the X wave [13] is verified in Fig. 3.8(b), which shows the position of maximum intensity along the z-axis as a function of time. From the linear regression of the frequency domain results, the velocity of the wave is found to be $v^{\text{FD}} = c/\cos(17.85^\circ) = 1.05c$, which is slightly lower than that from the linear regression of the time domain results: $v^{\text{TD}} = c/\cos(19.29^\circ) = 1.06c$. Both results are in line with the expected velocity from the COMSOL simulation: $c/\cos(18.70^\circ) = 1.06c$.

To the best of the authors' knowledge, this is the first device capable of generating X waves where the vectorial nature of the fields has been thoroughly examined in experiment. The generated X waves exhibit polarization purity: a well-defined TM_z polarization. The radiator exhibits 2° of cone angle dispersion over a 50% fractional bandwidth. The radiator presented in [79] exhibits 24° of cone angle dispersion over a 21% fractional bandwidth.

3.5 Chapter Summary

The Bessel beam radiator, a device capable of generating TM polarized Bessel beams over a broad bandwidth, was reported. A geometrical optics design process was used to ensure that the Bessel beams emerge at a specified angle over a wide range of frequencies. First, the radiator's operation was verified in simulation. The device was then fabricated and tested, with measurements in close agreement with simulations. Through these measurements, it was shown that the radiator emits X waves under a broadband excitation, the first such demonstration at microwave frequencies. This device could find application in high resolution near field imaging, wideband near field communication, or ground penetrating radar.

CHAPTER 4

Nondiffracting Waves: Metamaterial Bessel Beam Radiator

In the previous chapter, we introduced a Bessel beam and X wave radiator with a 20° cone angle operating between 18 and 30 GHz. It was the first fully characterized X wave launcher in literature.

In this chapter, a second Bessel beam and X wave radiator is developed. The primary goal of this work is to design a paraxial radiator that possesses an extended nondiffracting range. As a result, the Bessel beams and X waves emanated by it can be observed at greater distances relative to the aperture size.

4.1 Chapter Introduction and Outline

Localized waves have received significant attention by researchers in recent years, especially since the introduction of Bessel beams [13, 18]. These beams are exact, superluminal solutions to the Helmholtz equation that do not diffract as they propagate. They can be seen as the result of the interference of all plane waves forming a common angle, called the cone angle, with the propagation axis. Although ideal Bessel beams require infinite energy, truncated Bessel beams are practically realizable. Such beams maintain their nondiffractive properties within a finite range of distances.

X waves are one class of Bessel pulses [38]. They are formed by the superposition of a spectrum of Bessel beams possessing a common cone angle. X waves are appealing because they propagate without suffering from diffraction (spatial spreading) or dispersion (temporal spreading) within their nondiffracting range. These properties make X waves prime candidates for use in imaging [80], tissue characterization [81], communications [33], nondestructive evaluation of materials [82], and focusing [83].

X waves are difficult to generate at microwave frequencies, which partially explains the lack of relevant practical demonstrations in literature. A device generating X waves should

exhibit little or no dispersion (dependence of cone angle on frequency) over an appreciable bandwidth. The cost of broadband sources is also an impeding factor. Should these hurdles be overcome, there is high potential for microwave X waves in heating [84], medicine [85], microscopy [86], high power electromagnetic pulses [87], or ground penetrating radar applications [88].

A device capable of generating X waves at microwave frequencies was presented in the previous chapter. Based on geometrical optics, it converts the radiation from an electrically small monopole into Bessel beams with nearly constant cone angle between 18 and 30 GHz. In earlier research, a parabolic dish was used to verify the superluminality of X Waves [74]. A radial waveguide loaded with radiating slots [73] as well as leaky wave antennas [89, 79] have also been suggested as potential ways to excite X Waves at microwave and millimeter wave frequencies. However, these devices exhibit more pronounced dispersion. Here, a new device is presented, able to emit paraxial Bessel beams and X waves between 7.5 and 12.5 GHz. It is designed using quasiconformal transformation optics (QCTO), implemented with metamaterials, and fabricated through 3D printing. Preliminary results on the design methodology were reported in [36, 37].

Transformation electromagnetics provides arbitrary control of electromagnetic fields through control of constitutive material parameters (permittivity and permeability) as functions of space (inhomogeneity) and direction (anisotropy) [90]. QCTO is a 2D method of manipulating fields that only requires control of permittivity as a function of space [91]. Permeability, which is more difficult to control, is constant, while both permittivity and permeability are isotropic. This technique is used here to design a 3D device that possesses rotational symmetry about the $\widehat{z}$-axis, and as a result can be reduced to a 2D problem [92].

An exponentially tapered Impedance Matching Layer (IML) is added to the permittivity profile obtained from QCTO to reduce reflections at the interface with air [23]. The combined permittivity profile is implemented using rotationally symmetric metamaterial unit cells which are homogenized and modeled with effective permittivities [93]. The resulting device is fabricated through 3D printing, an additive manufacturing technique that is suitable for electromagnetic metamaterials [94]. In this work, three filaments of different permittivity values are used and the parts are later combined. Metamaterial structures requiring multiple filaments can be potentially fabricated in a single run [95].

The design of the tranformation region based on QCTO, together with the design of the IML, is presented in Sec. 4.2. The validity of the design is verified by comparing the electric field generated by this structure to that of an ideal Bessel aperture, computed using a full wave solver. The metamaterial implementation of the radiator using rotationally symmetric unit cells is outlined in Sec. 4.3, along with the corresponding simulation results.

In Sec. 4.4, the fabrication procedure and the challenges associated with it are explained. Measurement results from a fabricated prototype are also given, showing good agreement to those expected from simulation. Sec. 4.5 showcases the device's ability to generate X waves in its radiative near field when excited with a uniform spectrum pulse between 7.5 and 12.5 GHz. Finally, Sec. 4.6 presents concluding remarks.

4.2 Design of X Wave Radiator

Consider an electrically small monopole radiating in a conical region with apex angle θ_1 and relative permittivity ϵ_{r1}, as shown in Fig. 3.1(a). The monopole is situated at the apex of the cone, which is bounded by perfect electric conductor (PEC) shown in orange. The monopole is formed by extending the inner conductor of the coaxial cable feeding it by length p, which, together with θ_1 and ϵ_{r1}, controls the input impedance of the device. The coaxial cable has inner radius ρ_{in} and outer radius ρ_{out}, as shown in the inset of Fig. 3.1(a). The generated electric field has a $\widehat{\rho}$ and $\widehat{z}$ components, whereas the magnetic field only has a $\widehat{\phi}$ component. This field will be converted into a TM Bessel beam.

The equiphase surfaces of the fields emitted by the monopole will be approximately spheres centered at the origin. Two such surfaces are chosen for the analysis that follows, one having radius r_{in} and one having radius r_{out}. The region between the two spheres constitutes the original region and is expressed in terms of (ρ, ϕ, z) cylindrical coordinates.

The region using (ρ', ϕ', z') coordinates in Fig. 4.1(b) is also investigated. The parameters for the coaxial cable and monopole comprising the feed are kept the same. This region possesses a flat surface at $z' = r_{out}$, and is truncated to a maximum radius of ρ_{max}. The truncation ensures that the permittivity profile obtained from QCTO at a later step will not contain unrealizably small permittivity values. The apex angle is still θ_1, but the region in Fig. 4.1(b) has an inhomogeneous relative permittivity $\epsilon_{r2}(\rho', z')$. It constitutes the transformed region.

It is desired that the two regions presented in Fig. 4.1(a) and (b) behave similarly, meaning that the flat surface in the transformed region should also constitute an equiphase surface. Because of the problem's cylindrical symmetry about the $\widehat{z}$-axis, this results in the generation of a paraxial Bessel beam. Moreover, this symmetry means that these 3D regions can be treated as 2D surfaces, and analyzed using QCTO [92].

Fig. 4.2(a) and (b) show the original and transformed regions in 2D, respectively. In these figures, the mesh for the two regions is also shown. The mesh is obtained by solving Laplace's equation in each region, subject to appropriate boundary conditions [92]. First, Neumann boundary conditions are applied on edges 1 and 3, and Dirichlet boundary con-

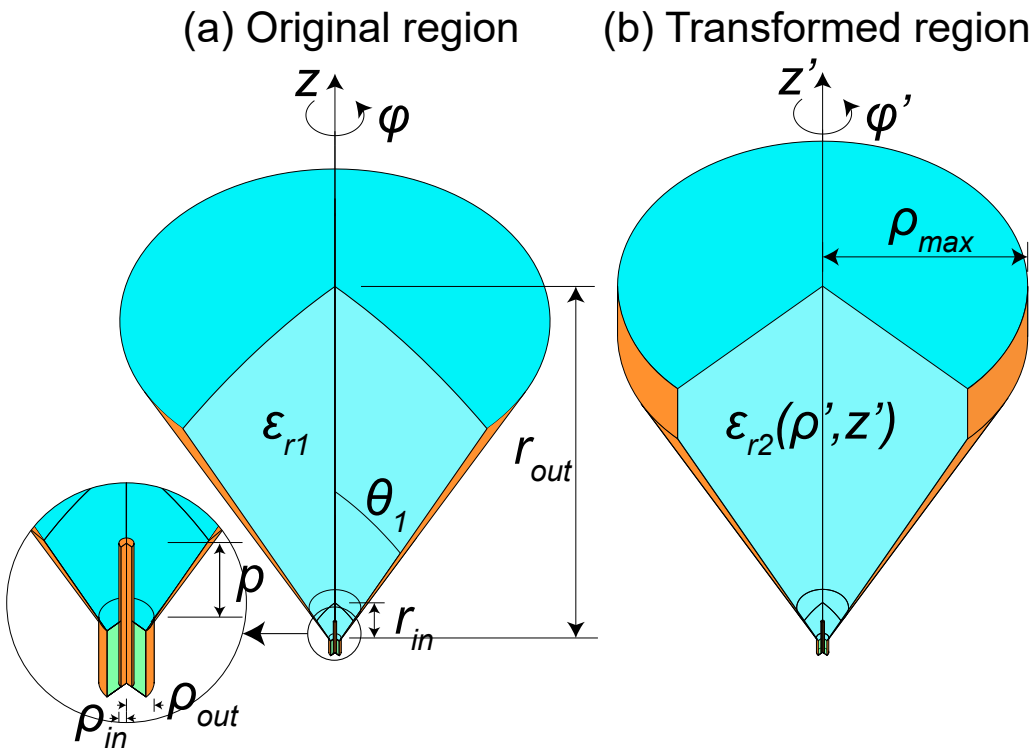

Figure 4.1: (a) The original region, comprising a coaxially fed monopole radiating in a conical region of homogeneous permittivity ϵ_{r1}, and bounded by a spherical surface at $r = r_{out}$. (b) The transformed region, utilizing the same feeding mechanism, having an inhomogeneous permittivity $\epsilon_{r2}(\rho', z')$ and bounded by a flat surface at $z' = r_{out}$.

ditions on edges 2 and 4. The edge numbers are shown in red. After solving Laplace's equation, a contour plot of the solution's amplitude yields the isocentric curves in Fig. 4.2(a). Then the straight, spokes-like curves in Fig. 4.2(a) are obtained by applying Dirichlet boundary condition on edges 1 and 3, and Neumann boundary conditions on edges 2 and 4. Similar boundary conditions are applied on the transformed region.

Once the two regions are meshed, for each point in the mesh

- we store the ρ values of the 3×3 grid surrounding the point in a matrix, $\boldsymbol{\rho}$,
- we store the z values of the 3×3 grid surrounding the point in a matrix, $\boldsymbol{z}$,
- we store the ρ' values of the 3×3 grid surrounding the point in a matrix, $\boldsymbol{\rho'}$,
- we store the z' values of the 3×3 grid surrounding the point in a matrix, $\boldsymbol{z'}$,
- we find the fitting coefficients, C_0, C_1, and C_2 such that $\boldsymbol{\rho'} \approx C_0 + C_1\boldsymbol{\rho} + C_2\boldsymbol{z}$, and
- we find the fitting coefficients, D_0, D_1, and D_2 such that $\boldsymbol{z'} \approx D_0 + D_1\boldsymbol{\rho} + D_2\boldsymbol{z}$.

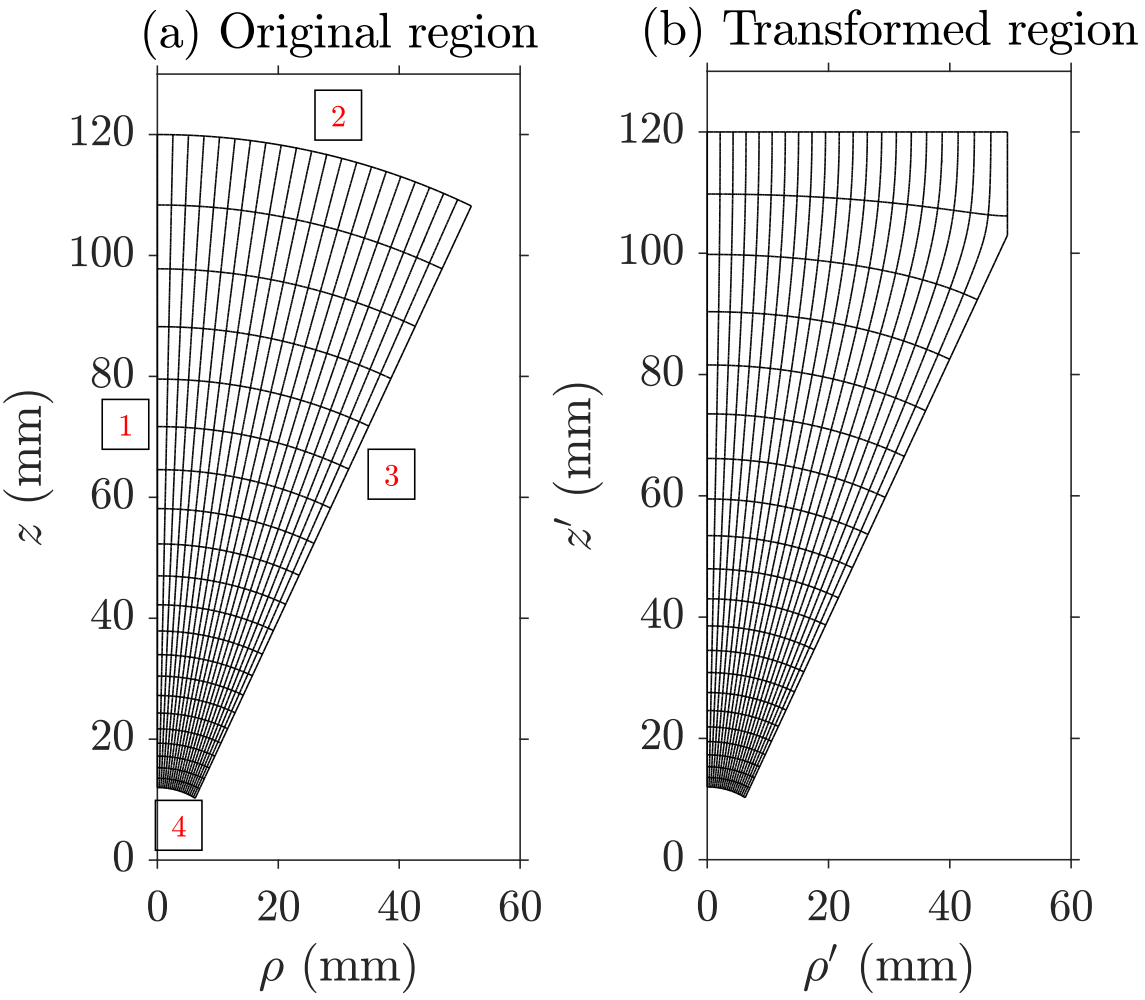

Figure 4.2: (a) Original, and (b) transformed regions in 2D, used in QCTO.

From this process, the coefficients C_0, C_1, C_2, D_0, D_1, and D_2 are calculated for each point in the mesh. These coefficients will be used to calculate the Jacobian matrix of the transformation. This technique can be better illustrated through an example. A point (denoted by a star) together with the surrounding 3×3 grid (denoted by dots) is shown in Fig. 4.3(a) in the original region, and in Fig. 4.3(b) in the transformed region.

For this point, the following matrices are constructed:

(a) Zooming in on the original region (b) Zooming in on the transformed region

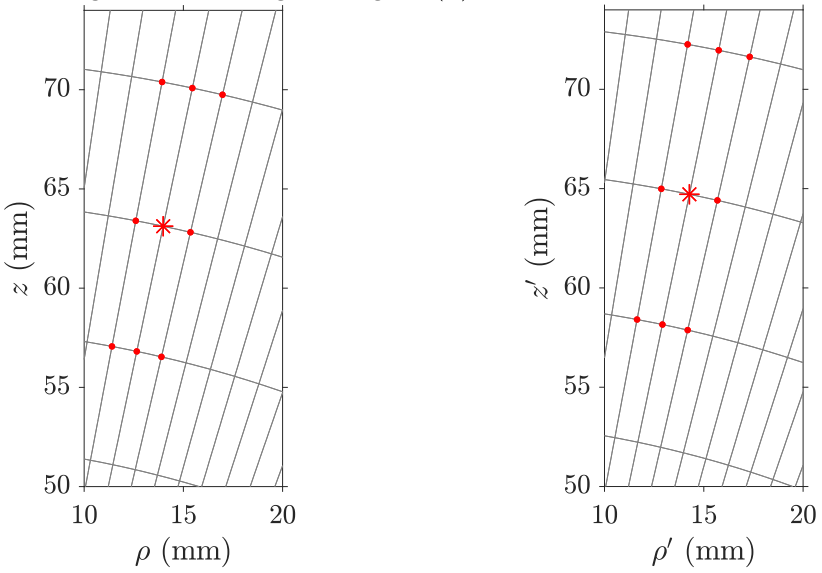

Figure 4.3: The 3×3 grid (denoted by dots) around a point (denoted by a star) in (a) the original region and (b) the transformed region. This point is used to illustrate the procedure followed in order to calculate the Jacobian of the transformation.

$$
\begin{aligned}
\boldsymbol{\rho} &= \begin{bmatrix} 0.011402 & 0.012652 & 0.013895 \\ 0.012602 & 0.013984 & 0.015357 \\ 0.013928 & 0.015453 & 0.016972 \end{bmatrix}, \\
\boldsymbol{z} &= \begin{bmatrix} 0.057064 & 0.056813 & 0.056537 \\ 0.063396 & 0.06312 & 0.062816 \\ 0.070388 & 0.070083 & 0.069747 \end{bmatrix}, \\
\boldsymbol{\rho'} &= \begin{bmatrix} 0.011639 & 0.012917 & 0.014188 \\ 0.012861 & 0.014275 & 0.015685 \\ 0.014187 & 0.015752 & 0.017312 \end{bmatrix}, \\
\boldsymbol{z'} &= \begin{bmatrix} 0.058408 & 0.058156 & 0.057878 \\ 0.064989 & 0.064713 & 0.064409 \\ 0.072261 & 0.071965 & 0.071636 \end{bmatrix}.
\end{aligned}
\tag{4.1}
$$

Using MATLAB's fitting function, the primed matrices are fitted to the unprimed ones:

Table 4.1: Values of design variables

Design variable	Value
ρ_{in}	0.455 mm
ρ_{out}	1.485 mm
p	11.3 mm
θ_1	25°
r_{in}	12 mm
r_{out}	120 mm
ρ_{max}	49.5 mm
t	9 mm
ϵ_{r1}	5.4
ϵ_{r2}	$2.90 - 7.36$
$\epsilon_{r,IML}$	$1.00 - 6.77$

$$\begin{aligned} \boldsymbol{\rho'} &\approx 0.00010666 + 1.0245\boldsymbol{\rho} - 0.0026006\boldsymbol{z}, \\ \boldsymbol{z'} &\approx -0.00097243 + 0.0097066\boldsymbol{\rho} + 1.0386\boldsymbol{z}. \end{aligned} \tag{4.2}$$

As a result, for this example, the fitting coefficients are:

$$\begin{aligned} C_0 = 0.00010666, \quad C_1 = 1.0245, \quad C_2 = -0.0026006, \\ D_0 = -0.00097243, \quad D_1 = 0.0097066, \quad D_2 = 1.0386. \end{aligned} \tag{4.3}$$

Using the design equations originally presented in [91] and in a more compact way in [92], the relative permittivity profile of the transformed region is calculated as

$$\epsilon_{r2}(\rho', z') = \frac{\epsilon_{r1}}{|\det(\mathbf{J}(\rho', z'))|}, \tag{4.4}$$

where

$$\mathbf{J}(\rho', z') = \begin{bmatrix} \frac{\partial \rho'}{\partial \rho} & \frac{\partial \rho'}{\partial z} \\ \frac{\partial z'}{\partial \rho} & \frac{\partial z'}{\partial z} \end{bmatrix} = \begin{bmatrix} C_1 & C_2 \\ D_1 & D_2 \end{bmatrix} \tag{4.5}$$

is the Jacobian matrix of the transformation at each point of the transformed region. The determinant of the Jacobian matrix is shown in Fig. 4.4.

The resulting permittivity profile, shown in Fig. 4.5(a), is smooth, and agrees with intuition from gradient index optics, where rays bend towards regions of higher permittivity. The relative permittivity of the original region, ϵ_{r1}, was chosen so that the relative permittivity of the transformed region falls within a range that can be realized through 3D

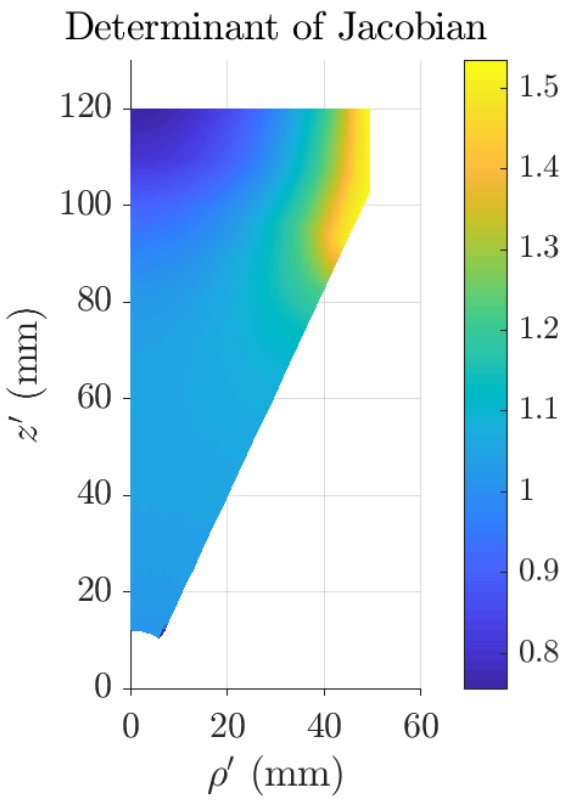

Figure 4.4: The determinant of the Jacobian matrix, calculated using (4.5).

printing. The overall dimensions were also decided on based on fabrication capabilities and constraints. Table 4.1 summarizes the design variables and their values.

The next step in the design process is to apply an IML of thickness t to the transformed region to minimize reflections caused by the high contrast of refractive indices at the flat interface (assuming the device is surrounded by air). An exponential taper was selected for the IML instead of a quarter wavelength transformer [96]. As a result, the IML is thicker, but it also provides an impedance match over a broader bandwidth. Its dielectric constant is

$$\epsilon_{r,IML}(\rho', z') = \epsilon_{r2}(\rho', r_{out}) e^{-\ln(\epsilon_{r2}(\rho', r_{out}))(z' - r_{out})/t}, \tag{4.6}$$

where $\epsilon_{r2}(\rho', r_{out})$ is the dielectric constant at the interface, as calculated from QCTO.

The final dielectric constant profile, comprising the transformed region and the IML, is shown in 2D in Fig. 4.5(b). The radiator possessing this permittivity profile was simulated at three frequencies, 7.5, 10, and 12.5 GHz, in the axially symmetric solver of COMSOL Multiplhysics. The amplitude of the longitudinal ($\widehat{z}'$-directed) electric fields in the region over the radiator are shown in Fig. 4.6(a-c) when a voltage of 1 V excites the coaxial

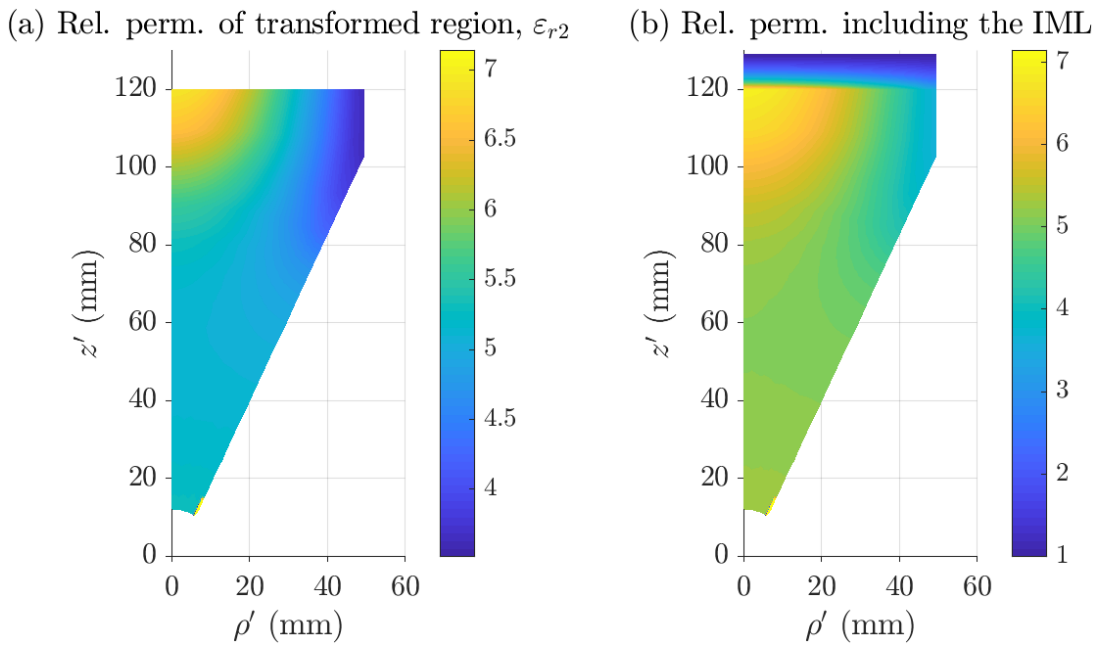

Figure 4.5: The relative permittivity profile of the transformed region (a) before, and (b) after the application of the IML.

cable. The real part (time snapshot) and phase of the fields is shown in Fig. 4.7(a-c) and Fig. 4.8(a-c), respectively. The cone angles of the emitted beams are $\theta = 18°$, $14°$, and $11°$, respectively. The nondiffracting range of the beams, calculated as $\rho_{max}\cot\theta$, is 152, 199, and 255 mm from the aperture, respectively. In order to achieve a smaller cone angle, which would result in a larger nondiffracting range, an electrically larger aperture is required. A larger aperture can produce a beam with narrower beamwidth, allowing the peak to approach broadside.

For comparison, the field generated from ideal Bessel apertures with these cone angles is investigated. The aperture has tangential electric field profile at $z' = r_{out} + t$ given by

$$E_\rho(\rho') \propto J_1(k_0 \sin\theta \rho'), \quad \rho' \leq \rho_{max}, \tag{4.7}$$

where k_0 is the free space wavenumber. The resulting $\hat{z}'$-directed electric field amplitudes are shown in Fig. 4.6(d-f) at the same three frequencies. Fig. 4.7(d-f) show the real part (time snapshot) of the fields, while Fig. 4.6(d-f) shows the phase. Although not identical, the field profiles appear quite similar, and agree in terms of range.

The reflection coefficient of the radiator including the IML is shown in Fig. 4.9 in blue. The shape of this curve is dictated largely by the reflection coefficient of the monopole, while the rest of the radiator contributes the small scale ripple. A broadband match is observed.

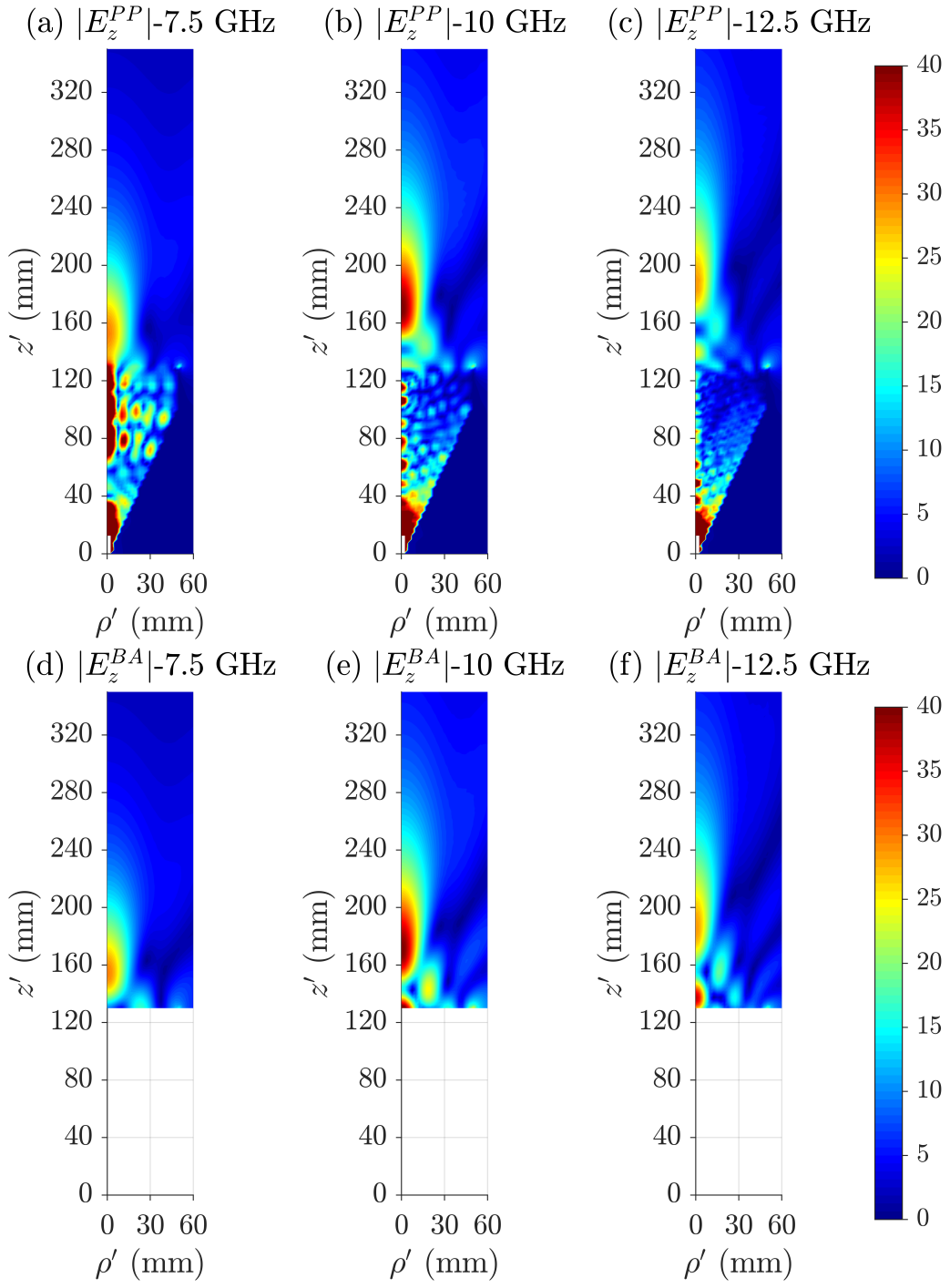

Figure 4.6: (a-c) $|E_z|$ (in V/m) emitted by the permittivity profile of Fig. 4.5(b) at 7.5, 10, and 12.5 GHz, respectively. (d-f) $|E_z|$ emitted by an ideal Bessel aperture at the same three frequencies for comparison.

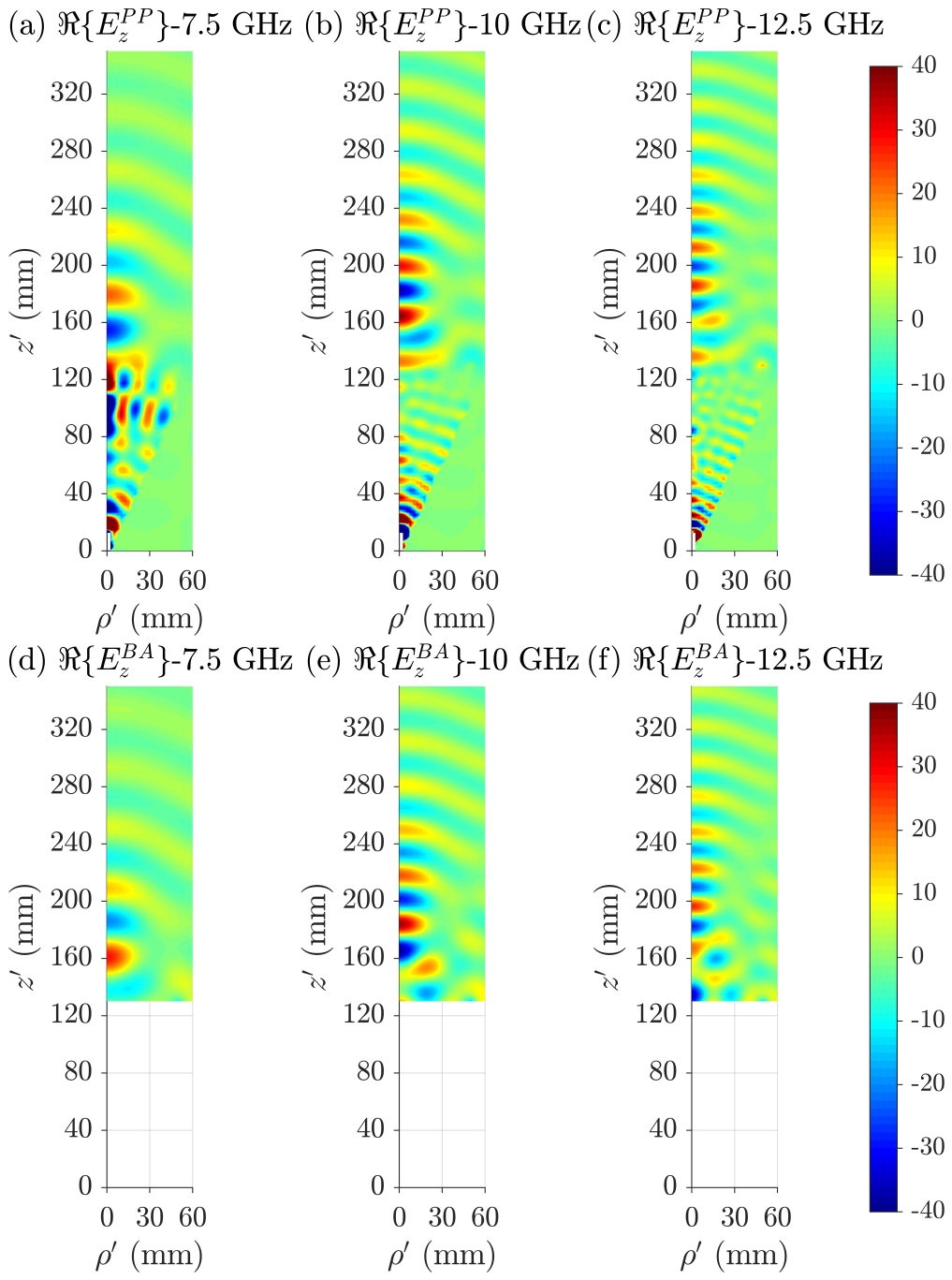

Figure 4.7: (a-c) $\Re\{E_z\}$ (in V/m) emitted by the permittivity profile of Fig. 4.5(b) at 7.5, 10, and 12.5 GHz, respectively. (d-f) $\Re\{E_z\}$ emitted by an ideal Bessel aperture at the same three frequencies for comparison.

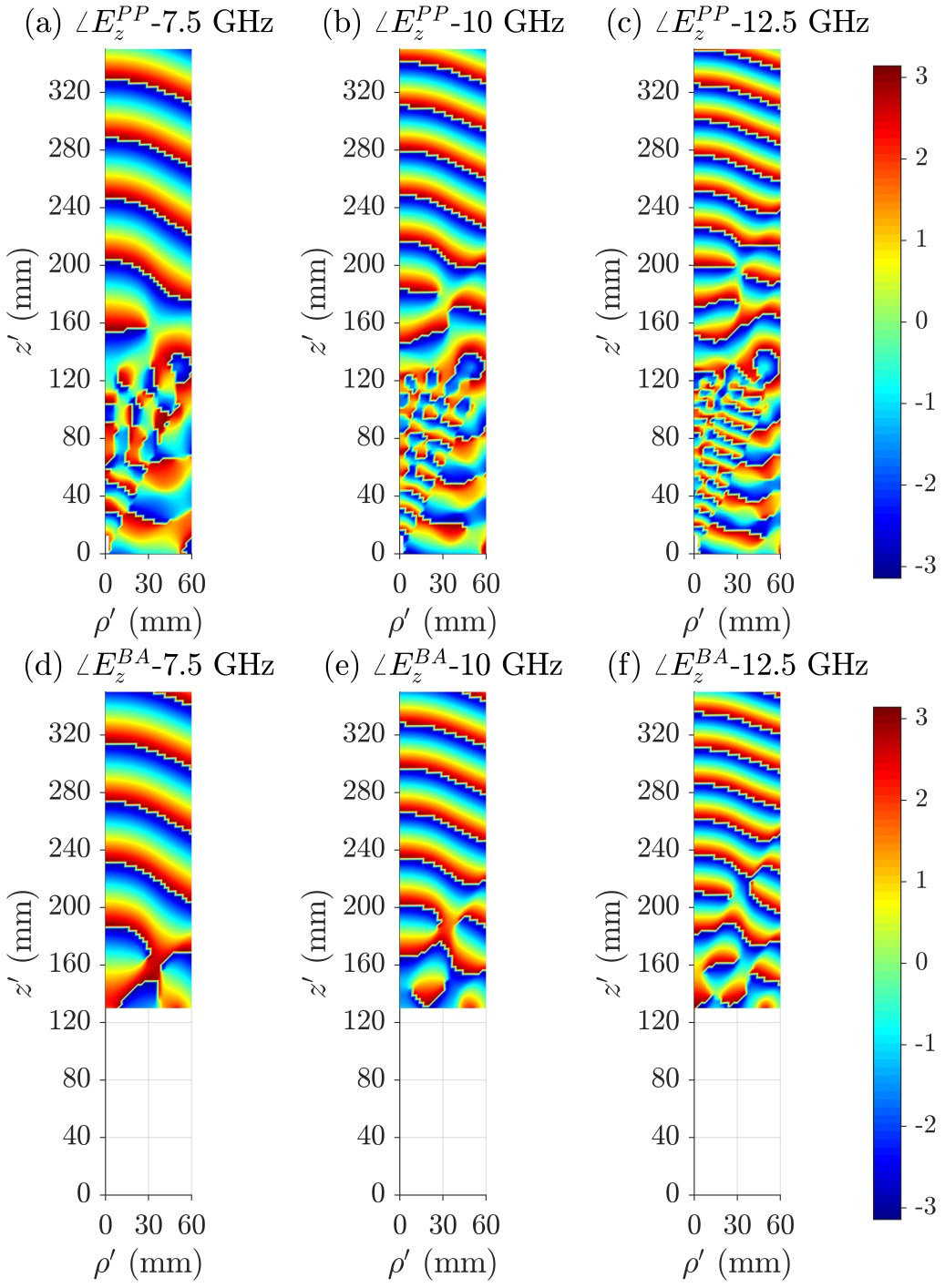

Figure 4.8: (a-c) $\angle E_z$ (in V/m) emitted by the permittivity profile of Fig. 4.5(b) at 7.5, 10, and 12.5 GHz, respectively. (d-f) $\angle E_z$ emitted by an ideal Bessel aperture at the same three frequencies for comparison.

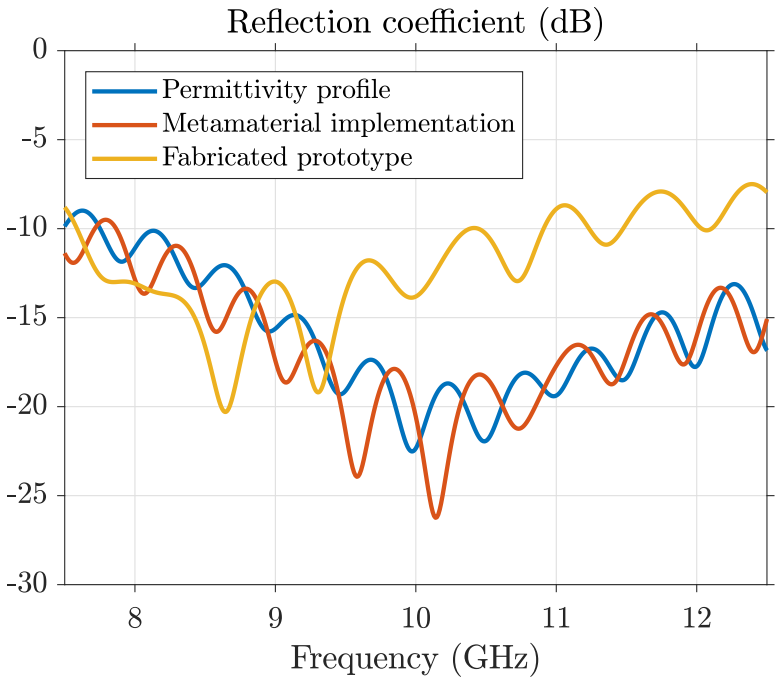

Figure 4.9: The reflection coefficient of the radiator having the permittivity profile of Fig. 4.5(b) (blue), the reflection coefficient of the radiator implemented with metamaterial unit cells (orange), and the reflection coefficient of the fabricated prototype (Fig. 4.16) (yellow).

4.3 Metamaterial implementation

The permittivity profile of Fig. 4.5(a) is implemented using the 2D metamaterial unit cell shown in Fig. 4.10(a). Choosing a 2D unit cell permits the rapid design of the implemented radiator. It consists of a square of side d made from a material with dielectric constant $\epsilon_{r,FIL}$, from which a square of side a has been removed. When swept about the $\widehat{z}'$-axis, it results in circular channels with square cross sections. Other inclusions shapes (circular, diamond) were examined, but this one was found to be the most appropriate for 3D printing. By changing the dielectric constant of the material, $\epsilon_{r,FIL}$, and parameter a, a large range of effective dielectric constants can be achieved with dimensions suitable for 3D printing.

The materials used should exhibit good electromagnetic properties (namely, be low-loss) and possess a controlled dielectric constant. PREPERM filaments offered by PREMIX [97] fulfill these criteria and are used here, specifically the ones with $\epsilon_{r,FIL} = 4.4$, 6.4, and 10. Their loss tangent is $\tan\delta = 0.004$.

The effective dielectric constant is found by simulating the unit cell of Fig. 4.10(a) in COMSOL. Its reflection and transmission coefficients are used to homogenize it into a dielectric slab filled with a material exhibiting the effective dielectric constant. The unit cell size is set to $d = 1.5$ mm. The effective dielectric constant of the unit cell as a function

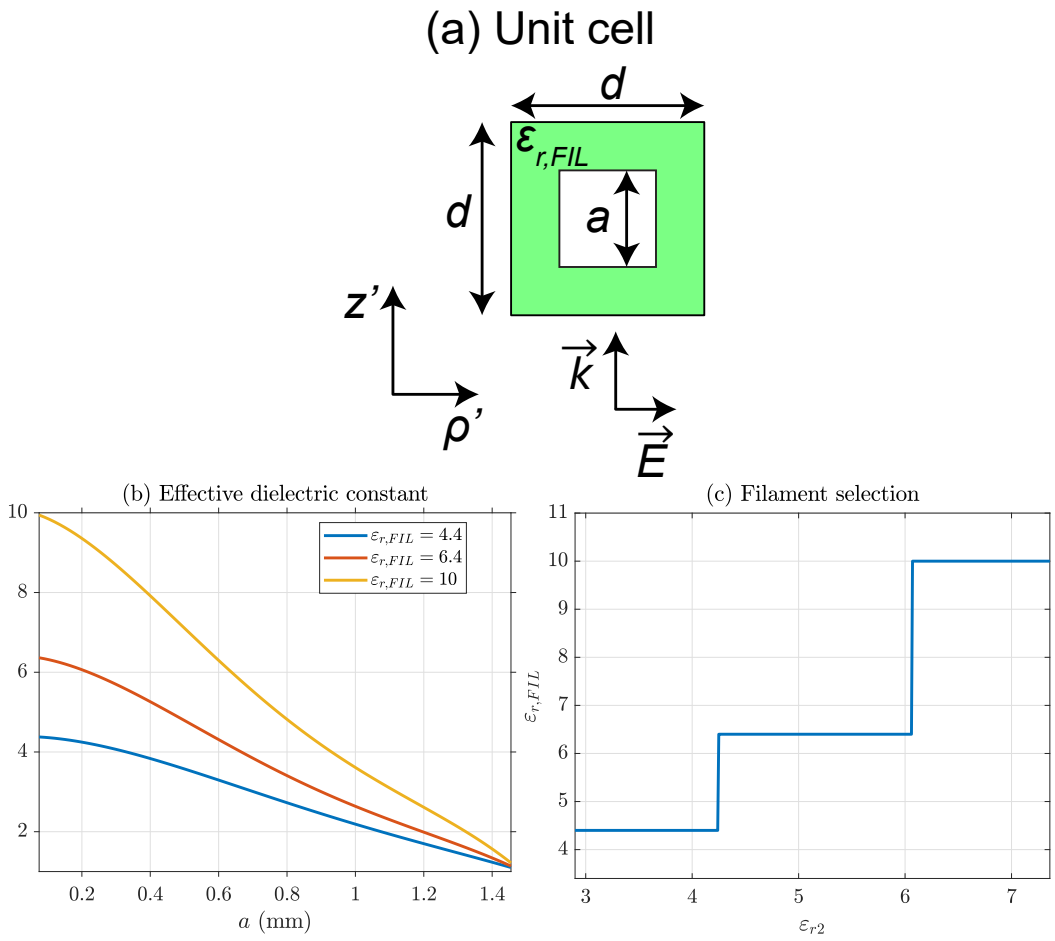

Figure 4.10: (a) Unit cell used to implement the permittivity profile obtained from QCTO. (b) The effective dielectric constant of this unit cell as a function of parameter a for different values of $\epsilon_{r,FIL}$. (c) The model developed to determine which filament should be used to implement a required effective dielectric constant.

of parameter a is plotted in Fig. 4.10(b) for the three filaments.

This unit cell has a uniaxial permittivity tensor with equal values in the $\widehat{\rho}'$- and $\widehat{z}'$-directions and a different one in the $\widehat{\phi}'$-direction. Since the fields emitted by the monopole are always polarized in plane with the unit cell, only the $\widehat{\rho}'$ and $\widehat{z}'$-directed permittivity is relevant.

The model of Fig. 4.10(c) is used to decide which filament should be used depending on the effective dielectric constant needed. It is based on fabrication constraints imposed by 3D printing on the value of parameter a. This parameter must be kept between 0.2 and 0.7 mm. For example, to achieve $\varepsilon_{r2} = 5$ at a specific point of the radiator, the $\varepsilon_{r,FIL} = 6.4$ filament should be used according to Fig. 4.10(c). From the homogenization curves of Fig. 4.10(b), $a = 0.46$ mm is the appropriate value to achieve $\varepsilon_{r2} = 5$ with the $\varepsilon_{r,FIL} = 6.4$ filament. This way the filament permittivity, $\varepsilon_{r,FIL}$, and parameter a can be determined for

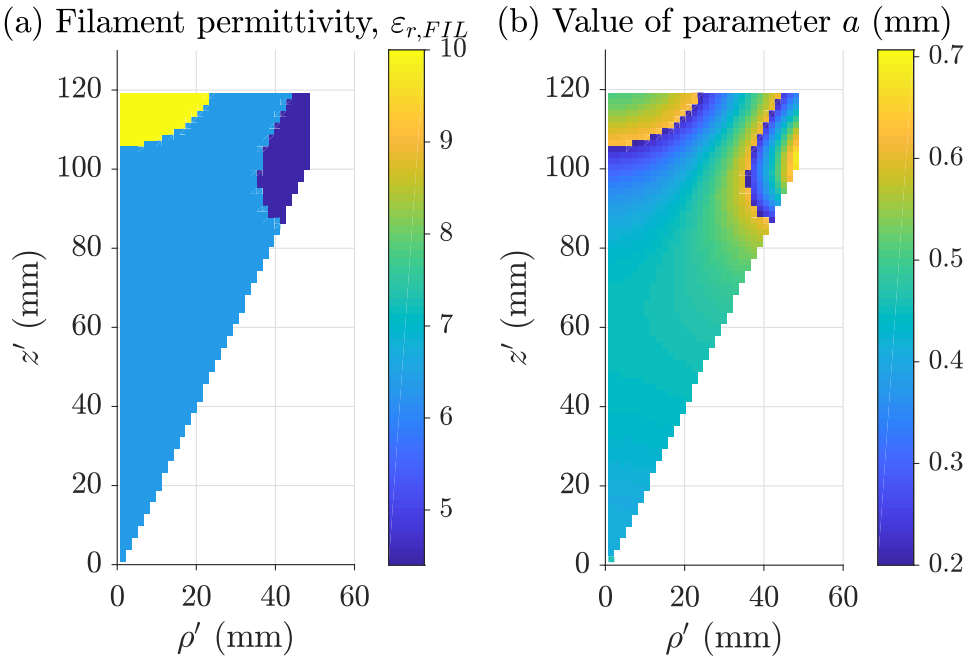

Figure 4.11: (a) Using the permittivity profile of Fig. 4.2(a) and the model of Fig. 4.10(c), the filament to be used at each point of the radiator is determined. (b) Knowing which filament will be used, the value of parameter a is determined using the appropriate homogenization curve in Fig. 4.10(b).

the entire device. Their values are given in Fig. 4.11(a) and (b), respectively.

Applying the same procedure for the IML would result in very large values for a (close to d, even if a filament with $\varepsilon_{r,FIL} = 3$ were to be used), which would be impossible to fabricate through 3D printing. As a result, a different approach is developed to implement the IML.

Specifically, the unit cell of Fig. 4.12(a) is used to implement the IML. It consists of a rectangle with dimensions $b \times d$, made of filament with dielectric constant $\varepsilon_{r,IML} = 6.4$. The unit cell size is $3d \times d$. By changing parameter b, the effective permittivity of the unit cell can be tuned, as shown in Fig. 4.12(b). Implementing the IML portion of the permittivity profile (Fig. 4.5(b)) using the curve in Fig. 4.12(b) results in the distribution for parameter b shown in Fig. 4.12(c).

The design resulting from the metamaterial implementation of the QCTO and IML regions is presented in Fig. 4.13. Each filament is represented by a different color: dark blue - $\varepsilon_{r,FIL} = 4.4$, light blue - $\varepsilon_{r,FIL} = 6.4$, yellow - $\varepsilon_{r,FIL} = 10$. This radiator design is simulated in the axially symmetric solver of COMSOL at the same three frequencies: 7.5, 10, and 12.5 GHz. The results, shown in Fig. 4.14, agree with the ones obtained using the inhomogeneous permittivity profile (Fig. 4.6(a-c)), justifying the metamaterial design

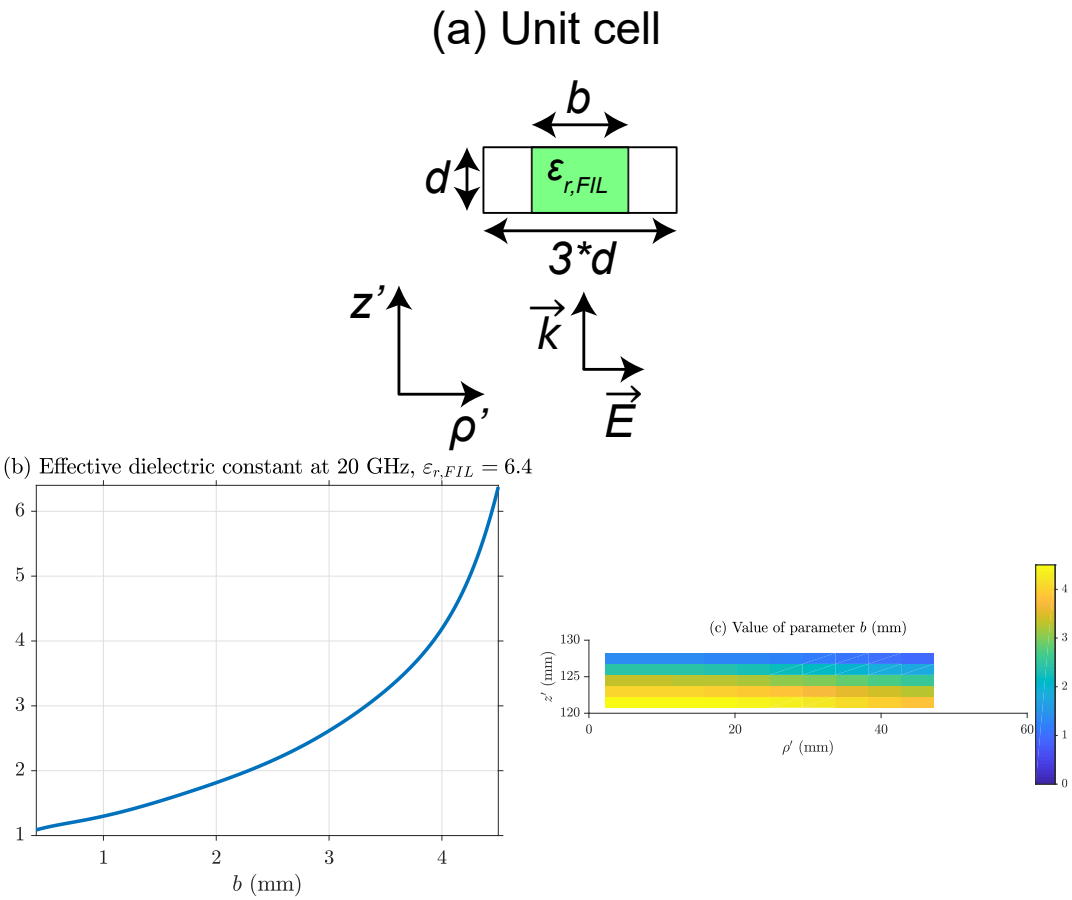

Figure 4.12: (a) Unit cell used to implement the IML portion of Fig. 4.5(b). (b) Effective dielectric constant of this unit cell (using $\varepsilon_{r,FIL} = 6.4$) as a function of parameter b through simulation in COMSOL. (c) Distribution of parameter b in the IML, based on this model and Fig. 4.5(b).

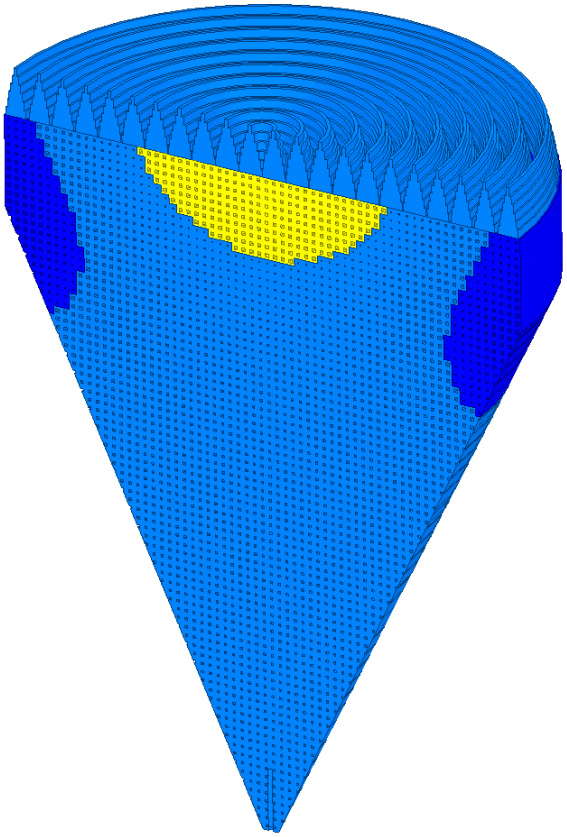

Figure 4.13: The rotationally symmetric metamaterial implementation of the QCTO and IML regions of the radiator. Dark blue: $\varepsilon_{r,FIL} = 4.4$, light blue: $\varepsilon_{r,FIL} = \varepsilon_{r,IML} = 6.4$, yellow: $\varepsilon_{r,FIL} = 10$.

procedure. The reflection coefficient of the metamaterial implementation is also obtained through COMSOL simulations, and is presented in Fig. 4.9 in orange.

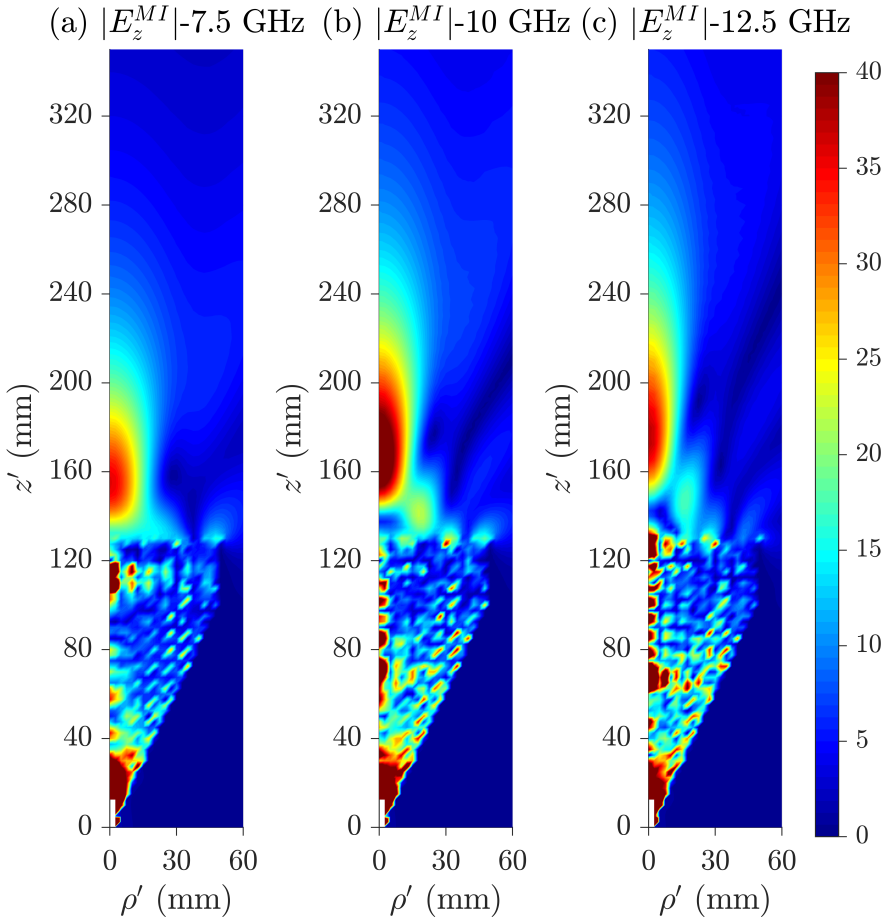

Figure 4.14: $|E_z|$ (in V/m) obtained by simulating the radiator that is implemented with metamaterial unit cells at (a) 7.5, (b) 10, and (c) 12.5 GHz, respectively.

In simulation, the cone angle of the Bessel beam generated by the radiator is also investigated. Specifically, Fig. 4.15 presents the cone angle as a function of frequency between 7.5 and 12.5 GHz. Any practical device will have a dependence of cone angle on frequency. The radiator presented in this chapter exhibits a variation of 7° between 7.5 and 12.5 GHz, or $0.14°/\%$ bandwidth. Bulkier radiators exhibit a smaller variation (2° between 18 and 30 GHz or $0.04°/\%$ bandwidth [35]), while planar ones exhibit larger variation (12° between 18 and 20 GHz, or $1.14°/\%$ bandwidth [79]). A larger cone angle dispersion degrades the confinement of the X wave pulse emitted by the radiator, since the different frequency components will be traveling at different velocities ($v \propto 1/\cos\theta$) [73].

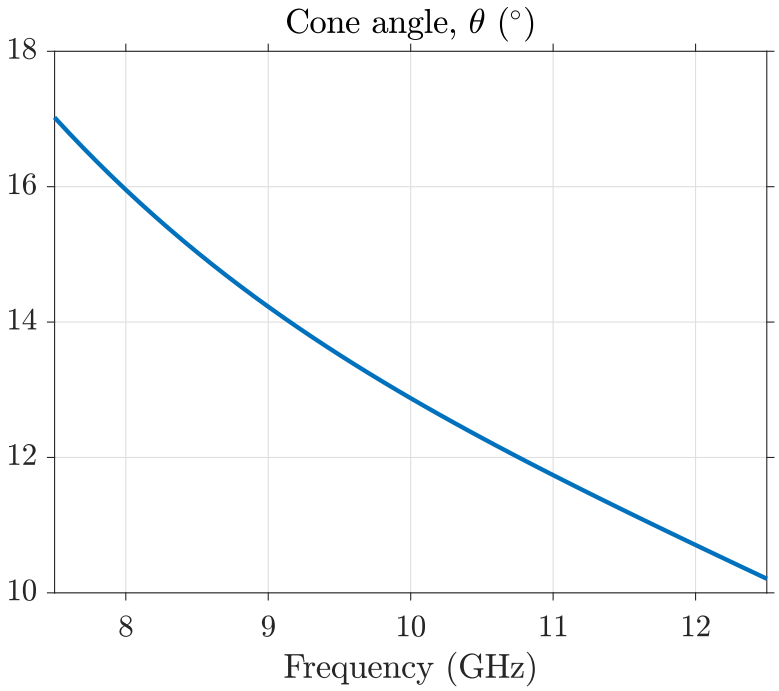

Figure 4.15: Cone angle of the radiator implemented using metamaterial unit cells as a function of frequency.

4.4 Measurement results

The metamaterial radiator was fabricated through 3D printing, using PREPERM filaments, by Dr. Shiyu Zhang at Loughborough University. Each part of the transformed region was manufactured using the appropriate filament (Fig. 4.11(a)) and distribution of parameter a (Fig. 4.11(b)). The IML was also 3D printed using $\epsilon_{r,FIL} = 6.4$, and the distribution of parameter b shown in Fig. 4.12(c). The cross section of the design is shown in Fig. 4.13. All parts were then glued together using acetone by the author. The monopole feeding the device was made from RG402 coaxial cable, and copper foil (3M®1126) was applied to form the conductive cladding. The fabricated prototype is shown in Fig. 4.16.

The fabrication of the parts, as well as their assembly into one structure proved quite challenging:

- Due to the complexity and size of the $\epsilon_{r,FIL} = 6.4$ part, its printing had to be further subdivided into three smaller printing jobs.

- Some of the parts exhibited a bow due to the variation of the temperature within the 3D printing chamber. A combination of treating with sandpaper (performed by the author) and lathing (performed by David Carter at the University of Michigan LSA

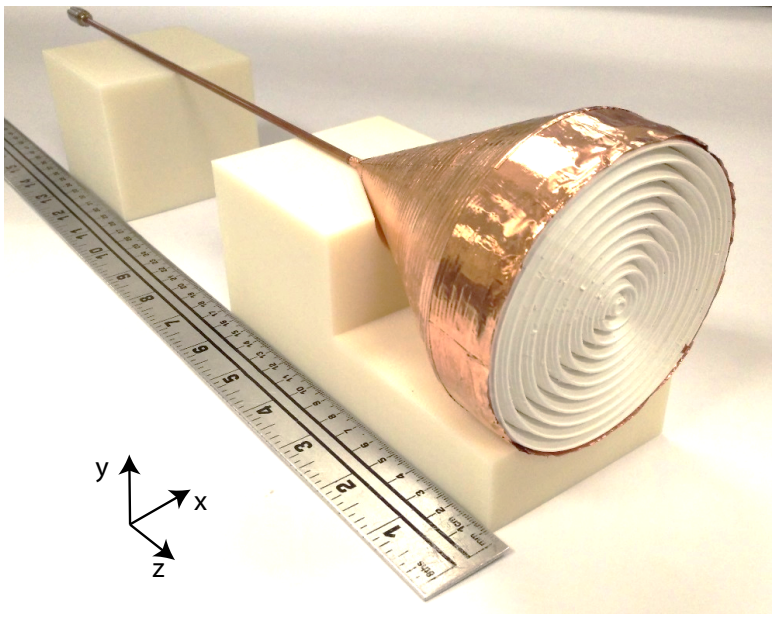

Figure 4.16: Fabricated prototype of the metamaterial implementation of the radiator, obtained through 3D printing.

Instrument Shop) on the affected surfaces was necessary to flatten the parts so that they would be flushed against each other upon assembly.

- Great care was taken to minimize the air gaps between the parts. However, due to the tight fit between some of the parts and the hardness of the material, some air gaps between parts could not be avoided.

- Inserting the electrically small monopole into the 3D printed region completely vertically was also challenging.

The longitudinal ($\widehat{z}'$-directed) electric field was measured in the region over the radiator (1601 points between 5 and 15 GHz). An electrically-small monopole surrounded by absorber was used as a probe, attached to a 3D translation stage. An open-ended coaxial cable made of RG402 (inner radius of 0.455 mm, outer radius of 1.485 mm). Both the radiator and the probe were connected to a vector network analyzer that was used to measure the signal transmitted between the two. A picture of the measurement setup is shown in Fig. 4.17.

The normalized fields along the $(\widehat{x}' - \widehat{z}')$ plane, obtained through COMSOL simulations, are shown at 7.5, 10, and 12.5 GHz in Fig. 4.18(a), (d), and (g), respectively. The experimentally measured fields along this plane at the same three frequencies are shown in Fig. 4.18(b), (e), and (h). The measurement results agree well with those from simulation.

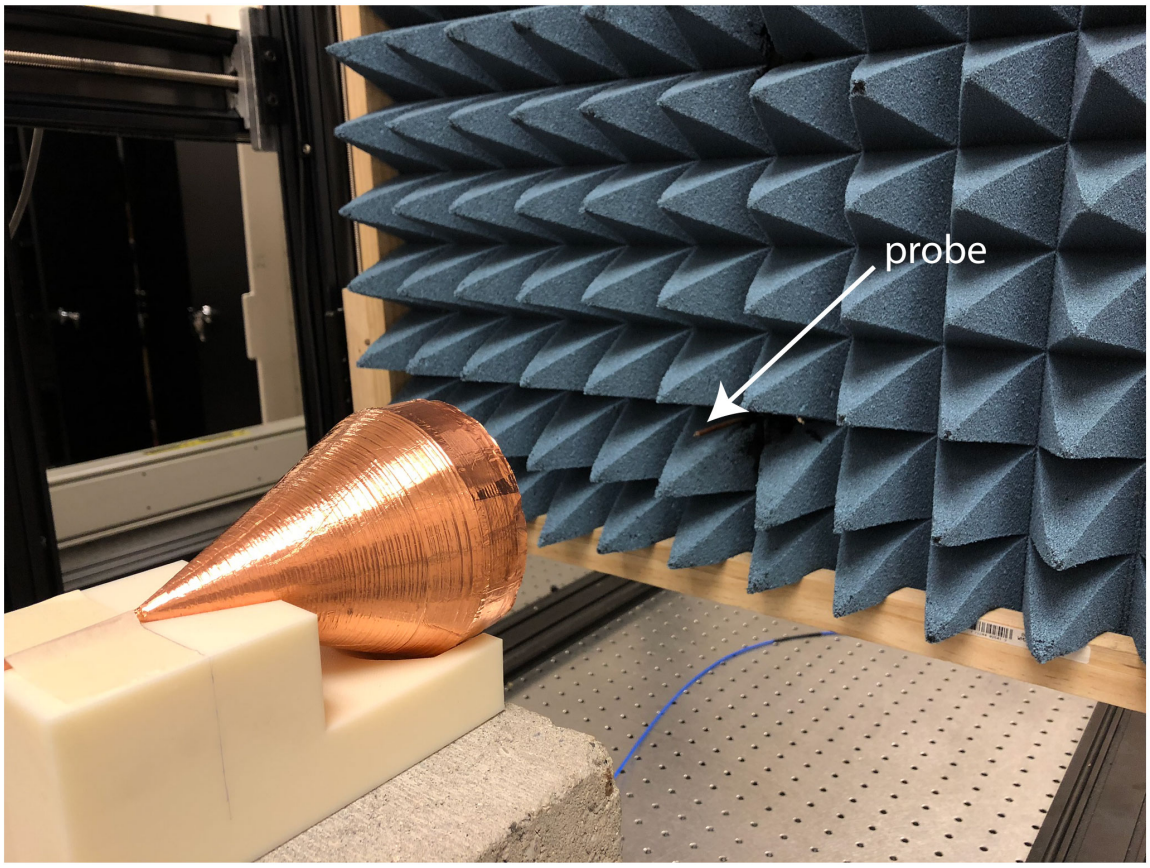

Figure 4.17: Measurement setup used to scan the $\widehat{z}'$-directed electric field emitted by the radiator.

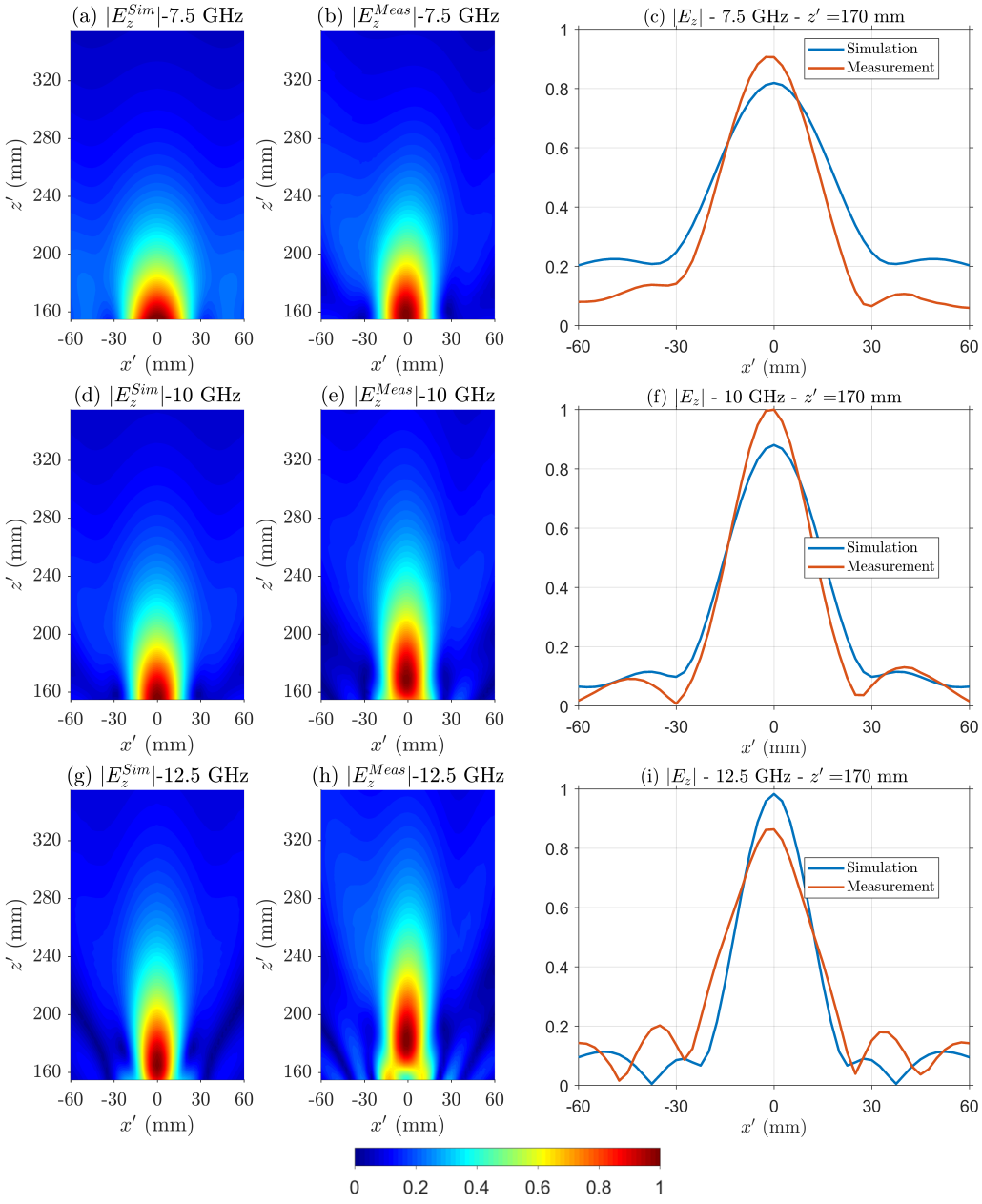

Figure 4.18: The longitudinal ($\widehat{z}'$-directed) electric field in the region over the radiator: (a) simulation and (b) measurement results at 7.5 GHz, (c) simulation and measurement results at 7.5 GHz at $z' = 170$ mm, (d) simulation and (e) measurement results at 10 GHz, (f) simulation and measurement results at 10 GHz at $z' = 170$ mm, (g) simulation and (h) measurement results at 12.5 GHz, (i) simulation and measurement results at 12.5 GHz at $z' = 170$ mm.

Small discrepancies start to appear at higher frequencies, where the unintenional features of the 3D printing process outlined earlier begin to degrade the radiator's performance. Fig. 4.18(c), (f), and (i) present the simulated and measured fields along the $z' = 170$ mm at those three frequencies for ease of comparison.

The input reflection coefficient of the fabricated prototype is shown in Fig. 4.9 in yellow. The discrepancy between the measured reflection coefficient and the one expected from simulation is attributed to the assembly process of the prototype. Significant effort was placed in minimizing the air gaps between parts, which can cause reflections. However, it was not possible to completely eliminate them.

4.5 Generation of X waves

X waves are pulses consisting of a spectrum of monochromatic Bessel beams exhibiting the same cone angle, θ. Assuming a uniform spectrum, the waveform (longitudinal electric field in this case) of an ideal X wave is given as a function of time, t, and cylindrical coordinates, (ρ, z), by [13]

$$e_z(\rho, z, t) = \int_{\omega_{min}}^{\omega_{max}} J_0(\omega \sin\theta \rho / c_0) e^{j\omega(t - \cos\theta z / c_0)} d\omega, \tag{4.8}$$

where J_0 is the zeroth order Bessel function of the first kind, ω is the angular frequency, and c_0 is the speed of light.

The time domain response of the radiator to a uniform spectrum pulse can be calculated as

$$e_z(x', z', t) = \sum_{\omega_i = 2\pi 7.5\text{GHz}}^{2\pi 12.5\text{GHz}} E_z(x', z', \omega_i) e^{j\omega_i t}, \tag{4.9}$$

where $E_z(x', z', \omega_i)$ is the simulated or measured value of E_z, which depends on spatial coordinates and frequency. The longitudinal electric field produced by the radiator, E_z, is that of an apodized Bessel beam.

Fig. 4.19(a), (c), (e), and (g) present the intensity of the X wave produced by the radiator in simulation. Fig. 4.19(b), (d), (f), and (h) present the intensity of the measured X wave produced by the radiator. Each plot has been normalized between 0 and 1 for ease of comparison. Close agreement is observed between the X wave based on simulation data and the one based on measured data. The measured X wave exhibits more prominent secondary lobes and tail. However, the shapes of the two pulses largely agree with each other.

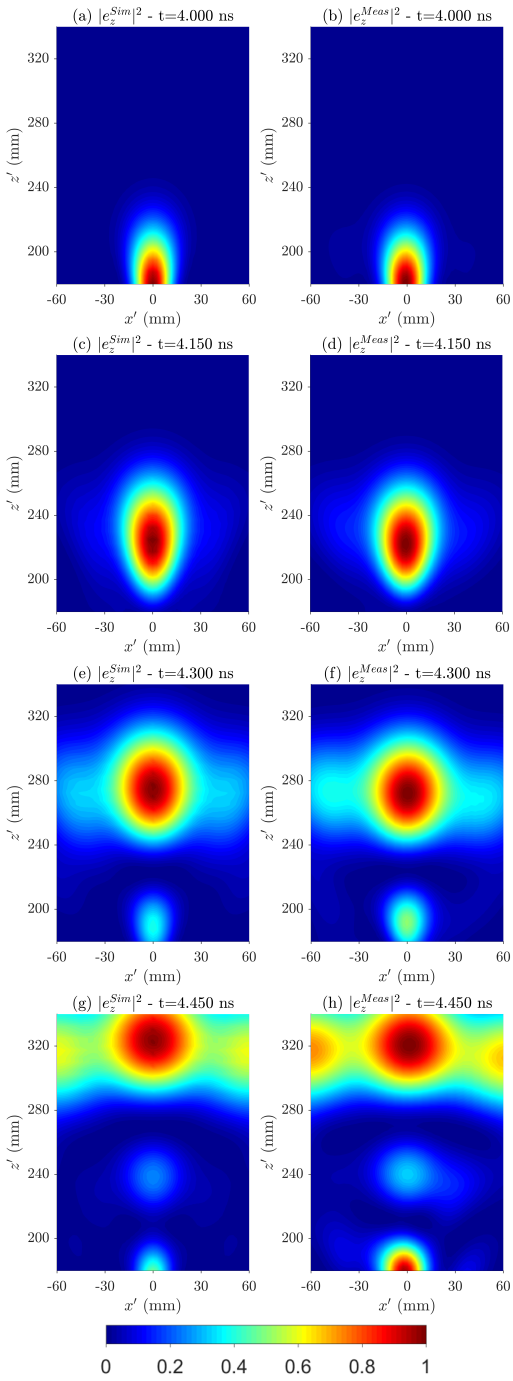

Figure 4.19: The intensity of the longitudinal ($\hat{z}'$-directed) electric field in the region over the radiator as a function of space and time when excited with a uniform spectrum pulse ($7.5 - 12.5$ GHz): using (a) simulation and (b) measurement results at 4 ns, (c) simulation and (d) measurement results at 4.15 ns, (e) simulation and (f) measurement results at 4.3 ns, (g) simulation and (h) measurement results at 4.45 ns.

4.6 Chapter Summary

In this chapter, a paraxial X wave radiator was presented. It was first shown through simulation that the permittivity profile of the transformation region, based on QCTO, and the IML can generate paraxial Bessel beams over a broad bandwidth. This profile was realized using rotationally symmetric metamaterial unit cells. A prototype of the implemented design was fabricated through 3D printing by Dr. Shiyu Zhang at Loughborough University, using three low-loss filaments. The device was printed in parts, which were later combined to form the radiator. The experimental results from this prototype were found to be in good agreement with those expected from simulation. Based on these results, the device's ability to generate paraxial X waves in its radiative near field was demonstrated. A uniform spectrum pulse between 7.5 and 12.5 GHz was used as the excitation.

The progress reported here, combined with other recent advancements in the field of X waves, pave the way for many exciting applications. From imaging to communications, and from heating to high power electromagnetic pulses, X waves are prime candidates for any application that requires highly localized mircrowave pulses.

Finally, 3D printing has already been established as a manufacturing technique for lenses over the past decade. This work demonstrates how 3D printing can also be employed to fabricate interesting near field devices that are directly fed. The incorporation of the feed in the printed part contributes to the reduction of the size of the device. Future advancements in the selection of available filament materials and in the capabilities of 3D printers will solidify the ubiquitousness of 3D printing in electromagnetic design.

CHAPTER 5

Metasurfaces

In the two previous chapters, the work on two novel radiators that generate highly localized waves and pulses was presented. The two designs, based on refractive optics and metamaterials, manipulated the fields of a coaxially fed monopole and converted them into TM Bessel beams in the radiative near field.

In this chapter, we investigate metasurfaces, which manipulate plane waves that exist in the far field. Metasurfaces offer great control over the amplitude, phase, and polarization of propagating waves.

5.1 Chapter Introduction and Outline

Metasurfaces are subwavelength-textured surfaces that exhibit tailored electromagnetic properties. In recent years, they have found numerous applications in flat quasi-optical/optical devices [39, 40], holography [41, 42], plasmonics [43], biosensing [44], THz technology [45], cloaking [46], phase and polarization control [52, 47, 48], antennas [49, 50], and absorbers [51]. Metasurfaces can consist of a single sheet of polarizable particles, such as a patterned metallic cladding, or a cascade of such sheets. Cascaded anisotropic, metallic claddings have been recently used to implement metasurfaces with tailored electric, magnetic, and bianisotropic responses [52].

The present work focuses on the analysis of patterned metallic claddings consisting of a periodic, two dimensional array of subwavelength unit cells. In particular, the unit cells are characterized by an equivalent electric sheet impedance, which can be scalar, anisotropic, or full tensorial. The design of metallic claddings can be traced back to the mature field of frequency selective surfaces [98]. However, only a limited range of geometries, exhibiting scalar or anisotropic sheet impedances, has been analytically modeled to date. These have included rectangular arrays of strips or patches [99], grids of crossed dipoles [100] or Jerusalem crosses [101], and arrays of circular patches [102]. When full tensorial sheet

impedances are required, researchers rely on databases of simulated geometries [42] or optimization schemes [48] for the appropriate unit cell. This is a time-consuming, resource intensive process that can be alleviated by the analytical modeling of some general-purpose geometries.

The proposed analytical models provide expressions for the sheet impedance of unit cells as a function of their physical parameters, frequency, angle of incidence, and polarization of the impinging wave. Inversion of these expressions allows one to find the geometrical parameters needed to realize a specific sheet impedance, under particular incidence angles. Slight tuning of these parameters with a full-wave electromagnetic simulator allows the exact sheet impedance to be synthesized. Moreover, analytical models provide intuition on how a geometry should be modified in order to produce a specific change in its sheet impedance.

The present chapter analytically characterizes general-purpose geometries that exhibit full tensorial sheet impedances under arbitrary plane-wave incidence. Due to the subwavelength size of the unit cells considered, their sheet impedance is given by simple expressions. Sheets consisting of periodic grids of strips are analyzed first. Under normal incidence, their equivalent sheet impedance can be calculated using circuit analysis, where the strips are treated as lumped components. However, under oblique incidence, the sheet impedance calculation requires a field solution. A Method of Moments (MoM) derivation serves as the starting point. Explicit expressions for the sheet impedance are derived in the long wavelength regime from the MoM formulation. The employed technique is demonstrated for two unit cell topologies: a skewed unit cell where two strips intersect at an arbitrary angle (Fig. 5.1(b)), and a three-branch unit cell where three strips intersect at specified angles (Fig. 5.4(b)). Variations of these cell topologies are also examined. Two metasurfaces that control the polarization of incident waves are designed to demonstrate the usefulness of the developed models: an asymmetric linear polrizer at oblique incidence, and a polarization rotator for normally incident plane waves, both operating at 10 GHz.

This chapter is organized as follows. In Sec. 5.2, the sheet impedance of a skewed grid of strips (Fig. 5.1(b)) for normal incidence is calculated using circuit analysis. In Sec. 5.3, a field solution is employed to determine the sheet impedance of the same geometry under oblique incidence. In Sec. 5.4, the sheet impedance of a three-branch unit cell (Fig. 5.4(b)) under normal incidence is determined via circuit analysis. In Sec. 5.5, the sheet impedance of the three-branch unit cell under oblique incidence is derived. In Sec. 5.6, an interpolation procedure is employed to model the sheet impedance of a sliced rectangle unit cell (Fig. 5.6(a)). In Sec. 5.7, the analytical results for the examined unit cells are compared to

full-wave simulation results obtained with a commercial electromagnetic solver. Sec. 5.8 presents the design of a metasurface operating as an asymmetric linear polarizer under oblique incidence at 10 GHz. Sec. 5.9 presents the design of a metasurface operating as a polarization rotator under normal incidence at 10 GHz. Finally, Sec. 5.10 summarizes the findings.

5.2 Skewed Unit Cell under Normal Incidence

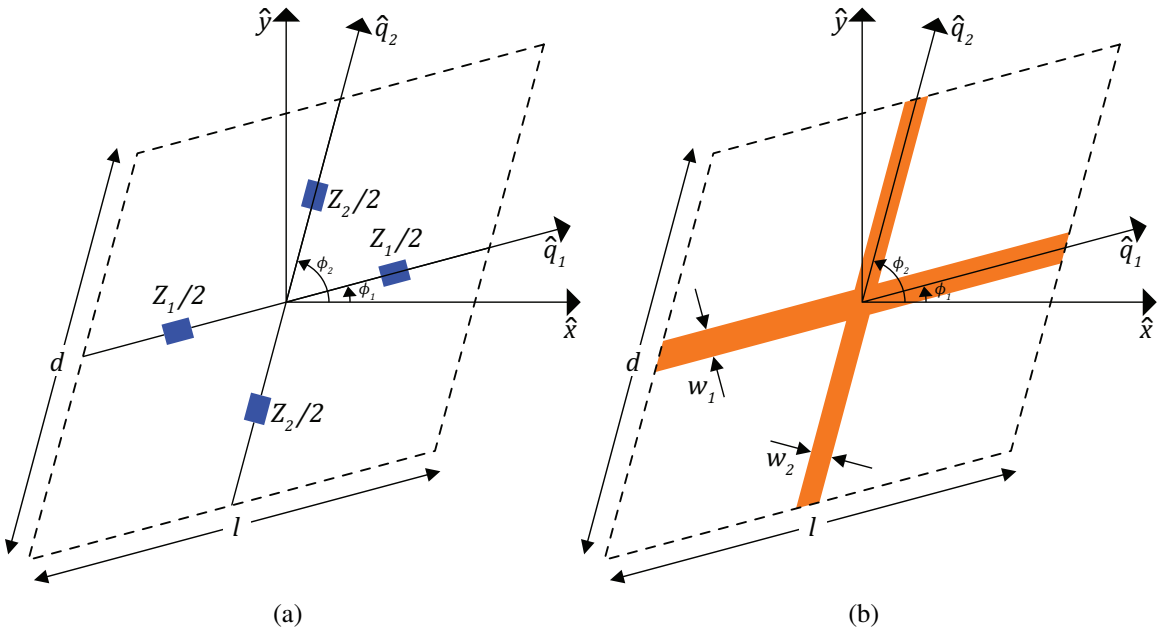

Figure 5.1: Skewed unit cells comprising (a) lumped components (colored blue), and (b) PEC strips (colored orange)

Unit cells with non-orthogonal (skewed) axes can exhibit full tensorial sheet impedances. Rotated orthogonal unit cells can be considered as a subset of skewed unit cells. Skewed unit cells have recently received attention for their ability to produce off-diagonal elements in the effective permeability tensor of transmission-line metamaterials. As a result, they have been used to realize transformation electromagnetics devices [103, 104]. A skewed, crossed wire mesh has also been utilized to implement a metamaterial lens exhibiting negative refraction [105]. Earlier work has examined the scattering properties of skewed grids of wires under arbitrary incidence [106]. Although the results derived therein are accurate,

the employed method is complex and cannot be readily applied to more complicated geometries, such as the three-branch unit cell, shown in Fig. 5.4(b). Here, a simpler method is used to analyze a variety of general-purpose geometries.

To begin, consider the skewed unit cell shown in Fig. 5.1(a). It consists of two branches in arbitrary, in-plane directions (denoted by unit vectors $\widehat{q}_1$ and $\widehat{q}_2$), loaded with lumped impedances Z_1 and Z_2, and having lengths l and d. In the figure, dashed lines denote the boundaries of the unit cell. Perfect short connections are assumed between the nodes of the circuit. In addition, a time dependence of the form $e^{-j\omega t}$ is assumed throughout the chapter. The spatially averaged electric fields, E_{q1} and E_{q2}, along $\widehat{q}_1$ and $\widehat{q}_2$ are related to the spatially averaged electric fields, E_x and E_y, along $\widehat{x}$ and $\widehat{y}$ as

$$\begin{bmatrix} E_{q1} \\ E_{q2} \end{bmatrix} = \overline{\overline{A}} \begin{bmatrix} E_x \\ E_y \end{bmatrix}, \quad \overline{\overline{A}} = \begin{bmatrix} \cos\phi_1 & \sin\phi_1 \\ \cos\phi_2 & \sin\phi_2 \end{bmatrix} \tag{5.1}$$

where ϕ_1 is the angle between $\widehat{q}_1$ and $\widehat{x}$, and ϕ_2 is the angle between $\widehat{q}_2$ and $\widehat{x}$. The electric fields can be expressed in terms of the currents, I_{q1} and I_{q2}, flowing through Z_1 and Z_2. The currents can also be spatially averaged to find the corresponding surface current densities, J_{q1} and J_{q2},

$$\begin{bmatrix} E_{q1} \\ E_{q2} \end{bmatrix} = \begin{bmatrix} \frac{Z_1}{l} & 0 \\ 0 & \frac{Z_2}{d} \end{bmatrix} \begin{bmatrix} I_{q1} \\ I_{q2} \end{bmatrix} = \begin{bmatrix} Z_1 \frac{d'}{l} & 0 \\ 0 & Z_2 \frac{l'}{d} \end{bmatrix} \begin{bmatrix} J_{q1} \\ J_{q2} \end{bmatrix} \tag{5.2}$$

where $d' = d\sin\Delta\phi$ and $l' = l\sin\Delta\phi$ are the distances between adjacent $\widehat{q}_1$- and $\widehat{q}_2$-directed branches, respectively, and $\Delta\phi = \phi_2 - \phi_1$. Surface current densities J_{q1} and J_{q2} are related to the total surface current densities, $J_{t,x}$ and $J_{t,y}$, along $\widehat{x}$ and $\widehat{y}$ as follows

$$\begin{bmatrix} J_{t,x} \\ J_{t,y} \end{bmatrix} = \overline{\overline{A}}^{\mathrm{T}} \begin{bmatrix} J_{q1} \\ J_{q2} \end{bmatrix} \tag{5.3}$$

The sheet impedance tensor, $\overline{\overline{\eta}}$, relates the average electric field tangential to a sheet, $\vec{E}_{tan}$, to the surface current density, $\vec{J}$. For a sheet in the $(x-y)$-plane, it is defined as

$$\vec{E}_{tan} = \overline{\overline{\eta}}\vec{J} \Rightarrow \begin{bmatrix} E_x \\ E_y \end{bmatrix} = \overline{\overline{\eta}} \begin{bmatrix} J_{t,x} \\ J_{t,y} \end{bmatrix} = \begin{bmatrix} \eta_{xx} & \eta_{xy} \\ \eta_{yx} & \eta_{yy} \end{bmatrix} \begin{bmatrix} J_{t,x} \\ J_{t,y} \end{bmatrix} \tag{5.4}$$

Using (5.1)-(5.4), the sheet impedance of a skewed unit cell comprising lumped compo-

nents (Fig. 5.1(a)) is

$$\boxed{\overline{\overline{\eta}}_{\text{skewed lumped}} = \overline{\overline{A}}^{-1} \begin{bmatrix} Z_1 \frac{d'}{l} & 0 \\ 0 & Z_2 \frac{l'}{d} \end{bmatrix} \left(\overline{\overline{A}}^{\mathrm{T}}\right)^{-1}} \tag{5.5}$$

which yields a full tensor when at least one of the unit vectors $\widehat{q}_1$ and $\widehat{q}_2$ is not aligned with $\widehat{x}$ or $\widehat{y}$.

Similarly, the sheet impedance of a skewed grid of PEC strips (Fig. 5.1(b)) can be calculated under normal incidence, i.e. when the tangential wave vector, $\vec{k}_{tan} = k_x\widehat{x} + k_y\widehat{y}$, is zero. The grid consists of strips having widths w_1 and w_2 along $\widehat{q}_1$ and $\widehat{q}_2$. It has been shown that the sheet impedance of an infinite grid of parallel PEC strips when illuminated by a normally incident plane-wave polarized along the strips is [107, Eq. (4.58)]

$$\eta_s(b, w) \approx j\frac{\eta_0 k_0 b}{2\pi} \ln\left(\csc\frac{\pi w}{2b}\right) \tag{5.6}$$

where η_0 and k_0 are the wave impedance and wavenumber of the surrounding medium (free space in this case), and b and w are the separation and width of the strips, respectively. In the above expression, it is assumed that $w \ll b \ll \lambda$, where λ is the wavelength. The sheet impedance of a skewed grid of strips (Fig. 5.1(b)) under normal incidence is calculated using (5.5) with the following substitutions

$$Z_1 \to \eta_s\left(d', w_1\right)\frac{l}{d'}, \quad Z_2 \to \eta_s\left(l', w_2\right)\frac{d}{l'} \tag{5.7}$$

resulting in

$$\begin{aligned} \overline{\overline{\eta}}_{\text{skewed strips}}\left(\vec{k}_{tan} = \vec{0}\right) = \\ = \overline{\overline{A}}^{-1} \begin{bmatrix} \eta_s\left(d', w_1\right) & 0 \\ 0 & \eta_s\left(l', w_2\right) \end{bmatrix} \left(\overline{\overline{A}}^{\mathrm{T}}\right)^{-1} \end{aligned} \tag{5.8}$$

5.3 Skewed Unit Cell under Oblique Incidence

Although the previous method provides accurate sheet impedance values for skewed grids of strips, it is limited to normally incident plane waves. When the wave vector of the impinging wave has a component that is tangential to the grid $\left(\vec{k}_{tan} \neq \vec{0}\right)$, currents I_{q1} and I_{q2} are spatially dispersive. Progressively phased currents flowing on the strips, due to an obliquely incident plane wave, produce electric fields that are both along and normal to the strips [108, Eq. (48)], causing strips to interact. Hence, the expressions for electric field

given by (5.2) do not hold in the case of oblique incidence. They neglect the electric fields normal to the strips.

To calculate the impedance of skewed grids under oblique incidence, an electromagnetic field analysis is required. Similar to [109], where orthogonal grids of wires were studied, an MoM formulation is employed here to determine the currents on a skewed grid of wires that is illuminated by a plane wave. For simplicity, wires are studied in lieu of strips. Subsequently, a well-known equivalence will be used to extend the results to grids of strips [107]. Assuming thin wires of radii r_1 and r_2 along $\widehat{q}_1$ and $\widehat{q}_2$ (see Fig. 5.1(b)), the currents on the wires are expressed as infinite sets of spatial harmonics with complex amplitudes A_m and B_u

$$\begin{aligned} I_{q1,u}(q_1) &= \sum_m A_m e^{j(k_{1,m}q_1 + k_1' u d')},\ k_{1,m} = k_1 + \frac{2\pi m}{l} \\ I_{q2,m}(q_2) &= \sum_u B_u e^{j(k_{2,u}q_2 + k_2' m l')},\ k_{2,u} = k_2 + \frac{2\pi u}{d} \end{aligned} \tag{5.9}$$

The integer indices u and m in I_{q1} and I_{q2} above identify a $\widehat{q}_1$- or $\widehat{q}_2$-directed wire, respectively. For example, $\widehat{q}_1$-directed wires cross the $\widehat{y}$-axis at $y_u = ud'/\cos\phi_1$, and $\widehat{q}_2$-directed wires cross the $\widehat{x}$-axis at $x_m = ml'/\sin\phi_2$. Wavenumbers k_1 and k_2 are the scalar projections of the wave vector onto $\widehat{q}_1$ and $\widehat{q}_2$. Wavenumbers k_1' and k_2' are the scalar projections of the wave vector on unit vectors that are perpendicular to $\widehat{q}_1$ and $\widehat{q}_2$. These wavenumbers are expressed in terms of the Cartesian components of the wave vector $\vec{k} = k_x\widehat{x} + k_y\widehat{y} + k_z\widehat{z}$ as

$$\begin{aligned} k_1 &= k_x\cos\phi_1 + k_y\sin\phi_1, \quad & k_1' &= -k_x\sin\phi_1 + k_y\cos\phi_1 \\ k_2 &= k_x\cos\phi_2 + k_y\sin\phi_2, \quad & k_2' &= k_x\sin\phi_2 - k_y\cos\phi_2 \end{aligned} \tag{5.10}$$

In order to derive the MoM equations for a skewed grid of wires, the following procedure is used:

- The total magnetic vector potential due to all $\widehat{q}_1$- and $\widehat{q}_2$-directed currents is calculated. The potential is then expressed in terms of the spectral representation of the 2D-periodic Green's function.
- The scattered electric field associated with the total vector potential is computed.
- The sum of the scattered and incident tangential electric fields is set to zero along a line on the surface of the $\widehat{q}_1$- and $\widehat{q}_2$-directed wires, yielding two equations that involve all complex amplitudes A_m and B_u.

- The two equations are then multiplied by a complex exponential testing function, and are integrated within the limits of one unit cell. The orthogonality between harmonics is invoked.

Using this procedure, the MoM equations of (5.12) are derived for a skewed grid of wires:

$$\sum_u \sum_m \left[\left(k_0^2 - k_{2,u}^2\right)\cot\Delta\phi - k_{2,u}\left(2\pi\frac{m}{l'} + k_2'\right)\right]\frac{e^{-r_1\left(\Gamma'_{mu}+jk_z\right)}}{l\,\Gamma'_{mu}}\text{sinc}\left(u\frac{l}{d}\cos\Delta\phi + m - n\right)B_u +$$

$$+\left(k_0^2 - k_{1,n}^2\right)\sum_u \frac{e^{-r_1(\Gamma_{nu}+jk_z)}}{d'\,\Gamma_{nu}}A_n = \frac{2k_0}{j\eta_0}E_{q1}^i\delta_{n0} \tag{5.12a}$$

$$\sum_m \sum_u \left[\left(k_0^2 - k_{1,m}^2\right)\cot\Delta\phi - k_{1,m}\left(2\pi\frac{u}{d'} + k_1'\right)\right]\frac{e^{-r_2(\Gamma_{mu}+jk_z)}}{d\,\Gamma_{mu}}\text{sinc}\left(m\frac{d}{l}\cos\Delta\phi + u - g\right)A_m +$$

$$+\left(k_0^2 - k_{2,g}^2\right)\sum_m \frac{e^{-r_2\left(\Gamma'_{mg}+jk_z\right)}}{l'\,\Gamma'_{mg}}B_g = \frac{2k_0}{j\eta_0}E_{q2}^i\delta_{g0} \tag{5.12b}$$

$$\Gamma_{mu} = \sqrt{k_{1,m}^2 + (2\pi u/d' + k_1')^2 - k_0^2}, \quad \Gamma'_{mu} = \sqrt{k_{2,u}^2 + (2\pi m/l' + k_2')^2 - k_0^2}$$

$$\text{sinc}(x) = \frac{\sin(\pi x)}{\pi x} \tag{5.12c}$$

These expressions can be rewritten in abbreviated form as

$$\sum_u R_{nu}B_u + P_nA_n = E_{q1}^i\delta_{n0} \tag{5.13a}$$

$$\sum_m T_{gm}A_m + S_gB_g = E_{q2}^i\delta_{g0} \tag{5.13b}$$

where

$$
\begin{aligned}
R_{nu} =& \frac{j\eta_0}{2k_0}\sum_m \left[\left(k_0^2-k_{2,u}^2\right)\cot\Delta\phi - k_{2,u}\left(2\pi\frac{m}{l'}+k_2'\right)\right] \\
& \frac{e^{-r_1(\Gamma'_{mu}+jk_z)}}{l\,\Gamma'_{mu}}\text{sinc}\left(u\frac{l}{d}\cos\Delta\phi+m-n\right) \\
P_n =& \frac{j\eta_0}{2k_0}\left(k_0^2-k_{1,n}^2\right)\sum_u \frac{e^{-r_1(\Gamma_{nu}+jk_z)}}{d'\,\Gamma_{nu}} \\
T_{gm} =& \frac{j\eta_0}{2k_0}\sum_u \left[\left(k_0^2-k_{1,m}^2\right)\cot\Delta\phi - k_{1,m}\left(2\pi\frac{u}{d'}+k_1'\right)\right] \\
& \frac{e^{-r_2(\Gamma_{mu}+jk_z)}}{d\,\Gamma_{mu}}\text{sinc}\left(m\frac{d}{l}\cos\Delta\phi+u-g\right) \\
S_g =& \frac{j\eta_0}{2k_0}\left(k_0^2-k_{2,g}^2\right)\sum_m \frac{e^{-r_2\left(\Gamma'_{mg}+jk_z\right)}}{l'\,\Gamma'_{mg}}
\end{aligned}
\tag{5.13c}
$$

In (5.12)-(5.13), δ_{ij} is the Kronecker delta, and E^i_{q1}, E^i_{q2} are the components of the incident electric field along $\widehat{q}_1$, $\widehat{q}_2$. In (5.12a) and (5.13a), each harmonic of I_{q1} is related to all harmonics of I_{q2}. Similarly in (5.12b) and (5.13b), each harmonic of I_{q2} is related to all harmonics of I_{q1}. The incident fields only appear in the equations for the fundamental harmonics ($n = 0$ and $g = 0$). The MoM equations form an infinite set of equations ($n,\, g \in \mathbb{Z}$) which must be truncated in order to be solved numerically.

Solving the system of equations given in (5.12)-(5.13) yields the complex amplitudes of the current harmonics, A_m and B_u. The currents on the wires can then be calculated using (5.9). However, a large number of harmonics is required for the method to converge because currents I_{q1} and I_{q2} are discontinuous at the junctions ($q_1 = q_2 = 0$ in Fig. 5.1(b)). As a result, analytic expressions for the sheet impedance cannot be derived. In order to improve the convergence, sawtooth functions are incorporated into the expressions for I_{q1} and I_{q2} to model this discontinuity at the wire junctions [110]. Let us assume the following sawtooth functions within a unit cell ($|q_1| < l/2$ and $|q_2| < d/2$)

$$
\begin{aligned}
f_1(q_1) &= \Delta\left[u(q_1)-\frac{q_1}{l}-\frac{1}{2}\right] = \Delta{\sum_m}' \frac{e^{j2\pi m q_1/l}}{2\pi j m} \\
f_2(q_2) &= \Delta\left[u(q_2)-\frac{q_2}{d}-\frac{1}{2}\right] = \Delta{\sum_u}' \frac{e^{j2\pi u q_2/d}}{2\pi j u}
\end{aligned}
\tag{5.14}
$$

where $u(x)$ is the unit step function and Δ is the unknown complex amplitude of the sawtooth functions. The prime in the sums denotes that the zeroth terms are excluded from the summations. For clarity, the sawtooth functions $f_1(q_1)$ and $f_2(q_2)$ are plotted

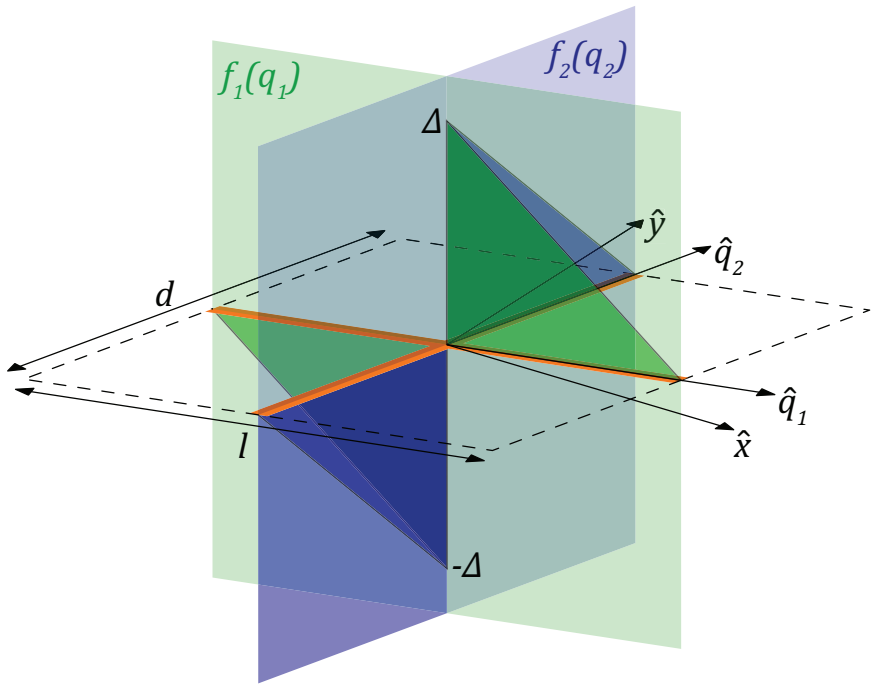

Figure 5.2: Sawtooth functions $f_1(q_1)$ and $f_2(q_2)$ superimposed on the skewed unit cell geometry

on the skewed unit cell geometry in Fig. 5.2. Note that Δ is a complex quantity. This specific discontinuous function was chosen because it has a simple spectral representation, as evidenced by (5.14). As a result, it leads to simple analytical expressions. Moreover, it models well the discontinuity in the currents [110]. Currents I_{q1} and I_{q2} can then be expressed as

$$\begin{aligned} I_{q1,u}(q_1) &= e^{j(k_1 q_1 + k_1' u d')} \left[\sum_m A'_m e^{j2\pi m q_1/l} + f_1(q_1) \right] \\ I_{q2,m}(q_2) &= e^{j(k_2 q_2 + k_2' m l')} \left[\sum_u B'_u e^{j2\pi u q_2/d} - f_2(q_2) \right] \end{aligned} \tag{5.15}$$

where the new complex amplitudes, A'_m and B'_u, are given by

$$A_m = A'_m + \frac{\Delta(1-\delta_{m0})}{2\pi j m}, \quad B_u = B'_u - \frac{\Delta(1-\delta_{u0})}{2\pi j u} \tag{5.16}$$

The jumps in the currents I_{q1} and I_{q2} in (5.15) have opposite signs. This ensures that Kirchhoff's current law is satisfied at the junction. The new MoM equations, exhibiting improved convergence, are found by using (5.16) in (5.13). Since the unknown Δ has been introduced, one more linearly independent equation is required. To ensure that the electric

fields are continuous at the junction, the linear charge densities, λ_q, on the four conductors at the junction ($q_1 = 0^+, 0^-$ and $q_2 = 0^+, 0^-$) must be equal [111, Eq. (5)]

$$\lambda_q(q_1 = 0^+) = \lambda_q(q_1 = 0^-) = \lambda_q(q_2 = 0^+) = \lambda_q(q_2 = 0^-) \tag{5.17}$$

From the conservation of charge, it follows that [110, Eq. (21)]

$$\left.\frac{\partial I_{q1,0}}{\partial q_1}\right|_{q_1=0^+} = \left.\frac{\partial I_{q1,0}}{\partial q_1}\right|_{q_1=0^-} = \left.\frac{\partial I_{q2,0}}{\partial q_2}\right|_{q_2=0^+} = \left.\frac{\partial I_{q2,0}}{\partial q_2}\right|_{q_2=0^-} \tag{5.18}$$

From (5.18), the following condition on the currents can be derived [110, Eq. (26)]

$$\left.\frac{\partial I_{q1,0}}{\partial q_1}\right|_{q_1=0^+} + \left.\frac{\partial I_{q1,0}}{\partial q_1}\right|_{q_1=0^-} = \left.\frac{\partial I_{q2,0}}{\partial q_2}\right|_{q_2=0^+} + \left.\frac{\partial I_{q2,0}}{\partial q_2}\right|_{q_2=0^-} \tag{5.19}$$

By applying this condition to the current expressions given in (5.15), the following additional equation is derived

$$\sum_m k_{1,m} A'_m - \sum_u k_{2,u} B'_u + j\Delta\left(\frac{1}{l} + \frac{1}{d}\right) = 0 \tag{5.20}$$

The new system of equations for A'_m and B'_u, formed by (5.13), (5.16) and (5.20), converges rapidly because the current discontinuity has been taken into account. For subwavelength unit cells, higher order terms ($m, u \neq 0$) will be negligible. Therefore, it is sufficient to retain only the fundamental current harmonics, with complex amplitudes A'_0 and B'_0. In this case, the system reduces to

$$P_0 A'_0 + R_{00} B'_0 + j\Delta {\sum_u}' \frac{R_{0u}}{2\pi u} = E^i_{q1} \tag{5.21a}$$

$$S_0 B'_0 + T_{00} A'_0 - j\Delta {\sum_m}' \frac{T_{0m}}{2\pi m} = E^i_{q2} \tag{5.21b}$$

$$k_1 A'_0 - k_2 B'_0 + j\Delta\left(\frac{1}{l} + \frac{1}{d}\right) = 0 \tag{5.21c}$$

Again, A'_0 and B'_0 are the complex amplitudes of the fundamental harmonics of currents I_{q1} and I_{q2} in (5.15), and Δ represents the jump in the currents at the junction. By solving (5.21c) for Δ, and substituting the result into (5.21a) and (5.21b), the incident electric fields, E^i_{q1} and E^i_{q2}, can be expressed in terms of the surface current densities $J_{q1} = A'_0/d'$

and $J_{q2} = B_0'/l'$

$$\begin{bmatrix} E_{q1}^i \\ E_{q2}^i \end{bmatrix} = \begin{bmatrix} d'P_0 - \frac{d'dlk_1}{d+l} \sum_u{}' \frac{R_{0u}}{2\pi u} & l'R_{00} + \frac{dl'lk_2}{d+l} \sum_u{}' \frac{R_{0u}}{2\pi u} \\ d'T_{00} + \frac{d'dlk_1}{d+l} \sum_m{}' \frac{T_{0m}}{2\pi m} & l'S_0 - \frac{dl'lk_2}{d+l} \sum_m{}' \frac{T_{0m}}{2\pi m} \end{bmatrix} \begin{bmatrix} J_{q1} \\ J_{q2} \end{bmatrix} \tag{5.22}$$

If the wire radii r_1 and r_2 are small compared to the wavelength, the following approximate formula can be used in the calculation of P_0 and S_0 [109, Eq. (10)]

$$\sum_u \frac{e^{-r_1\Gamma_{0u}}}{\Gamma_{0u}} \approx \frac{d'}{\pi} \ln \frac{d'}{2\pi r_1} + \frac{1}{\Gamma_{00}} = \frac{d'}{\pi} \ln \frac{d'}{2\pi r_1} + \frac{1}{jk_z} \tag{5.23}$$

Using (5.13c) and (5.23)

$$\begin{aligned} P_0 &\approx \frac{j\eta_0}{2k_0 d'} \left(k_0^2 - k_1^2\right) \left(\frac{d'}{\pi} \ln \frac{d'}{2\pi r_1} + \frac{1}{jk_z} \right) \\ S_0 &\approx \frac{j\eta_0}{2k_0 l'} \left(k_0^2 - k_2^2\right) \left(\frac{l'}{\pi} \ln \frac{l'}{2\pi r_2} + \frac{1}{jk_z} \right) \end{aligned} \tag{5.24}$$

The sums that appear in (5.22) can be approximated as

$$\begin{aligned} \sum_u{}' \frac{R_{0u}}{2\pi u} &\approx \frac{\eta_0}{j2\pi l} \frac{k_1}{k_0} \ln \frac{d'}{2\pi r_1} \\ \sum_m{}' \frac{T_{0m}}{2\pi m} &\approx \frac{\eta_0}{j2\pi d} \frac{k_2}{k_0} \ln \frac{l'}{2\pi r_2} \end{aligned} \tag{5.25}$$

The scattered electric fields, E_{q1}^s and E_{q2}^s, along $\widehat{q}_1$ and $\widehat{q}_2$ are related to the surface current densities through [109, Eq. (4)]

$$\begin{bmatrix} E_{q1}^s \\ E_{q2}^s \end{bmatrix} = \frac{\eta_0}{2k_z k_0} \begin{bmatrix} k_1^2 - k_0^2 & k_1 k_2 - k_0^2 \cos\Delta\phi \\ k_1 k_2 - k_0^2 \cos\Delta\phi & k_2^2 - k_0^2 \end{bmatrix} \begin{bmatrix} J_{q1} \\ J_{q2} \end{bmatrix} \tag{5.26}$$

The total electric fields, E_{q1} and E_{q2}, along $\widehat{q}_1$ and $\widehat{q}_2$ are the sums of the incident and scattered electric fields

$$\begin{aligned} &\begin{bmatrix} E_{q1} \\ E_{q2} \end{bmatrix} = \begin{bmatrix} E_{q1}^i \\ E_{q2}^i \end{bmatrix} + \begin{bmatrix} E_{q1}^s \\ E_{q2}^s \end{bmatrix} = \\ &= j\frac{\eta_0 k_0}{2\pi} \begin{bmatrix} \left(d' - \frac{d'l}{d+l} \frac{k_1^2}{k_0^2}\right) \ln \frac{d'}{2\pi r_1} & -\frac{d'l}{d+l} \frac{k_1 k_2}{k_0^2} \ln \frac{d'}{2\pi r_1} \\ -\frac{l'd}{d+l} \frac{k_1 k_2}{k_0^2} \ln \frac{l'}{2\pi r_2} & \left(l' - \frac{l'd}{d+l} \frac{k_2^2}{k_0^2}\right) \ln \frac{l'}{2\pi r_2} \end{bmatrix} \begin{bmatrix} J_{q1} \\ J_{q2} \end{bmatrix} \end{aligned} \tag{5.27}$$

Using (5.5), the sheet impedance of a skewed grid of wires can then be found. The result can be extended to a skewed grid of strips having widths w_1 and w_2 (Fig. 5.1(b)) by invoking the following well-known substitution [107, Eq. (4.56)]

$$r_1 \to \frac{d'}{2\pi}\sin\frac{\pi w_1}{2d'}, \quad r_2 \to \frac{l'}{2\pi}\sin\frac{\pi w_2}{2l'} \tag{5.28}$$

Under oblique incidence, the sheet impedance of a skewed grid of strips possessing sub-wavelength periodicity becomes

$$\boxed{\begin{aligned}&\overline{\overline{\eta}}_{\text{skewed strips}}\left(\vec{k}_{tan}\right) = \\ &\overline{\overline{A}}^{-1}\begin{bmatrix}\eta_1\left(1-\frac{l}{d+l}\frac{k_1^2}{k_0^2}\right) & -\eta_1\frac{l}{d+l}\frac{k_1k_2}{k_0^2}\\ -\eta_2\frac{d}{d+l}\frac{k_1k_2}{k_0^2} & \eta_2\left(1-\frac{d}{d+l}\frac{k_2^2}{k_0^2}\right)\end{bmatrix}\left(\overline{\overline{A}}^{\mathrm{T}}\right)^{-1}\\ &\eta_1 = j\frac{\eta_0 k_0 d'}{2\pi}\ln\left(\csc\frac{\pi w_1}{2d'}\right),\ \eta_2 = j\frac{\eta_0 k_0 l'}{2\pi}\ln\left(\csc\frac{\pi w_2}{2l'}\right)\end{aligned}} \tag{5.29}$$

The loaded, skewed unit cell (shown in Fig. 5.3(a)) can be considered as the series connection of the unloaded, skewed unit cell (Fig. 5.1(b)) and lumped components Z_1 and Z_2 (Fig. 5.1(a)). As a result, its sheet impedance under oblique incidence is

$$\boxed{\begin{aligned}&\overline{\overline{\eta}}_{\text{loaded, skewed strips}}\left(\vec{k}_{tan}\right) = \\ &\qquad\overline{\overline{\eta}}_{\text{skewed strips}}\left(\vec{k}_{tan}\right) + \overline{\overline{\eta}}_{\text{skewed lumped}}\end{aligned}} \tag{5.30}$$

It should be noted that the loaded, skewed unit cell is capable of exhibiting an arbitrary sheet impedance for a given wave vector.

The skewed patch, shown in Fig. 5.3(b), is complementary to the unloaded, skewed unit cell (Fig. 5.1(b)). As a result, its sheet impedance under oblique incidence, $\overline{\overline{\eta}}_{\text{skewed patch}}\left(\vec{k}_{tan}\right)$, can be found using Babinet's principle in tensorial form [112, Eq. (40)]

$$\boxed{\overline{\overline{\eta}}_{\text{skewed patch}}\left(\vec{k}_{tan}\right) = \frac{\eta_0^2}{4}\left(\overline{\overline{R}}^{\mathrm{T}}\overline{\overline{\eta}}_{\text{skewed strips}}\left(\vec{k}_{tan}\right)\overline{\overline{R}}\right)^{-1}} \tag{5.31}$$

where $\overline{\overline{R}} = \begin{bmatrix}0 & -1\\ 1 & 0\end{bmatrix}$ is the $\pi/2$ rotation matrix.

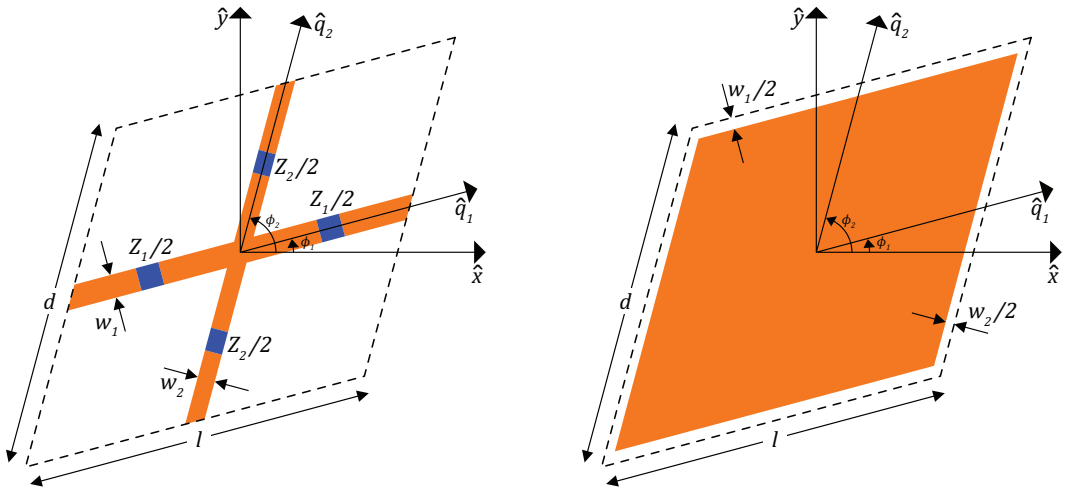

Figure 5.3: (a) A loaded, skewed unit cell comprising PEC strips and lumped components, and (b) a skewed patch

5.4 Three-Branch Unit Cell under Normal Incidence

The loaded, skewed unit cell (Fig. 5.3(a)) may present an arbitrary sheet impedance through control of its physical geometry and lumped components. However, in applications that require inhomogeneous claddings, the physical parameters d, l, ϕ_1, ϕ_2 cannot vary arbitrarily from cell to cell as this creates an "inter-cell connectivity problem" [103, Fig. 9]. The geometrical parameters must be chosen such that the strips of neighboring unit cells remain connected. Although the loading elements, Z_1 and Z_2, may vary between unit cells, they only provide two degrees of freedom, whereas the realization of an arbitrary, reciprocal impedance tensor requires three.

In order to overcome this limitation, the three-branch unit cell of Fig. 5.4(a) is studied. Its topology is inspired by previous work on tensor transmission-line metamaterials [113, Fig. 4]. It consists of three branches: one along $\widehat{x}$ of length l and loaded with impedance Z_x, another along $\widehat{y}$ of length d and loaded with Z_y, and a third branch along $\widehat{q}_3 = \cos\psi\widehat{x} + \sin\psi\widehat{y}$ ($\psi = tan^{-1}(d/l)$) of length $h = \sqrt{d^2 + l^2}$ and loaded with Z_3. Neighboring $\widehat{q}_3$-directed branches are separated by $t = l\sin\psi$. The electric fields, E_x, E_y, and E_{q3}, along $\widehat{x}$, $\widehat{y}$, and $\widehat{q}_3$, satisfy

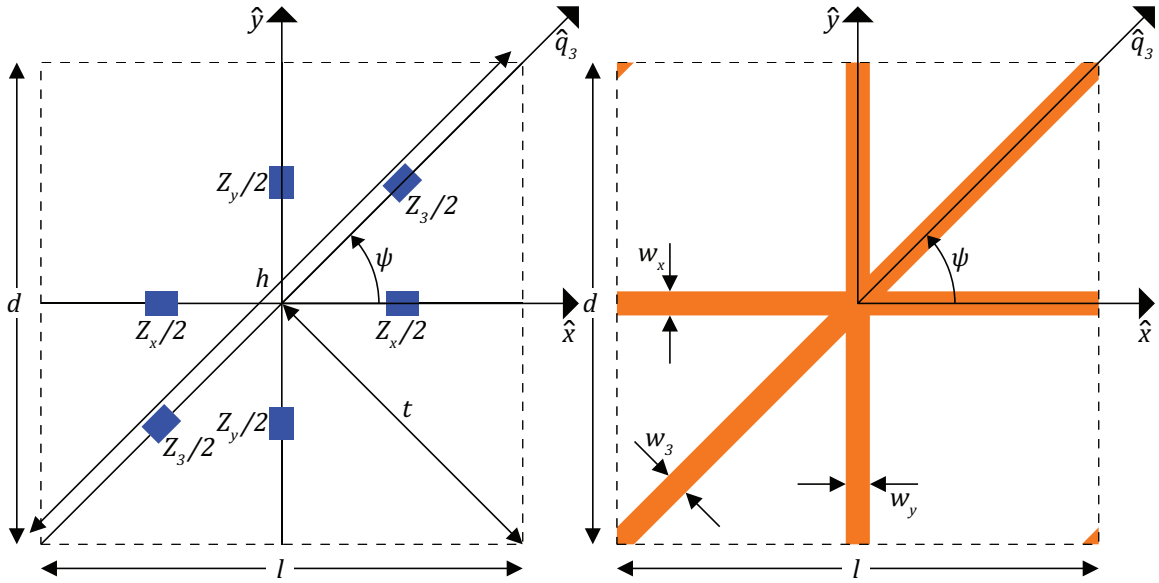

Figure 5.4: Three-branch unit cells comprising (a) lumped components, and (b) PEC strips

$$\begin{bmatrix} E_x \\ E_y \\ E_{q3} \end{bmatrix} = \overline{\overline{B}} \begin{bmatrix} E_x \\ E_y \end{bmatrix}, \quad \overline{\overline{B}} = \begin{bmatrix} 1 & 0 \\ 0 & 1 \\ \cos\psi & \sin\psi \end{bmatrix} \tag{5.32}$$

The electric fields can be expressed in terms of the currents on the three branches, I_x, I_y, and I_{q3}, and the corresponding spatially averaged surface current densities, J_x, J_y, and J_{q3}, as

$$\begin{bmatrix} E_x \\ E_y \\ E_{q3} \end{bmatrix} = \begin{bmatrix} Z_x/l & 0 & 0 \\ 0 & Z_y/d & 0 \\ 0 & 0 & Z_3/h \end{bmatrix} \begin{bmatrix} I_x \\ I_y \\ I_{q3} \end{bmatrix} = \overline{\overline{C}} \begin{bmatrix} J_x \\ J_y \\ J_{q3} \end{bmatrix}$$
$$\overline{\overline{C}} = \begin{bmatrix} dZ_x/l & 0 & 0 \\ 0 & lZ_y/d & 0 \\ 0 & 0 & tZ_3/h \end{bmatrix} \tag{5.33}$$

Both J_x and J_{q3} contribute to the total $\hat{x}$-directed surface current density, $J_{t,x}$. Similarly, both J_y and J_{q3} contribute to the total $\hat{y}$-directed surface current density, $J_{t,y}$. The total

surface current densities can then be expressed as

$$\begin{bmatrix} J_{t,x} \\ J_{t,y} \end{bmatrix} = \overline{\overline{B}}^{\mathrm{T}} \begin{bmatrix} J_x \\ J_y \\ J_{q3} \end{bmatrix} = \overline{\overline{B}}^{\mathrm{T}}\, \overline{\overline{C}}^{-1} \begin{bmatrix} E_x \\ E_y \\ E_{q3} \end{bmatrix} = \overline{\overline{B}}^{\mathrm{T}}\, \overline{\overline{C}}^{-1} \overline{\overline{B}} \begin{bmatrix} E_x \\ E_y \end{bmatrix} \tag{5.34}$$

Consequently, the sheet impedance of a three-branch unit cell of lumped components (Fig. 5.4(a)) is

$$\boxed{\overline{\overline{\eta}}_{\text{3-branch lumped}} = \left(\overline{\overline{B}}^{\mathrm{T}}\, \overline{\overline{C}}^{-1}\, \overline{\overline{B}} \right)^{-1}} \tag{5.35}$$

In Fig. 5.4(b), the lumped components of Fig. 5.4(a) are replaced by PEC strips of widths w_x, w_y, and w_3 along $\widehat{x}$, $\widehat{y}$, and $\widehat{q}_3$. The sheet impedance of this unit cell under normal incidence is given by (5.35) with the following substitutions

$$Z_x \to \eta_s(d, w_x)\frac{l}{d}, \quad Z_y \to \eta_s(l, w_y)\frac{d}{l}, \quad Z_3 \to \eta_s(t, w_3)\frac{h}{t} \tag{5.36}$$

where $\eta_s(b, w)$ is defined in (5.6). This results in

$$\begin{aligned} &\overline{\overline{\eta}}_{\text{3-branch strips}} \left(\vec{k}_{tan} = 0 \right) = \\ &= \left(\overline{\overline{B}}^{\mathrm{T}} \begin{bmatrix} \eta_s(d, w_x) & 0 & 0 \\ 0 & \eta_s(l, w_y) & 0 \\ 0 & 0 & \eta_s(t, w_3) \end{bmatrix}^{-1} \overline{\overline{B}} \right)^{-1} \end{aligned} \tag{5.37}$$

5.5 Three-Branch Unit Cell under Oblique Incidence

The calculation of the sheet impedance of the three-branch unit cell under oblique incidence again requires an electromagnetic field solution. The method presented in Sec. 5.3 is applied to the case of three intersecting wires placed in the three-branch geometry (Fig. 5.4(b)). The radii along $\widehat{x}$, $\widehat{y}$, and $\widehat{q}_3$ are r_x, r_y, and r_3. The currents on the wires are expressed as infinite sets of spatial harmonics with complex amplitudes A_s, B_s, and C_s

$$\begin{aligned} I_{x,u}(x) &= \sum_s A_s e^{j(k_{x,s}x + k_y ud)},\ k_{x,s} = k_x + \frac{2\pi s}{l} \\ I_{y,u}(y) &= \sum_s B_s e^{j(k_{y,s}y + k_x ul)},\ k_{y,s} = k_y + \frac{2\pi s}{d} \\ I_{q3,u}(q_3) &= \sum_s C_s e^{j(k_{3,s}q_3 + k'_3 ut)},\ k_{3,s} = k_3 + \frac{2\pi s}{h} \end{aligned} \tag{5.38}$$

where wavenumbers $k_3 = k_x\cos\psi + k_y\sin\psi$ and $k_3' = k_x\sin\psi - k_y\cos\psi$ are the scalar projections of the wave vector onto $\widehat{q}_3$ and a unit vector perpendicular to $\widehat{q}_3$, respectively. The integer index u is used to identify a specific wire in each of the three directions. The derived MoM equations for this geometry are

$$\begin{aligned} D_n^{\mathrm{I}} A_n - \sum_u D_{nu}^{\mathrm{II}} B_u + \sum_s D_{ns}^{\mathrm{III}} C_s &= E_x^i \delta_{n0} \\ D_g^{\mathrm{IV}} B_g - \sum_s D_{gs}^{\mathrm{V}} A_s + \sum_u D_{gu}^{\mathrm{VI}} C_u &= E_y^i \delta_{g0} \\ D_b^{\mathrm{VII}} C_b + \sum_s D_{bs}^{\mathrm{VIII}} A_s + \sum_u D_{bu}^{\mathrm{IX}} B_u &= E_{q3}^i \delta_{b0} \end{aligned} \tag{5.39}$$

where the D quantities are given in Appendix D and E_x^i, E_y^i, E_{q3}^i are the incident electric fields at the plane of the grid along $\widehat{x}$, $\widehat{y}$, $\widehat{q}_3$. As before, the convergence is significantly improved by incorporating the following sawtooth functions

$$\begin{aligned} f_x(x) &= \Upsilon \left[u(x) - \frac{x}{l} - \frac{1}{2} \right], |x| < \frac{l}{2} \\ f_y(y) &= \Lambda \left[u(y) - \frac{y}{d} - \frac{1}{2} \right], |y| < \frac{d}{2} \\ f_3(q_3) &= -(\Upsilon + \Lambda) \left[u(q_3) - \frac{q_3}{h} - \frac{1}{2} \right], |q_3| < \frac{h}{2} \end{aligned} \tag{5.40}$$

into the expressions for the currents in (5.38), where Υ and Λ are the two unknown complex amplitudes of the sawtooth functions. The currents can then be expressed as

$$\begin{aligned} I_{x,u}(x) &= e^{j(k_x x + k_y u d)} \left[\sum_s A_s' e^{j2\pi s x/l} + f_x(x) \right] \\ I_{y,u}(y) &= e^{j(k_y y + k_x u l)} \left[\sum_s B_s' e^{j2\pi s y/d} + f_y(y) \right] \\ I_{q3,u}(q_3) &= e^{j(k_3 q_3 + k_3' u t)} \left[\sum_s C_s' e^{j2\pi s q_3/h} + f_3(q_3) \right] \end{aligned} \tag{5.41}$$

where the new complex amplitudes, A_s', B_s', and C_s', are given by

$$\begin{aligned} A_s &= A_s' + \frac{\Upsilon(1-\delta_{s0})}{2\pi j s}, \quad B_s = B_s' + \frac{\Lambda(1-\delta_{s0})}{2\pi j s}, \\ C_s &= C_s' - \frac{(\Upsilon + \Lambda)(1-\delta_{s0})}{2\pi j s} \end{aligned} \tag{5.42}$$

The first three MoM equations of the new set that exhibits improved convergence are found by substituting (5.42) into (5.39). Two extra equations are needed, due to the introduction of the two unknowns Υ and Λ. They are derived from the continuity of charge at the junction

$$\begin{aligned}
\left.\frac{\partial I_{x,0}}{\partial x}\right|_{x=0^+} + \left.\frac{\partial I_{x,0}}{\partial x}\right|_{x=0^-} &= \left.\frac{\partial I_{y,0}}{\partial y}\right|_{y=0^+} + \left.\frac{\partial I_{y,0}}{\partial y}\right|_{y=0^-} \\
\left.\frac{\partial I_{x,0}}{\partial x}\right|_{x=0^+} + \left.\frac{\partial I_{x,0}}{\partial x}\right|_{x=0^-} &= \left.\frac{\partial I_{q3,0}}{\partial q_3}\right|_{q_3=0^+} + \left.\frac{\partial I_{q3,0}}{\partial q_3}\right|_{q_3=0^-}
\end{aligned} \tag{5.43}$$

which results in

$$\begin{aligned}
j\sum_s k_{x,s}A'_s - j\sum_s k_{y,s}B'_s - \frac{\Upsilon}{l} + \frac{\Lambda}{d} &= 0 \\
j\sum_s k_{x,s}A'_s - j\sum_s k_{3,s}C'_s - \Upsilon\left(\frac{1}{l}+\frac{1}{h}\right) - \frac{\Lambda}{h} &= 0
\end{aligned} \tag{5.44}$$

The new set of equations for A'_s, B'_s and C'_s, formed by (5.39), (5.42) and (5.44), converges rapidly and a single current harmonic is sufficient to model subwavelength grids. The incident electric fields can then be expressed in terms of the average surface current densities $J_x = A'_0/d$, $J_y = B'_0/l$, $J_{q3} = C'_0/t$ by eliminating Υ and Λ in the following equations

$$\begin{aligned}
D_0^{\mathrm{I}}A'_0 - D_{00}^{\mathrm{II}}B'_0 + D_{00}^{\mathrm{III}}C'_0 + \\
+j(\Upsilon+\Lambda)\sum_s{}' \frac{D_{0s}^{\mathrm{III}}}{2\pi s} + j\Lambda\sum_u{}' \frac{D_{0u}^{\mathrm{II}}}{2\pi u} &= E_x^i \\
D_0^{\mathrm{IV}}B'_0 - D_{00}^{\mathrm{V}}A'_0 + D_{00}^{\mathrm{VI}}C'_0 + \\
+j(\Upsilon+\Lambda)\sum_u{}' \frac{D_{0u}^{\mathrm{VI}}}{2\pi u} + j\Upsilon\sum_s{}' \frac{D_{0s}^{\mathrm{V}}}{2\pi s} &= E_y^i \\
D_0^{\mathrm{VII}}C'_0 + D_{00}^{\mathrm{VIII}}A'_0 + D_{00}^{\mathrm{IX}}B'_0 - \\
-j\Upsilon\sum_s{}' \frac{D_{0s}^{\mathrm{VIII}}}{2\pi s} - j\Lambda\sum_u{}' \frac{D_{0u}^{\mathrm{IX}}}{2\pi u} &= E_{q3}^i \\
jk_xA'_0 - jk_yB'_0 - \frac{\Upsilon}{l} + \frac{\Lambda}{d} &= 0 \\
jk_xA'_0 - jk_3C'_0 - \Upsilon\left(\frac{1}{l}+\frac{1}{h}\right) - \frac{\Lambda}{h} &= 0
\end{aligned} \tag{5.45}$$

Using the approximate formulas given in (5.23)-(5.25), the incident electric fields can be

expressed as

$$\begin{bmatrix} E_x^i \\ E_y^i \\ E_{q3}^i \end{bmatrix} = \frac{\eta_0}{2k_0k_z} \begin{bmatrix} L_{11} & L_{12} & L_{13} \\ L_{21} & L_{22} & L_{23} \\ L_{31} & L_{32} & L_{33} \end{bmatrix} \begin{bmatrix} J_x \\ J_y \\ J_{q3} \end{bmatrix}$$

$$\begin{aligned}
L_{11} &= k_0^2 - k_x^2 + j\frac{dk_z}{\pi}\left(k_0^2 - \frac{lk_x^2}{d+h+l}\right)\ln\frac{d}{2\pi r_x} \\
L_{12} &= -k_xk_y\left(1 + j\frac{dlk_z}{(d+h+l)\pi}\ln\frac{d}{2\pi r_x}\right) \\
L_{13} &= -j\frac{dlk_xk_3k_z}{(d+h+l)\pi}\ln\frac{d}{2\pi r_x} - k_xk_3 + k_0^2\cos\psi \\
L_{21} &= -k_xk_y\left(1 + j\frac{dlk_z}{(d+h+l)\pi}\ln\frac{l}{2\pi r_y}\right) \\
L_{22} &= k_0^2 - k_y^2 + j\frac{lk_z}{\pi}\left(k_0^2 - \frac{dk_y^2}{d+h+l}\right)\ln\frac{l}{2\pi r_y} \\
L_{23} &= k_0^2\sin\psi - k_yk_3 - j\frac{dlk_yk_3k_z}{(d+h+l)\pi}\ln\frac{l}{2\pi r_y} \\
L_{31} &= k_0^2\cos\psi - k_xk_3 - j\frac{dlk_xk_3k_z}{(d+h+l)\pi}\ln\frac{t}{2\pi r_3} \\
L_{32} &= k_0^2\sin\psi - k_yk_3 - j\frac{dlk_yk_3k_z}{(d+h+l)\pi}\ln\frac{t}{2\pi r_3} \\
L_{33} &= k_0^2 - k_3^2 + j\frac{tk_z}{\pi}\left(k_0^2 - \frac{hk_3^2}{d+h+l}\right)\ln\frac{t}{2\pi r_3}
\end{aligned} \tag{5.46}$$

The scattered electric fields E_x^s, E_y^s, and E_{q3}^s at the plane of the grid along $\widehat{x}$, $\widehat{y}$, and $\widehat{q}_3$ can be written as

$$\begin{bmatrix} E_x^s \\ E_y^s \\ E_{q3}^s \end{bmatrix} = \frac{\eta_0}{2k_zk_0} \begin{bmatrix} Q_{11} & Q_{12} & Q_{13} \\ Q_{12} & Q_{22} & Q_{23} \\ Q_{13} & Q_{23} & Q_{33} \end{bmatrix} \begin{bmatrix} J_x \\ J_y \\ J_{q3} \end{bmatrix} \tag{5.47}$$

$$Q_{11} = k_x^2 - k_0^2,\ Q_{12} = k_xk_y,\ Q_{13} = k_3k_x - k_0^2\cos\psi$$

$$Q_{22} = k_y^2 - k_0^2,\ Q_{23} = k_3k_y - k_0^2\sin\psi,\ Q_{33} = k_3^2 - k_0^2$$

The same steps presented in Sec. 5.3 are then followed. Specifically, the total electric fields are found as the sum of the incident ((5.46)) and scattered ((5.47)) electric fields. The equivalence between wires and strips ((5.28)) is then used. Finally, from (5.35) the sheet impedance of a three-branch unit cell of strips (Fig. 5.4(b)) under oblique incidence

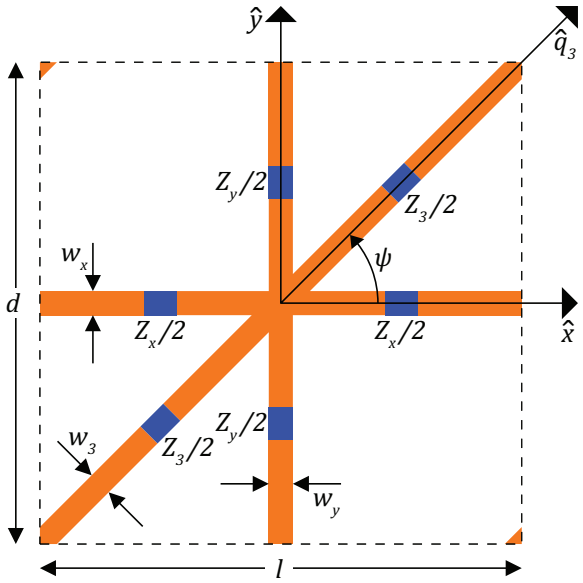

Figure 5.5: A loaded, three-branch unit cell comprising PEC strips and lumped components

is obtained

$$
\boxed{
\begin{aligned}
\overline{\overline{\eta}}_{\text{3-branch strips}}\left(\vec{k}_{tan}\right) &= \left(\overline{\overline{B}}^{\mathrm{T}}\,\overline{\overline{V}}^{-1}\left(\vec{k}_{tan}\right)\,\overline{\overline{B}}\right)^{-1} \\
\overline{\overline{V}}\left(\vec{k}_{tan}\right) &= -\frac{1}{(d+h+l)k_0^2}\begin{bmatrix} V_{11} & V_{12} & V_{13} \\ V_{21} & V_{22} & V_{23} \\ V_{31} & V_{32} & V_{33} \end{bmatrix} \\
V_{11} &= \left(lk_x^2-(d+h+l)k_0^2\right)\eta_s(d,w_x), V_{12} = lk_xk_y\eta_s(d,w_x) \\
V_{13} &= lk_xk_3\eta_s(d,w_x), V_{21} = dk_xk_y\eta_s(l,w_y), \\
V_{22} &= \left(dk_y^2-(d+h+l)k_0^2\right)\eta_s(l,w_y), V_{23} = dk_yk_3\eta_s(l,w_y) \\
V_{31} &= hk_xk_3\eta_s(t,w_3), V_{32} = hk_yk_3\eta_s(t,w_3), \\
V_{33} &= (hk_3^2-(d+h+l)k_0^2)\eta_s(t,w_3)
\end{aligned}
} \tag{5.48}
$$

Note that $\overline{\overline{B}}$ is defined in (5.32), $\eta_s(b,w)$ is defined in (5.6) and $k_3 = k_x\cos\psi + k_y\sin\psi$.

The sheet impedance of the loaded, three-branch unit cell of Fig. 5.5 is obtained using (5.35) and (5.48)

$$
\boxed{\overline{\overline{\eta}}_{\text{loaded, 3-branch strips}}\left(\vec{k}_{tan}\right) = \left(\overline{\overline{B}}^{\mathrm{T}}\left(\overline{\overline{V}}\left(\vec{k}_{tan}\right)+\overline{\overline{C}}\right)^{-1}\overline{\overline{B}}\right)^{-1}} \tag{5.49}
$$

It should be noted that the loaded, three-branch unit cell may exhibit an arbitrary sheet impedance for a given wave vector, by simply changing the loading elements. The physical geometry need not be changed.

5.6 Sliced Rectangle Unit Cell

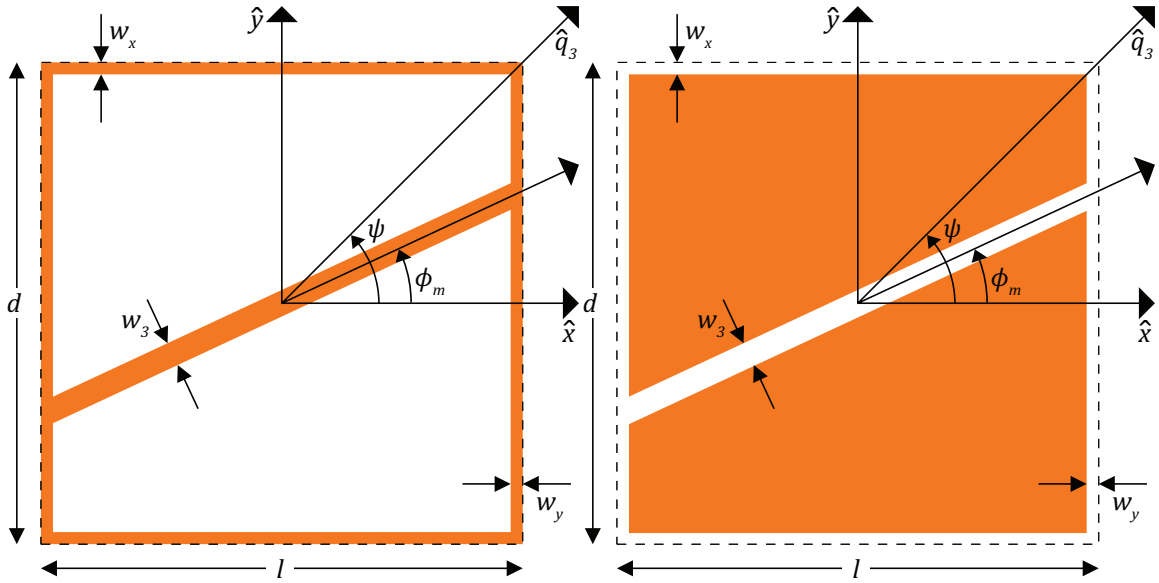

Figure 5.6: (a) Sliced rectangle, and (b) sliced patch unit cells

A geometry that is more general than the unloaded, three-branch unit cell is the sliced rectangle, shown in Fig. 5.6(a). It differs from the three-branch unit cell in that the central strip can form an arbitrary angle ϕ_m with $\widehat{x}$ $(0 \leq \phi_m \leq \pi)$. The complement of this unit cell is the sliced patch (Fig. 5.6(b)), which has been previously used to realize devices with tensorial surface properties [42, 114].

Eq. (5.48) provides the sheet impedance of the sliced rectangle (Fig. 5.6(a)) when $\phi_m = \psi$. In addition, its sheet impedance is known when $\phi_m = 0$ or $\pi/2$, where it reduces to an orthogonal grid [107, Eq. (4.54), (4.55)]. The sheet impedance of the sliced rectangle for arbitrary ϕ_m must change smoothly between these values. As a result, the following procedure is proposed to model the sheet impedance of the sliced rectangle:

- Calculate the diagonal elements of the sheet impedance when the central strip is aligned with the $\widehat{x}$-axis $(\phi_m = 0)$:

$$\eta_{xx}(\vec{k}_{tan}, \phi_m = 0) = \eta_s\left(\frac{d}{2}, w_x\right)\left(1 - \frac{l}{d/2 + l}\frac{k_x^2}{k_0^2}\right)$$
$$\eta_{yy}(\vec{k}_{tan}, \phi_m = 0) = \eta_s\left(l, w_y\right)\left(1 - \frac{d/2}{d/2 + l}\frac{k_y^2}{k_0^2}\right) \tag{5.50}$$

- Calculate the diagonal elements of the sheet impedance when the central strip is aligned with the $\widehat{y}$-axis ($\phi_m = \pi/2$):

$$\eta_{xx}\left(\vec{k}_{tan}, \phi_m = \frac{\pi}{2}\right) = \eta_s\left(d, w_x\right)\left(1 - \frac{l/2}{d + l/2}\frac{k_x^2}{k_0^2}\right)$$
$$\eta_{yy}\left(\vec{k}_{tan}, \phi_m = \frac{\pi}{2}\right) = \eta_s\left(\frac{l}{2}, w_y\right)\left(1 - \frac{d}{d + l/2}\frac{k_y^2}{k_0^2}\right) \tag{5.51}$$

- It is evident that the separation between adjacent central strips changes with ϕ_m, namely $t(\phi_m) = \frac{d}{2}|\text{cos}\phi_m| + \frac{l}{2}\text{sin}\phi_m$. Similarly, the wavenumber along the middle strip, k_3, becomes $k_3(\phi_m) = k_x\text{cos}\phi_m + k_y\text{sin}\phi_m$. Using these expressions in (5.48) allows $\overline{\overline{V}}\left(\vec{k}_{tan}, \phi_m\right)$ to be calculated.

- Calculate the 2x2 tensor $\overline{\overline{F}}\left(\vec{k}_{tan}, \phi_m\right)$, defined as:

$$\overline{\overline{F}}\left(\vec{k}_{tan}, \phi_m\right) = \left(\overline{\overline{B}}_1^{\text{T}}\,\overline{\overline{V}}^{-1}\left(\vec{k}_{tan}, \phi_m\right)\,\overline{\overline{B}}_2\right)^{-1}$$
$$\overline{\overline{B}}_1 = \begin{bmatrix} 1 & 0 \\ 0 & 1 \\ \text{cos}\phi_m & \text{sin}\phi_m \end{bmatrix}, \overline{\overline{B}}_2 = \begin{bmatrix} 1 & 0 \\ 0 & 1 \\ \text{sgn}(\text{cos}\phi_m)\frac{t(\phi_m)}{d} & \frac{t(\phi_m)}{l} \end{bmatrix} \tag{5.52}$$

where sgn(x) is the signum function. Note that when $\phi_m = \psi$, $\overline{\overline{F}}$ is equal to $\overline{\overline{\eta}}_{\text{3-branch strips}}\left(\vec{k}_{tan}\right)$.

- Finally, the sheet impedance of the sliced rectangle under oblique incidence is

$$\overline{\overline{\eta}}_{\text{sliced rect.}}\left(\vec{k}_{tan}, \phi_m\right) = \begin{bmatrix} \eta_{xx} & \eta_{xy} \\ \eta_{yx} & \eta_{yy} \end{bmatrix} \tag{5.53a}$$

For angles $0 \leq \phi_m \leq \psi$ or $\pi - \psi \leq \phi_m \leq \pi$:

$$\eta_{xx} = \eta_{xx}(\vec{k}_{tan}, 0) + \left(\overline{\overline{F}}[1,1] - \eta_{xx}(\vec{k}_{tan}, 0)\right)\frac{\text{sin}\phi_m}{\text{sin}\psi}$$
$$\eta_{xy} = \eta_{yx} = \overline{\overline{F}}[2,1] \tag{5.53b}$$
$$\eta_{yy} = \eta_{yy}(\vec{k}_{tan}, 0) + \left(\overline{\overline{F}}[2,2] - \eta_{yy}(\vec{k}_{tan}, 0)\right)\frac{\text{sin}^2\phi_m}{\text{sin}^2\psi}$$

where $\eta_{xx}(\vec{k}_{tan}, 0)$ and $\eta_{yy}(\vec{k}_{tan}, 0)$ are given in (5.50) and $\overline{\overline{F}}$ is given in (5.52). The square brackets denote the element of the tensor $\overline{\overline{F}}$.
For angles $\psi \leq \phi_m \leq \pi - \psi$:

$$\begin{aligned}
\eta_{xx} &= \eta_{xx}\left(\vec{k}_{tan}, \frac{\pi}{2}\right) + \left(\overline{\overline{F}}[1,1] - \eta_{xx}\left(\vec{k}_{tan}, \frac{\pi}{2}\right)\right) \frac{\cos^2\phi_m}{\cos^2\psi} \\
\eta_{xy} &= \eta_{yx} = \overline{\overline{F}}[1,2] \\
\eta_{yy} &= \eta_{yy}\left(\vec{k}_{tan}, \frac{\pi}{2}\right) + \left(\overline{\overline{F}}[2,2] - \eta_{yy}\left(\vec{k}_{tan}, \frac{\pi}{2}\right)\right) \frac{|\cos\phi_m|}{\cos\psi}
\end{aligned} \tag{5.53c}$$

where $\eta_{xx}(\vec{k}_{tan}, \pi/2)$ and $\eta_{yy}(\vec{k}_{tan}, \pi/2)$ are given in (5.51) and $\overline{\overline{F}}$ is given in (5.52).

Quantity $\overline{\overline{F}}$ in (5.52) and the sinusoidal interpolation functions in (5.53b) and (5.53c) were judiciously chosen. Parametric sweeps of the sliced rectangle unit cell were performed using a full-wave solver, which verified the model in (5.53). In the expressions for $\phi_m = 0$ and $\phi_m = \pi/2$ in (5.50) and (5.51), it has been assumed that $w_x \approx w_3$ and $w_y \approx w_3$, respectively.

The sheet impedance of the sliced patch (Fig. 5.6(b)) is obtained using the tensorial form of Babinet's principle ((5.31))

$$\boxed{\overline{\overline{\eta}}_{\text{sliced patch}}\left(\vec{k}_{tan}, \phi_m\right) = \frac{\eta_0^2}{4}\left(\overline{\overline{R}}^{\mathrm{T}}\,\overline{\overline{\eta}}_{\text{sliced rect.}}\left(\vec{k}_{tan}, \phi_m\right)\overline{\overline{R}}\right)^{-1}} \tag{5.54}$$

5.7 Full-Wave Verification

In this Section, full-wave simulations of the examined geometries are presented and compared to results from the analytical models. Simulations were performed using Ansys Electronics Desktop, a commercial full-wave electromagnetic solver. The direction of the wave vector is given in terms of the polar angle, θ, and the azimuthal angle, ϕ, in the spherical coordinate system [107, Eq. (4.20)]

$$k_x = k_0 \sin\theta\cos\phi, \quad k_y = k_0 \sin\theta\sin\phi \tag{5.55}$$

The procedure presented in [53] is used to simulate the metallic claddings in ANSYS Electronics Desktop and extract their sheet impedance. The claddings are simulated in free space.

First, results are considered for the sheet impedance of the unloaded, skewed unit cell

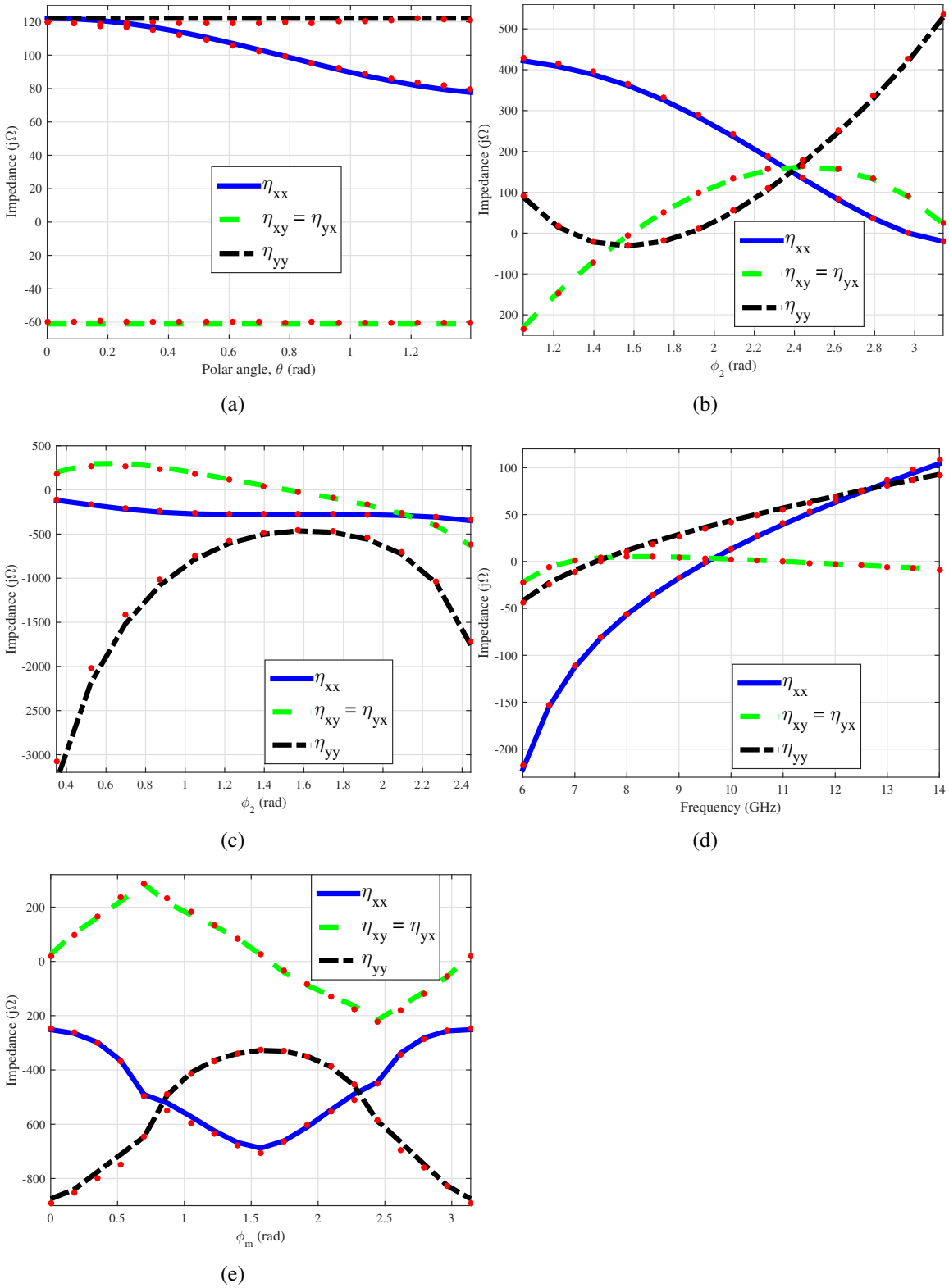

Figure 5.7: Numerical results for (a) an unloaded, skewed unit cell of strips, (b) a loaded, skewed unit cell of strips, (c) a skewed patch, (d) a loaded, three-branch unit cell of strips, and (e) a sliced patch. The lines correspond to analytical data, while the dots correspond to simulation results.

(Fig. 5.1(b)) at a frequency of 10 GHz ($\lambda = 3$ cm). The following physical parameters are assumed: $d = \lambda/10$, $l = \lambda/10$, $w_1 = w_2 = \lambda/300$, $\phi_1 = \pi/12$, $\phi_2 = 5\pi/12$. The azimuthal angle of incidence is $\phi = 0$. The analytical results from (5.29) and the corresponding simulation data for the elements of the reciprocal impedance tensor, η_{xx}, $\eta_{xy} = \eta_{yx}$, and η_{yy}, are shown in Fig. 5.7(a) when the polar angle of incidence, θ, ranges from 0 to almost $\pi/2$ (grazing incidence). The red dots denote ANSYS Electronics Desktop results.

Then, the sheet impedance of the loaded, skewed unit cell (Fig. 5.3(a)) is examined. The following physical parameters and lumped component values are assumed: $d = \lambda/7.5$, $l = \lambda/10$, $w_1 = w_2 = \lambda/300$, $\phi_1 = \pi/6$, $Z_1 = j\omega L_1$, $L_1 = 2$ nH, $Z_2 = \frac{1}{j\omega C_2}$, $C_2 = 0.1$ pF. The angle of incidence is $[\theta, \phi] = [\pi/4, \pi/3]$. The analytical results from (5.30) and the corresponding simulation data are shown in Fig. 5.7(b) when ϕ_2 ranges from $\pi/6$ to π.

Next, results for the skewed patch (Fig. 5.3(b)) with the following parameters are calculated at 10 GHz: $d = \lambda/10$, $l = \lambda/7.5$, $w_1 = \lambda/250$, $w_2 = \lambda/200$, $\phi_1 = -\pi/18$. The angle of incidence is $[\theta, \phi] = [\pi/3, \pi/6]$. Analytical results from (5.31) and simulation data are presented in Fig. 5.7(c) when ϕ_2 ranges from $\pi/9$ to $7\pi/9$.

Numerical results are also presented for the loaded, three-branch unit cell (Fig. 5.5). The following physical parameters and lumped component values are assumed ($\lambda = 3$ cm): $d = \lambda/7.5$, $l = \lambda/10$, $w_x = w_y = w_3 = \lambda/300$, $Z_x = \frac{1}{j\omega Cx}$, $C_x = 0.15$ pF, $Z_y = \frac{1}{j\omega C_y}$, $C_y = 0.2$ pF, $Z_3 = j\omega L_3$, $L_3 = 6$ nH. The angle of incidence is $[\theta, \phi] = [\pi/6, -\pi/6]$. Analytical results from (5.49) and simulation data are reported in Fig. 5.7(d) when the frequency of the impinging wave ranges from 6 to 14 GHz.

Finally, the sliced patch (Fig. 5.6(b)) is examined at a frequency of 10 GHz with the following parameters: $d = \lambda/10$, $l = \lambda/8$, $w_x = w_y = \lambda/300$, $w_3 = \lambda/250$. The angle of incidence is $[\theta, \phi] = [\pi/6, \pi/3]$. Fig. 5.7(e) shows the analytical results from (5.54) and the corresponding simulation data when the sliced angle ϕ_m ranges from 0 to π.

In all the examined cases, close agreement between analytical results and simulation data is observed. This confirms the validity of the analysis of the skewed and three-branch geometries, as well as the interpolation procedure used to model the sheet impedance of the sliced rectangle. As can be seen from Fig. 5.7, the examined unit cells can achieve a wide range of impedances, making them suitable for a variety of applications.

Cascaded metasurfaces consist of multiple metallic claddings, separated by thin dielectric substrates [52]. In this case, the technique presented in [99] can be used to find the approximate sheet impedance of a cladding in the presence of a dielectric substrate.

The models presented in this chapter are limited to claddings consisting of subwavelength unit cells formed by PEC strips or patches. Fig. 5.8(a) investigates the agree-

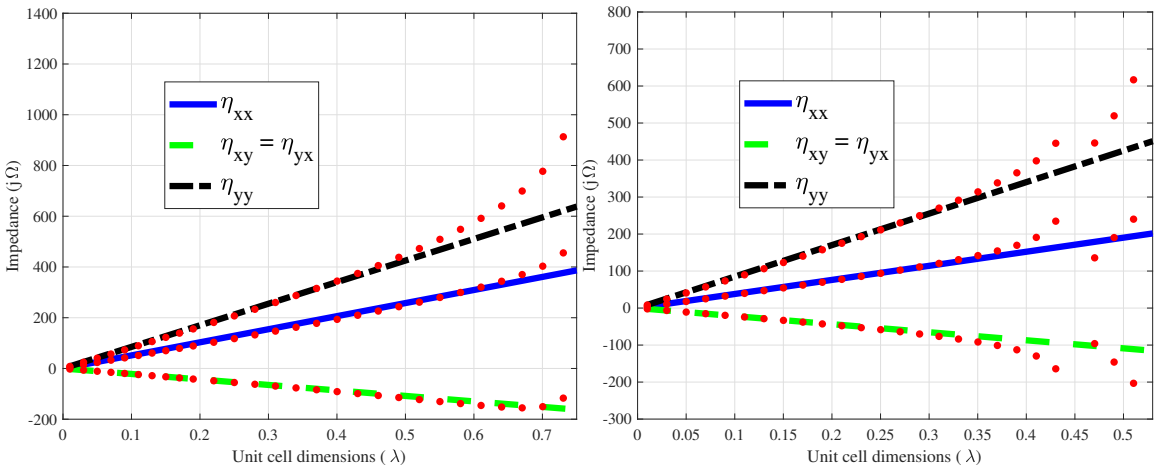

Figure 5.8: Numerical results for (a) a sliced rectangle under normal incidence and (b) a sliced rectangle under oblique incidence. The lines correspond to analytical data, while the dots correspond to simulation results.

ment between analytical and simulation data when the unit cell size becomes an appreciable fraction of the wavelength. Specifically, a sliced rectangle with $d = l = 3$ mm, $w_x = w_y = w_3 = 0.15$ mm, $\phi_m = \pi/6$ under normal incidence ($[\theta, \phi] = [0, 0]$) is examined. When the unit cell size exceeds half the wavelength, the discrepancy between analytical and simulation data becomes observable. The same unit cell is simulated under oblique incidence: $[\theta, \phi] = [\pi/4, 0]$. The results are shown in Fig. 5.8(b). In this case, the discrepancy between analytical and simulation data becomes observable when the unit cell size exceeds 0.35λ. The sheet impedance of larger unit cells can be found using the MoM procedure presented in Sec. 5.3 and 5.5. If the conductors have finite conductivity, a sheet resistance can be included into the MoM formulation.

5.8 Asymmetric linear polarizer

The analytical models developed previously are used to design an asymmetric linear polarizer under oblique incidence. As shown in Fig. 5.9, an asymmetric linear polarizer has the following functionalities [53]:

- transmits TM-polarized plane waves from side 1 and converts them to TE-polarized plane waves on side 2, and

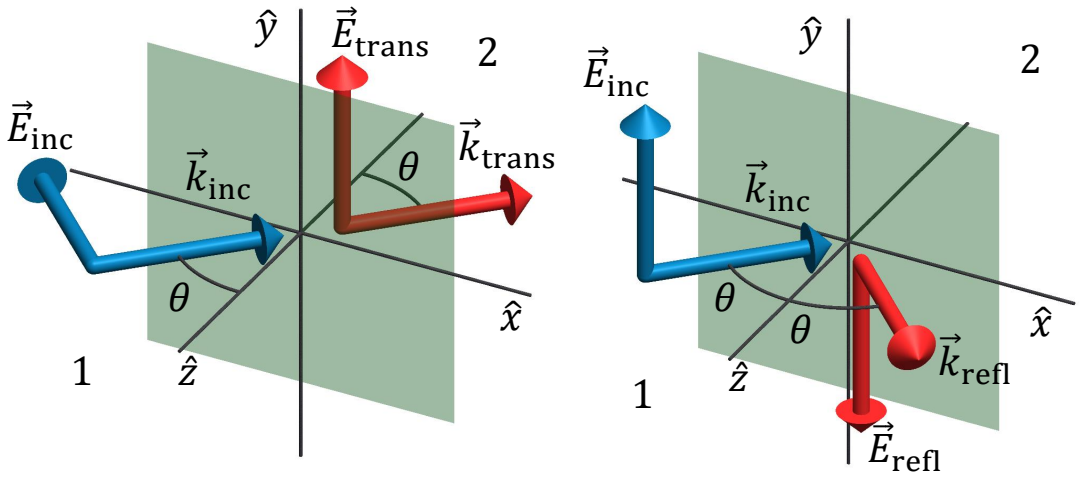

(a) (b)

Figure 5.9: The asymmetric linear polarizer: (a) transmits $\widehat{x}$-polarized plane waves from side 1 and converts them to $\widehat{y}$-polarized plane waves in side 2, and (b) reflects $\widehat{y}$-polarized plane waves from side 1.

- reflects TE-polarized plane waves from side 1.

Using the technique presented in [53], an asymmetric linear polarizer was designed using three sheets for an angle of incidence $(\theta, \phi) = (45°, 0)$ at 10 GHz. With reference to Fig. 5.10, the required sheet impedances are:

$$\overline{\overline{\eta}}_1 = \begin{bmatrix} -256.61 & 0 \\ 0 & 0 \end{bmatrix} j\Omega, \overline{\overline{\eta}}_2 = \begin{bmatrix} 44.52 & -50.28 \\ -50.28 & 44.52 \end{bmatrix} j\Omega, \overline{\overline{\eta}}_3 = \begin{bmatrix} 0 & 0 \\ 0 & -256.61 \end{bmatrix} j\Omega. \quad (5.56)$$

The sheets are separated by substrates with thicknesses:

$$t_1 = t_2 = 1.47 \text{ mm}, \quad (5.57)$$

and dielectric constants:

$$\varepsilon_{r1} = \varepsilon_{r2} = 9.8. \quad (5.58)$$

Rogers TMM® 10, with a dielectric constant of 9.8, is a suitable choice to realize the two spacers. This set of parameters leads to the S-parameters of the cascaded metasurface to be:

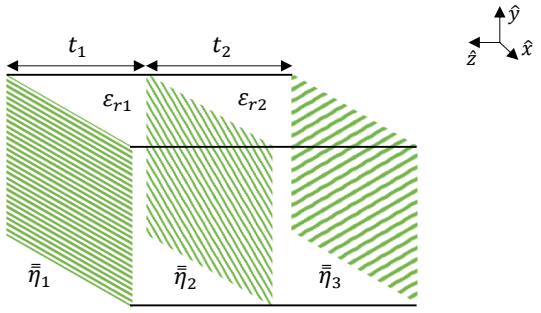

Figure 5.10: A three-layer metasurface consisting of three cascaded sheets and two dielectric slabs implements an asymmetric linear polarizer under oblique incidence.

$$\boldsymbol{S}_{11} = e^{j0}\begin{bmatrix} 0 & 0 \\ 0 & -1 \end{bmatrix}, \quad \boldsymbol{S}_{21} = e^{j0}\begin{bmatrix} 0 & 0 \\ j & 0 \end{bmatrix}, \quad \boldsymbol{S}_{22} = e^{j0}\begin{bmatrix} -1 & 0 \\ 0 & 0 \end{bmatrix}. \tag{5.59}$$

Port 1 is placed to the left of Fig. 5.10, while port 2 is to the right. Each port supports both $\widehat{x}$ and $\widehat{y}$ polarizations.

The design process is verified through simulation in ANSYS Electronics Desktop. Specifically, the sheet impedance, permittivity and thickness values are used to implement an asymmetric linear polarizer under oblique incidence at 10 GHz. The sheet impedances are modeled as ideal anisotropic impedance boundary conditions, while the dielectric slabs are modeled as lossless dielectric blocks. The electric field when the metasurface is illuminated with an obliquely incident TM plane wave is shown in Fig. 5.11(a). Full transmission and conversion from TM to TE are observed. The electric field when the metasurface is illuminated with a TE plane wave is shown in Fig. 5.11(b). Full reflection is observed. The S-parameters from simulation are:

$$\boldsymbol{S} = \begin{bmatrix} S_{11}^{xx} & S_{11}^{xy} & S_{12}^{xx} & S_{12}^{xy} \\ S_{11}^{yx} & S_{11}^{yy} & S_{12}^{yx} & S_{12}^{yy} \\ S_{21}^{xx} & S_{21}^{xy} & S_{22}^{xx} & S_{22}^{xy} \\ S_{21}^{yx} & S_{21}^{yy} & S_{22}^{yx} & S_{22}^{yy} \end{bmatrix} = e^{j0}\begin{bmatrix} 0 & 0 & 0 & j \\ 0 & -1 & 0 & 0 \\ 0 & 0 & -1 & 0 \\ j & 0 & 0 & 0 \end{bmatrix}. \tag{5.60}$$

The metasurface is implemented using patterned metallic claddings with 4×4 mm^2 unit cells. Sheets 1 and 3 are simply rotated (by $90°$) versions of each other. Sheet 1 is capacitive in $\widehat{x}$ and presents a short in $\widehat{y}$. A simple way to achieve this is by using a unit

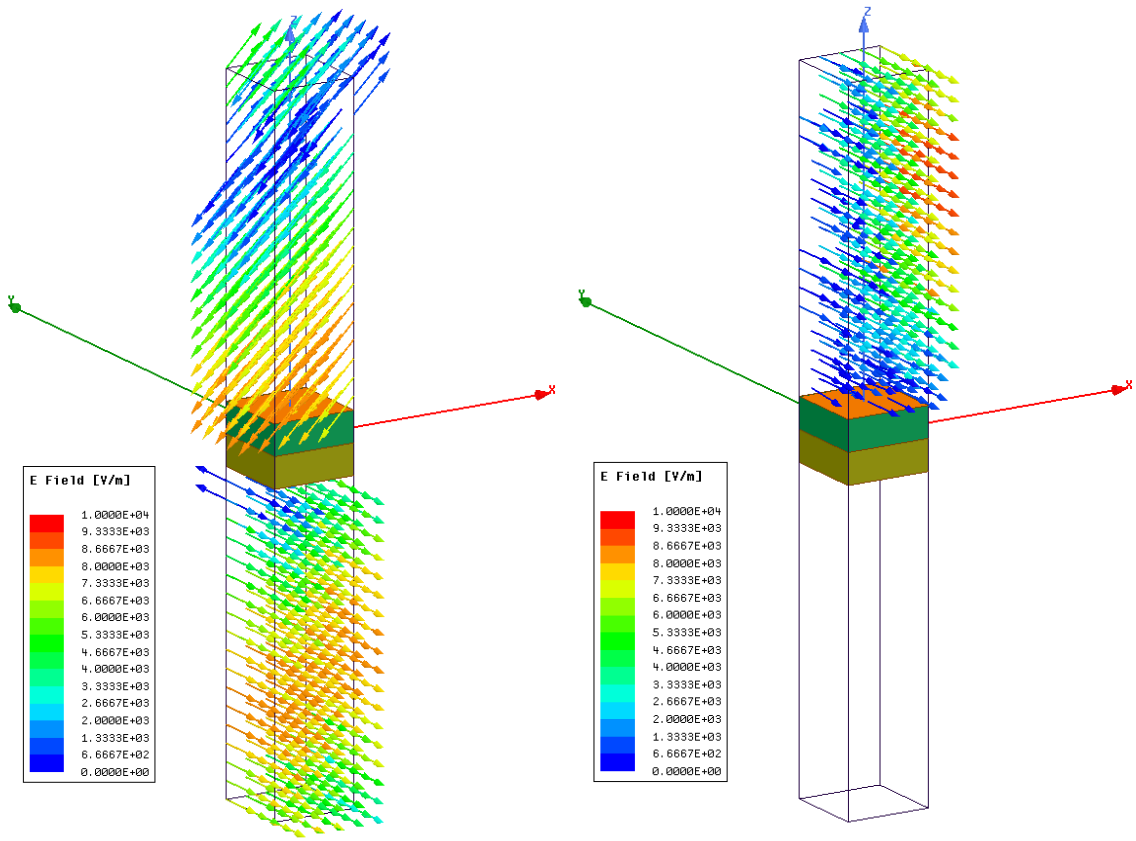

(a) (b)

Figure 5.11: The asymmetric linear polarizer simulated in ANSYS Electronics Desktop using ideal anisotropic impedance boundary conditions and lossless dielectric blocks: (a) TM-polarized plane waves from the top are transmitted and converted to TE-polarized plane waves on the bottom side, and (b) TE-polarized plane waves incident from the top side are reflected.

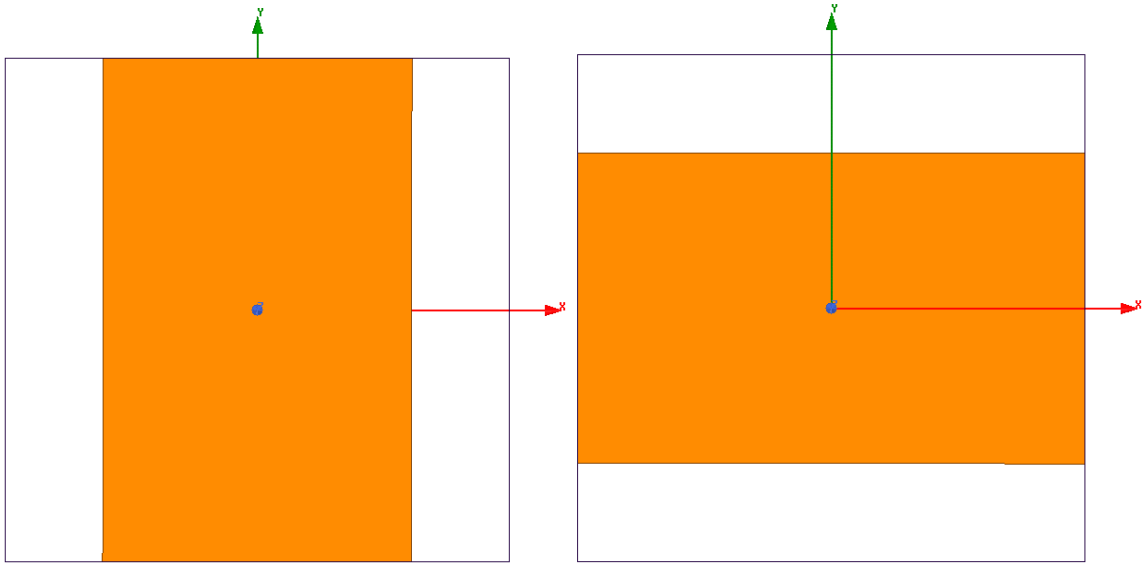

(a) (b)

Figure 5.12: Sheets (a) 1, and (b) 3 of the asymmetric linear polarizer implemented with patterned metallic sheets. The unit cell measures 4×4 mm^2, and the strip is 2.45 mm wide.

cell that contains a metallic strip of appropriate width, as shown in Fig. 5.12(a). According to the equations presented in [99], a strip with width 2.36 mm is needed. From full-wave simulations, a width of 2.45 mm yields optimal performance. Sheet 3 is shown in Fig. 5.12(b).

Sheet 2 should exhibit a full tensorial sheet impedance. The three-branch unit cell is chosen to implement sheet 2. With reference to Fig. 5.5, the following parameters are used:

$$\begin{aligned} w_x = 0.34\,\text{mm}, w_y = 0.4\,\text{mm}, w_3 = 0.28\,\text{mm}, l = d = 4\,\text{mm}, \\ Z_x = 0, \quad Z_y = 0, \quad Z_3 = 1/(j\omega C_3), \quad C_3 = 0.11\,\text{pF}. \end{aligned} \tag{5.61}$$

The capacitor along the diagonal strip is implemented using two gaps, as shown in Fig. 5.13(a). The implementation of all three sheets of the metasurface is shown in Fig. 5.13(b). Fig. 5.14(a) presents the reflection and transmission coefficients of the metasurface as a function of frequency. Its bandwidth is from 8 to 10.4 GHz. As prescribed, incident TM plane waves are converted to TE plane waves, while incident TE plane waves are reflected. Fig. 5.14(b) shows the transmission and reflection coefficients as a function of the angle of incidence, θ. The dependence of the metasurface's performance on the angle of incidence is negligible up to an angle of $80°$.

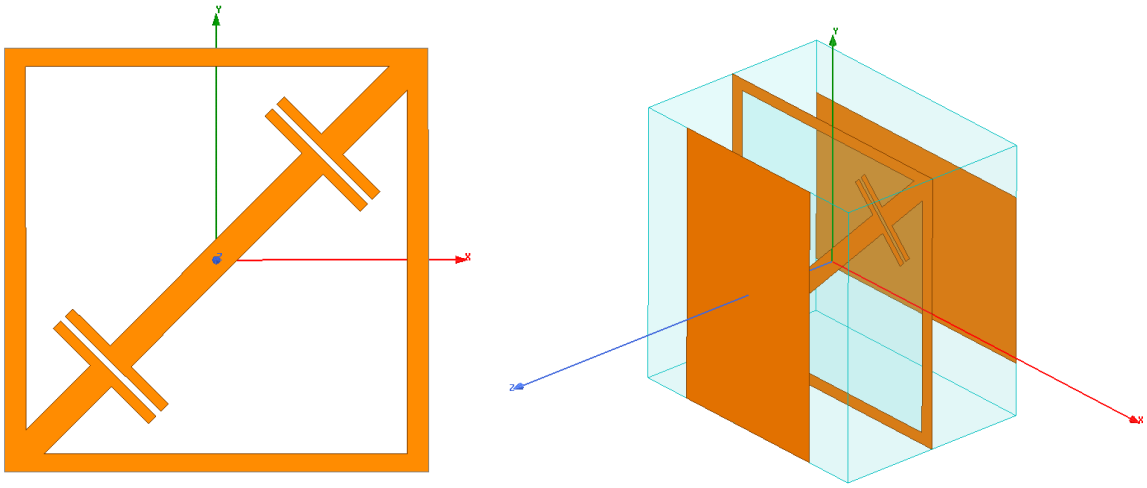

(a) (b)

Figure 5.13: (a) Sheet 2 of the asymmetric linear polarizer implemented with a patterned metallic sheet. A three-branch unit cell with the parameters in (5.61) is used. (b) The complete asymmetric linear polarizer metasurface.

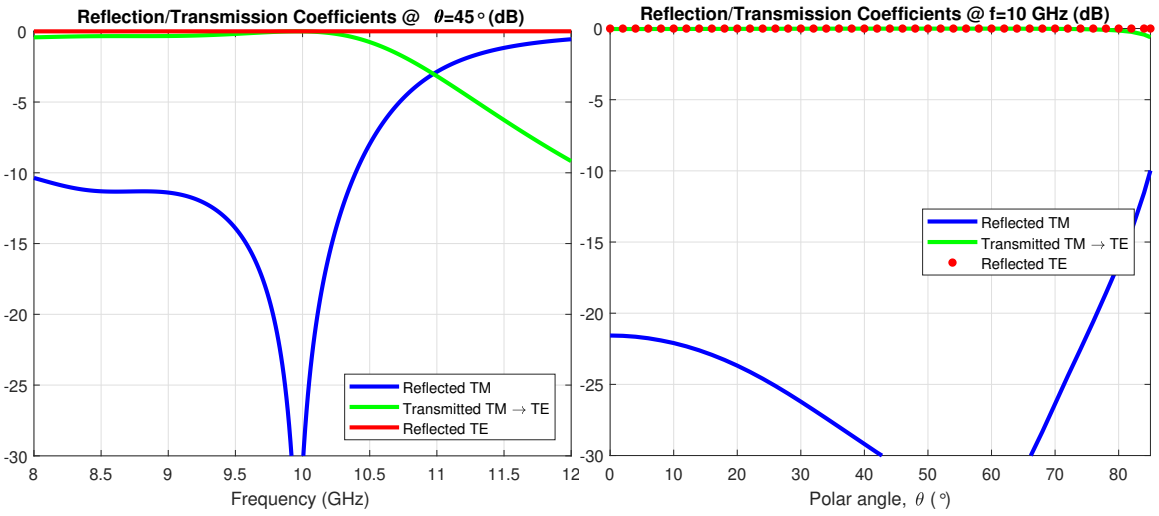

(a) (b)

Figure 5.14: The transmission and reflection coefficients of the asymmetric linear polarizer obtained through simulation in ANSYS Electronics Desktop as a function of (a) frequency, and (b) angle of incidence.

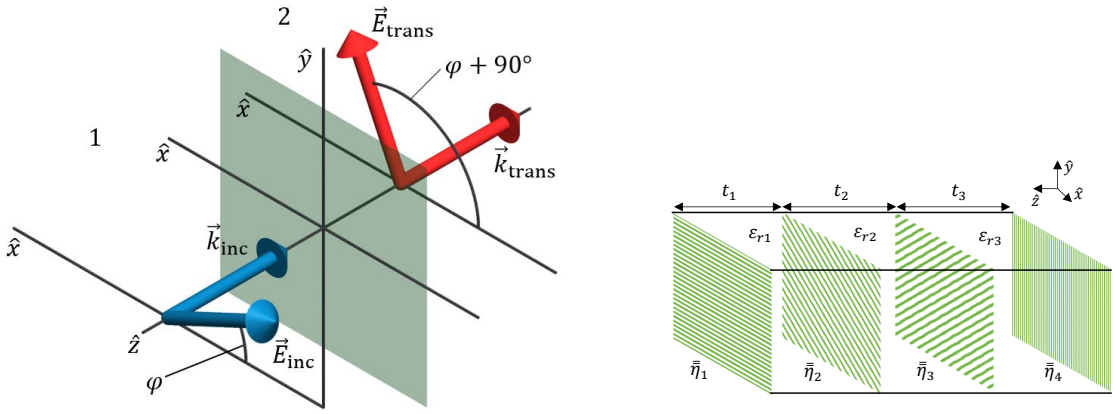

(a) (b)

Figure 5.15: (a) The polarization rotator changes the direction of the electric field of a normally incident plane wave by $90°$ upon transmission. (b) A four-layer metasurface consisting of four cascaded sheets and three dielectric slabs implements a polarization rotator under normal incidence.

5.9 Polarization rotator

The second metasurface synthesis example pertains to the design of a polarization rotator, operating under normal incidence at 10 GHz. Its function is shown in Fig. 5.15(a). The polarization of the incident wave on side 1 is rotated by $90°$ upon transmission to side 2.

Using the technique presented in [53], a polarization rotator can be realized with four sheets for angles of incidence $(\theta, \phi) = (0, 0)$ at 10 GHz. With reference to Fig. 5.15(b), the required sheet impedances are:

$$\begin{aligned} \bar{\bar{\eta}}_1 &= \begin{bmatrix} -80.00 & -40.00 \\ -40.00 & -80.00 \end{bmatrix} j\Omega, \quad \bar{\bar{\eta}}_2 = \begin{bmatrix} -100.04 & -49.99 \\ -49.99 & -100.04 \end{bmatrix} j\Omega, \\ \bar{\bar{\eta}}_3 &= \begin{bmatrix} -100.04 & -44.64 \\ -44.64 & -329.52 \end{bmatrix} j\Omega, \quad \bar{\bar{\eta}}_4 = \begin{bmatrix} -34.41 & 0 \\ 0 & 50.17 \end{bmatrix} j\Omega. \end{aligned} \tag{5.62}$$

The sheets are separated by substrates with thicknesses:

$$t_1 = 1.39 \text{ mm}, \quad t_2 = 4.28 \text{ mm}, \quad t_3 = 1.63 \text{ mm}, \tag{5.63}$$

and dielectric constants:

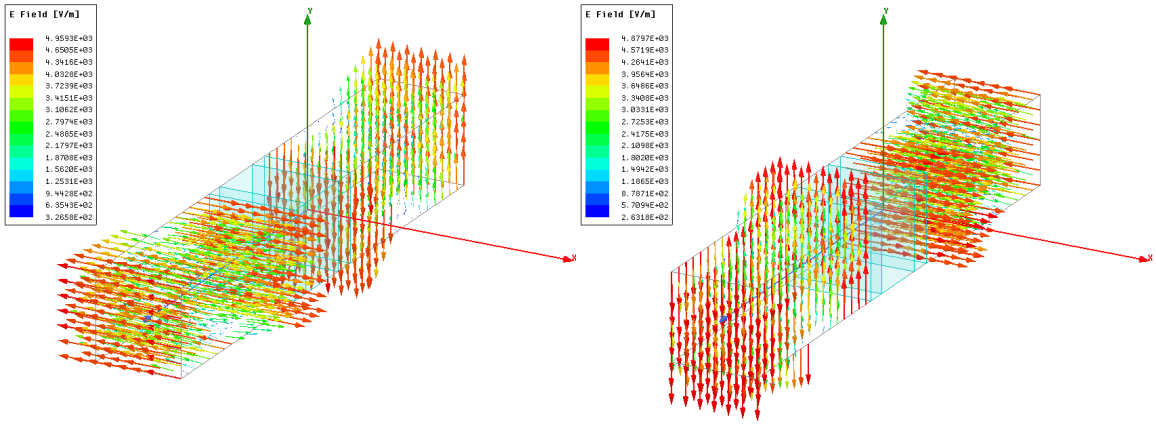

(a) (b)

Figure 5.16: The polarization rotator simulated in ANSYS Electronics Desktop using ideal anisotropic impedance boundary conditions and lossless dielectric blocks: (a) $\widehat{x}$-polarized plane waves are transmitted and converted to $\widehat{y}$-polarized plane waves, and (b) $\widehat{y}$-polarized plane waves are transmitted and converted to $\widehat{x}$-polarized plane waves.

$$\varepsilon_{r1} = 5.24, \quad \varepsilon_{r2} = 2, \quad \varepsilon_{r3} = 10. \tag{5.64}$$

This set of parameters results in the following S-parameters for the cascaded metasurface:

$$\boldsymbol{S}_{11} = \begin{bmatrix} 0 & 0 \\ 0 & 0 \end{bmatrix}, \boldsymbol{S}_{21} = e^{j\pi} \begin{bmatrix} 0 & -1 \\ 1 & 0 \end{bmatrix}, \boldsymbol{S}_{22} = \begin{bmatrix} 0 & 0 \\ 0 & 0 \end{bmatrix}. \tag{5.65}$$

The electric field resulting from the metasurface being illuminated with a normally incident, $\widehat{x}$-polarized plane wave is shown in Fig. 5.16(a). Full transmission and conversion from $\widehat{x}$ to $\widehat{y}$-polarization are observed. The electric field resulting from a $\widehat{y}$-polarized plane wave illumination is shown in Fig. 5.16(b). Full transmission and conversion from $\widehat{y}$ to $\widehat{x}$-polarization are observed.

Sheets 1 and 2 of the polarization rotator possess a capacitive sheet impedance with equal diagonal components. As a result, the complementary of the three-branch unit cell (a sliced patch unit cell with $\phi_m = \psi$) is the most suitable geometry to implement these two sheets. The 6×6 mm^2 unit cells for Sheets 1 and 2 are shown in Fig. 5.17(a) and 5.17(b), respectively.

The parameters for Sheet 1 are:

$$w_x = w_y = 0.19 \text{ mm}, w_3 = 0.25 \text{ mm}, \phi_m = \psi. \tag{5.66}$$

The parameters for Sheet 2 are:

$$w_x = w_y = 0.48 \text{ mm}, w_3 = 0.33 \text{ mm}, \phi_m = \psi. \tag{5.67}$$

Sheet 3 of the polarization rotator possesses a capacitive sheet impedance with unequal diagonal components. As a result, a sliced patch unit cell is the most suitable geometry to implement this sheet. It is shown in Fig. 5.17(c). The parameters for Sheet 3 are:

$$w_x = 0.78 \text{ mm}, w_y = 2.07 \text{ mm}, w_3 = 1.35 \text{ mm}, \phi_m = 2.91 \text{ rad}. \tag{5.68}$$

Sheet 4 possesses a sheet impedance with zero off-diagonal values. An orthogonal grid loaded with a capacitor (gap) in the $\widehat{x}$-direction is the most suitable geometry to implement this sheet. It is shown in Fig. 5.17(d). The parameters for Sheet 4 are:

$$w_x = 1.26 \text{ mm}, w_y = 2.10 \text{ mm}. \tag{5.69}$$

The implementation of all four sheets of the metasurface is shown in Fig. 5.18. Fig. 5.19(a) presents the reflection and transmission coefficients of the metasurface as a function of frequency. The metasurface is illuminated with a normally incident $\widehat{x}$-polarized plane wave ($\varphi = 0$ with reference to Fig. 5.15(a)). As a result, co-pol refers to $\widehat{x}$-polarization, while x-pol (cross polarization) refers to $\widehat{y}$-polarization. It can be seen that the incident wave gets entirely transmitted and converted to x-pol, while the co- and x-pol reflections, as well as the co-pol transmission, are negligible.

Fig. 5.19(b) presents the reflection and transmission coefficients of the metasurface as a function of azimuthal angle, φ, at 10 GHz. The polarization of the incident plane wave is rotated to verify that the metasurface operates as a polarization rotator, as intended. The transmitted co-pol is always close to 0 dB, while the co- and x-pol reflections, as well as the co-pol transmission, are below -15 dB.

5.10 Chapter Summary

In this chapter, the sheet impedances of general-purpose tensor metasurface geometries were found analytically. The subwavelength size of the examined unit cells allowed for simple, yet accurate expressions for the sheet impedance. Specifically, three unit cells were

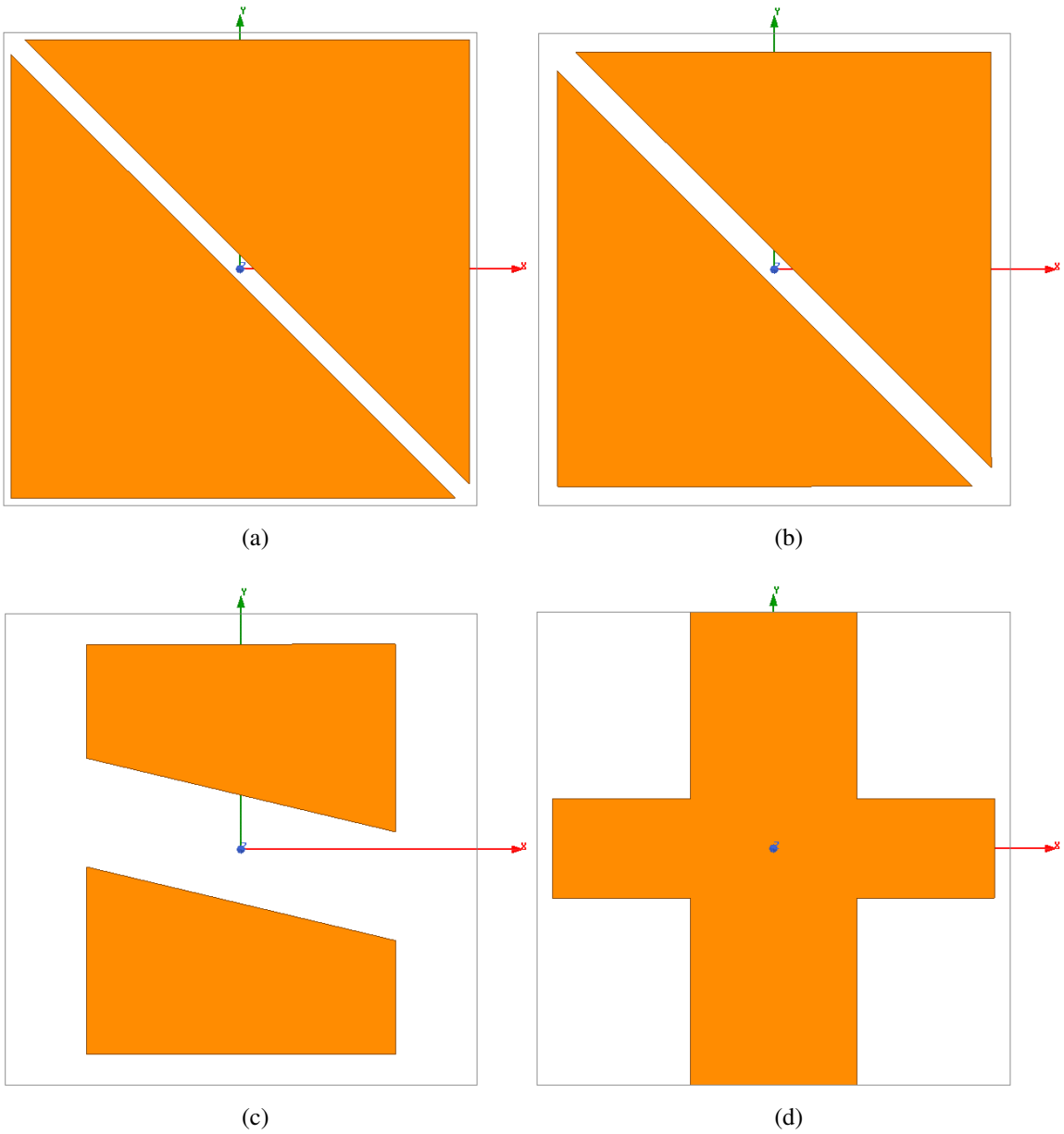

Figure 5.17: Sheets (a) 1, (b) 2, (c) 3, and (d) 4 of the polarization rotator metasurface implemented with patterned metallic sheets using 6×6 mm^2 unit cells.

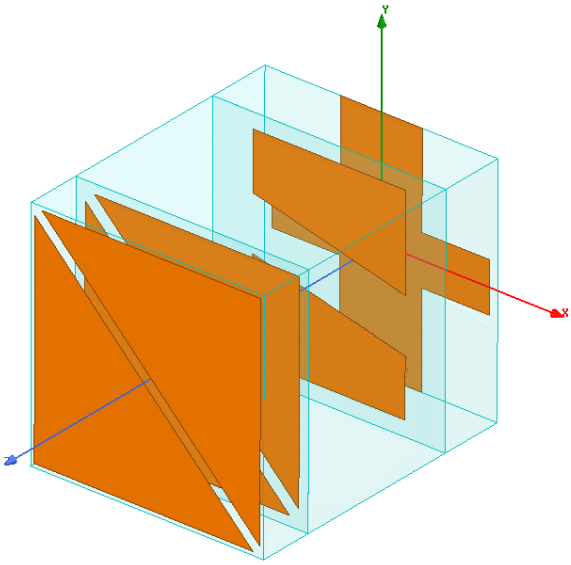

Figure 5.18: The complete polarization rotator metasurface.

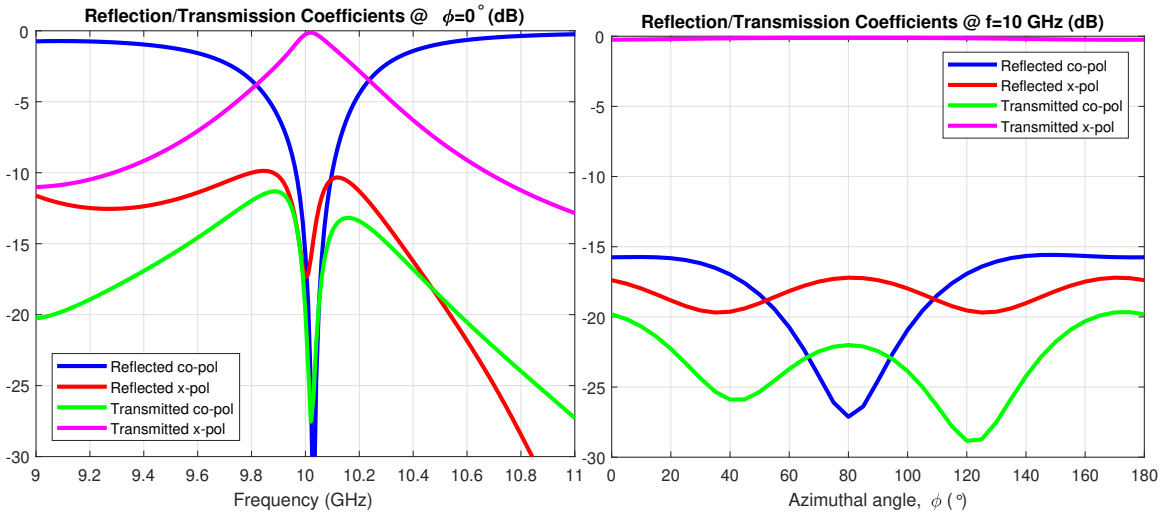

(a) (b)

Figure 5.19: The transmission and reflection coefficients of the polarization rotator obtained through simulation in ANSYS Electronics Desktop as a function of (a) frequency, and (b) azimuthal angle, φ (see Fig. 5.15(a)).

examined under arbitrary incidence. These included the skewed unit cell, the three-branch unit cell and the sliced rectangle. Expressions for variations of these unit cells, namely loaded and complementary ones, were also reported. The derived models were compared to full-wave simulations and close agreement was observed. Two metasurfaces, an asymmetric linear polarizer and a polarization rotator, operating at 10 GHz were designed to showcase the usefulness of the geometries analyzed.

The present work is expected to expedite the design of metasurfaces, where researchers are constantly tasked with relating electrical properties to realizable geometries. Claddings with homogeneous or inhomogeneous full tensorial impedances can now be designed analytically for arbitrary incidence, reducing the needed number of full-wave simulations. The proposed geometries can achieve a wide range of impedances and provide flexibility when fabrication or bandwidth issues need to be addressed. Although the primary motivation behind this work was the implementation of claddings for metasurfaces, the analyzed geometries can be used in any application that requires patterned metallic claddings, such as printed-circuit tensor impedance surfaces, leaky wave antennas, frequency selective surfaces and high-impedance surfaces.

CHAPTER 6

Conclusion

6.1 Summary of Contributions and Future Work

In this thesis, various methods for manipulating electromagnetic fields were presented. The techniques outlined here covered a wide spectrum of applications, ranging from the reactive near field to the far field. A summary of the contributions is given in this chapter for each topic discussed. Potential future directions that are relevant to this work are also given.

6.1.1 Electrically Small Antennas

In Chapter 2, ESAs for compact IoT nodes were presented. These antennas must be carefully designed in order to maintain their performance in an adverse near-field environment. Two elementary radiators were examined at the mm- and cm-scale: an electric dipole (linear wire), and a magnetic dipole (loop). It was found that although electric dipoles are more efficient than magnetic dipoles standalone. However, when the losses in the required matching components are taken into account, magnetic dipoles are overall more efficient.

Knowing that magnetic dipoles are better suited for compact IoT nodes, we developed a new class of magnetic dipoles, called 3D loops. By taking advantage of the height of the antenna, we were able to produce a design that has two solid metal planes that can be used by other components of the system as ground planes. The presence of the metal planes isolates the antenna from those components, and helps maintain its efficiency. These 3D loops were used in two practical systems that were developed in collaboration with other groups at the University of Michigan: an ISM band transceiver, and a GPS receiver.

These antennas, together with the integrated chips driving them, are slated to be used in upcoming systems that transmit images or audio. A potential direction for future work includes the fabrication of the antennas with the rest of the PCBs in the system in a single, multilayer design. This would improve their connection, both electrically as well as mechanically.

The applications that this antenna was designed for are inherently narrowband, so the antenna bandwidth was not a concern. It would be interesting to investigate whether any modifications could be made to the antenna in order to improve its bandwidth. This could potentially make it a good candidate for applications that require more bandwidth, such as the transmission of video.

6.1.2 Nondiffracting Waves

Significant advancements were presented in the field of nondiffracting waves, which exist in the radiative near field.

In Chapter 3, a broadband Bessel beam radiator based on refractive optics was outlined. The principle of operation, based on the refraction and reflection of rays within a homogeneous dielectric region, was explained. The device's ability to generate Bessel beams over a broad bandwidth was verified in simulation. Measurements on a fabricated prototype confirmed the simulation results. Using both frequency and time domain experimental data, it was shown that the device can generate X waves. These are short localized pulses that do not diffract or disperse as they propagate in the radiative near field. This was the first demonstration of X waves in the microwave region where the fields and pulses were thoroughly measured.

In Chapter 4, a Bessel beam radiator using a metamaterial region to bend the rays of an electric monopole was presented. The design procedure, based on QCTO, was outlined, and verified through simulation results. A design procedure based on metamaterial synthesis was employed to implement the device using rotationally symmetric unit cells. Simulation results confirmed the validity of this approach. Experimental results from a fabricated prototype were presented, showing good agreement with those obtained through simulation. Using simulation and experimental data, it was shown that the device is capable of generating X waves in its radiative near field.

The are multiple future directions that could be explored based on this research. One could investigate other techniques of generating Bessel beams, including flat radiators that would occupy less space. Techniques to enhance the bandwidth could also be studied, such as the incorporation of a feed with broader bandwidth, or by changing the materials used. As a result, the device would be able to radiate even shorter pulses. The advancement of novel fabrication techniques, e.g. ceramic stereolithography, could provide an alternate path of realizing devices like the ones presented here.

The work in this thesis filled a void in the experimental demonstration of exotic beams and pulses that until recently were treated in a theoretical framework. This opens up a new

range of possibilities in the experimental demonstration of other interesting phenomena, such as Y waves or Frozen waves.

6.1.3 Metasurfaces

Chapter 5 presented analytical models for the sheet impedance tensor of various unit cells used in metasurfaces. An MoM procedure served as the starting point for the analysis of unit cells consisting of intersecting metallic strips. By increasing the convergence of the method, a single harmonic was shown to be sufficient. As a result, analytical expressions were obtained for the skewed unit cell and the three-branch unit cell under arbitrary incidence. The effect of loading these unit cells with lumped components was also studied. Complementary structures were treated through the use of Babinet's principle in tensorial form. A related geometry, the sliced patch, was modeled through interpolation. The analytical results were compared to those obtained from simulation and excellent agreement was observed in the long wavelength limit.

To show the utility of the analytical expressions, the developed models were then used to design two metasurfaces at 10 GHz: an asymmetric linear polarizer, and a polarization rotator. The asymmetric linear polarizer converts TM waves to TE ones, while it reflects TE waves. It was implemented using three sheets. The outer sheets were identical apart from a 90° rotation between them. The middle sheet was implemented using a capacitvely-loaded three-branch unit cell. The polarization rotator was realized using four sheets. Three of the sheets were implemented using the sliced patch unit cell, while the fourth sheet consisted of a capacitvely-loaded orthogonal grid. Simulation results verified the performance of the designs.

A large range of metasurfaces can be designed using the models introduced in this work. Even though the design examples were both at 10 GHz, the models can be used to realize an arbitrary sheet impedance and are valid as long as one operates in the long wavelength limit. Additional geometries could be investigated analytically to provide even more options for designers. One could also incorporate techniques that take into account the plasmonic nature of metals at higher frequencies, to make them suitable for use even at optical frequencies.

The patterned metallic sheets modeled here could also be used in applications outside of metasurfaces. Leaky wave antennas, high impedance surfaces, absorbers or reflectarrays that often use inhomogeneous patterned sheets would serve as prime candidates. The analytical models can describe the frequency or angular response of these devices, reducing the need for time- and resource consuming simulations.

6.2 List of Publications

The work presented in this thesis has been submitted or published in the following journal papers and conference proceedings.

6.2.1 Journal Papers

1. **N. Chiotellis**, L.-X. Chuo, H. Kim, Y. Chen, H.-S. Kim, D. D. Wentzloff, D. Blaauw, and A. Grbic, "Electrically small loop antennas for compact IoT devices," *under review*.

2. **N. Chiotellis**, V. Mendez, S. M. Rudolph, and A. Grbic, "Experimental demonstration of highly localized pulses (X waves) at microwave frequencies," *Physical Review B*, vol. 97, no. 8, p. 085136, 2018.

3. T. Jang, G. Kim, B. Kempke, M. B. Henry, **N. Chiotellis**, C. Pfeiffer, D. Kim, Y. Kim, Z. Foo, H. Kim, A. Grbic, D. Sylvester, H.-S. Kim, D. D. Wentzloff, and D. Blaauw, "Circuit and system designs of ultra-low power sensor nodes with illustration in a miniaturized GNSS logger for position tracking: Part II - Data communication, energy harvesting, power management, and digital circuits," *IEEE Transactions on Circuits and Systems I: Regular Papers*, vol. 64, no. 9, pp. 2250-2262, 2017.

4. T. Jang, G. Kim, B. Kempke, M. B. Henry, **N. Chiotellis**, C. Pfeiffer, D. Kim, Y. Kim, Z. Foo, H. Kim, A. Grbic, D. Sylvester, H.-S. Kim, D. D. Wentzloff, and D. Blaauw, "Circuit and system designs of ultra-low power sensor nodes with illustration in a miniaturized GNSS logger for position tracking: Part I - Analog circuit techniques," *IEEE Transactions on Circuits and Systems I: Regular Papers*, vol. 64, no. 9, pp. 2237-2249, 2017.

5. Y. Chen, **N. Chiotellis**, L.-X. Chuo, C. Pfeiffer, Y. Shi, R. G. Dreslinski, A. Grbic, T. Mudge, D. D. Wentzloff, D. Blaauw, and H.-S. Kim, "Energy-autonomous wireless communication for millimeter-scale Internet-of-Things sensor nodes," *IEEE Journal on Selected Areas in Communications*, vol. 34, no. 12, pp. 3962-3977, 2016.

6. **N. Chiotellis** and A. Grbic, "Analytical modeling of tensor metasurfaces," *JOSA B*, vol. 33, no. 2, pp. A51-A60, 2016.

6.2.2 Conference Proceedings

1. **N. Chiotellis** and A. Grbic, "Space-time focusing using a dispersive axicon," in *Antennas and Propagation & USNC/URSI National Radio Science Meeting, 2018 IEEE International Symposium on*. IEEE, 2018, pp. 433-434.

2. H. Kim, **N. Chiotellis**, E. Ansari, M. Faisal, T. Jang, A. Grbic, H.-S. Kim, D. Blaauw, and D. D. Wentzloff, "A receiver/antenna co-design for a 1.5 mJ per fix fully-integrated 10x10x6mm^3 GPS logger," in *Custom Integrated Circuits Conference (CICC), 2018 IEEE*. IEEE, 2018, pp. 1-4.

3. **N. Chiotellis** and A. Grbic, "Metamaterial-based Bessel beam launcher," in Engineered Materials Platforms for Novel Wave Phenomena (Metamaterials), *2017 11th International Congress on*. IEEE, 2017, pp. 55-57.

4. **N. Chiotellis** and A. Grbic, "Metamaterial Bessel beam radiator," in *Antennas and Propagation & USNC/URSI National Radio Science Meeting, 2017 IEEE International Symposium on*. IEEE, 2017, pp. 1735-1736.

5. L.-X. Chuo, Y. Shi, Z. Luo, **N. Chiotellis**, Z. Foo, G. Kim, Y. Kim, A. Grbic, D. D. Wentzloff, H.-S. Kim, and D. Blaauw, "7.4 A 915MHz asymmetric radio using Q-enhanced amplifier for a fully integrated 3x3x3mm^3 wireless sensor node with 20m non-line-of-sight communication," in *Solid-State Circuits Conference (ISSCC), 2017 IEEE International*. IEEE, 2017, pp. 132-133.

6. **N. Chiotellis** and A. Grbic, "A broadband, Bessel beam radiator," in *Antennas and Propagation & USNC/URSI National Radio Science Meeting, 2016 IEEE International Symposium on*. IEEE, 2016, pp. 873-874.

7. **N. Chiotellis** and A. Grbic, "Towards the analytical design of bianisotropic metasurfaces," in *6th International Conference on Metamaterials, Photonic Crystals and Plasmonics META 2015*, pp. 1185-1186.

8. **N. Chiotellis** and A. Grbic, "Towards the analytical design of tensor metasurfaces," in *Antennas and Propagation & USNC/URSI National Radio Science Meeting, 2015 IEEE International Symposium on*. IEEE, 2015, pp. 1094-1095.

APPENDIX A

Comparison between Bessel and Gaussian beams

In this Appendix, Bessel and Gaussian beams are compared in terms of how effectively they can transfer power from a transmitting (radiating) aperture to a receiving one. This is a rather complex problem when treated thoroughly [115, 116]. Here, the aim is to demonstrate that Bessel beams can outperform Gaussian beams under certain circumstances, making their study worthwhile.

The following assumptions are made in this comparison of Bessel and Gaussian beams

- The operating frequency is 10 GHz.
- The transmitting and receiving apertures are $\rho_{max} = 0.05$ m in radius, centered along the $\widehat{z}$-axis. The transmitting aperture is placed at $z = 0$ and the field outside of it is assumed to be 0. The two apertures are identical in terms of the fields they support.
- The Bessel beam has cone angle $\theta = 13.27°$, with a linearly polarized tangential electric field that follows a $J_0(k_0 \sin\theta \rho)$ distribution, where k_0 is the wavenumber in free space. The cone angle has been chosen so that the first zero of the Bessel beam coincides with $\rho = \rho_{max}$. The nondiffracting range extends to $z_{max} = 0.212$ m.
- The Gaussian beam is focused (exhibits smallest waist) at the transmitting aperture. The waist radius is set to $w_0 = 0.425\rho_{max}$, so that the field at the edge of the aperture is almost 0 (-48 dB).

The electric field (E_x) profiles of the two beams are plotted in Fig. A.1(a).

To assess the coupling between the identical transmitting and receiving apertures, the following reaction integral is calculated [57, 115]:

$$< aRb >= \frac{|\iint_S \vec{H}_{21}(z) \cdot \vec{M}_2 dS|^2}{16P_1^2}, \tag{A.1}$$

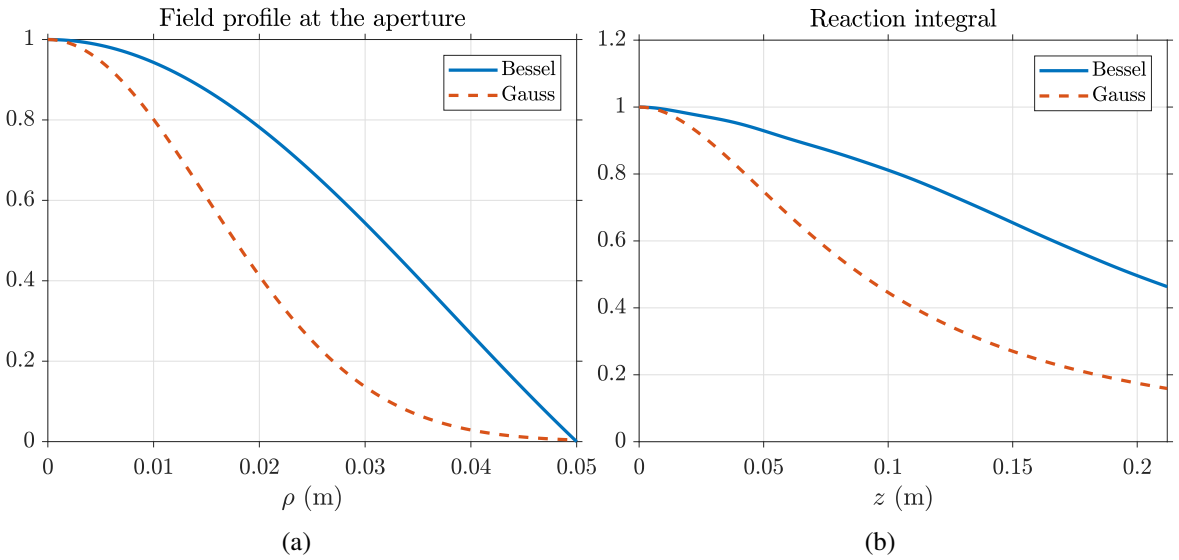

Figure A.1: (a) The electric field (E_x) profiles for the two beams on the radiating aperture as a function of ρ. (b) The reaction integral in (A.1) for the two beams as a function of z.

where $\vec{H}_{21}$ is the magnetic field generated by the transmitting aperture at the receiving aperture, $\vec{M}_2$, is the magnetic current distribution on the receiving aperture, and P_1 is the transmitted power.

The magnetic field generated by the transmitting aperture at the receiving one, $\vec{H}_{21}(z) = H_{21x}(z)\widehat{x} + H_{21y}(z)\widehat{y}$, is calculated using the Fourier transform method [57].

The magnetic current distribution, $\vec{M}_2$, is calculated as

$$\vec{M}_2 = -2\,\widehat{n} \times \vec{E}_2 \overset{\widehat{n}=-\widehat{z}}{=} 2\,\widehat{z} \times \vec{E}_2 = 2\,\widehat{z} \times (E_{2x}\widehat{x} + E_{2y}\widehat{y}) = 2(E_{2x}\widehat{y} - E_{2y}\widehat{x}), \tag{A.2}$$

where E_{2x} and E_{2y} are the cartesian components of the electric field of the receiving aperture.

The transmitted power is found by integrating the Poynting vector on the transmitting aperture

$$P_1 = \iint_S \frac{1}{2}\Re\{E_{1x}H_{1y}^* - E_{1y}H_{1x}^*\}dS. \tag{A.3}$$

The result of the reaction integral in (A.1) as a function of z is plotted in Fig. A.1(b). It can be seen that the Bessel beam performs better than the Gaussian beam in this case, given that it can deliver more power to the receiving aperture.

The evolution of a uniform spectrum pulse between 5 and 15 GHz emitted by the Bessel aperture at $t = 10$ ns is shown in Fig. A.2(a-d) at $t = 10.1$, 10.3, 10.5, and 10.7 ns, respectively. The evolution of an identical pulse emitted by the Gaussian aperture is shown in Fig. A.2(e-h) at the same four times. The maximum value of the two pulses is plotted in Fig. A.3 as a function of time. The pulse emitted by the Bessel aperture has approximately twice the amplitude of the pulse emitted by the Gaussian aperture at $t = 10.7$ ns, when the pulses reach the nondiffracting range of the Bessel aperture ($z_{max} = 0.212$ m).

The pulse size as a function of time is calculated for each pulse as

$$\Delta A(t) = \frac{\int_z \int_\rho |E_x(\rho, z, t)|^2 d\rho dz}{|E_{x,\text{max}}(t)|^2}. \tag{A.4}$$

A smaller pulse size corresponds to a higher spatial confinement of the pulse. The pulse size is plotted in Fig. A.4 for the Bessel and Guassian pulses. The Bessel pulse exhibits a smaller pulse size for $t > 10.15$ ns.

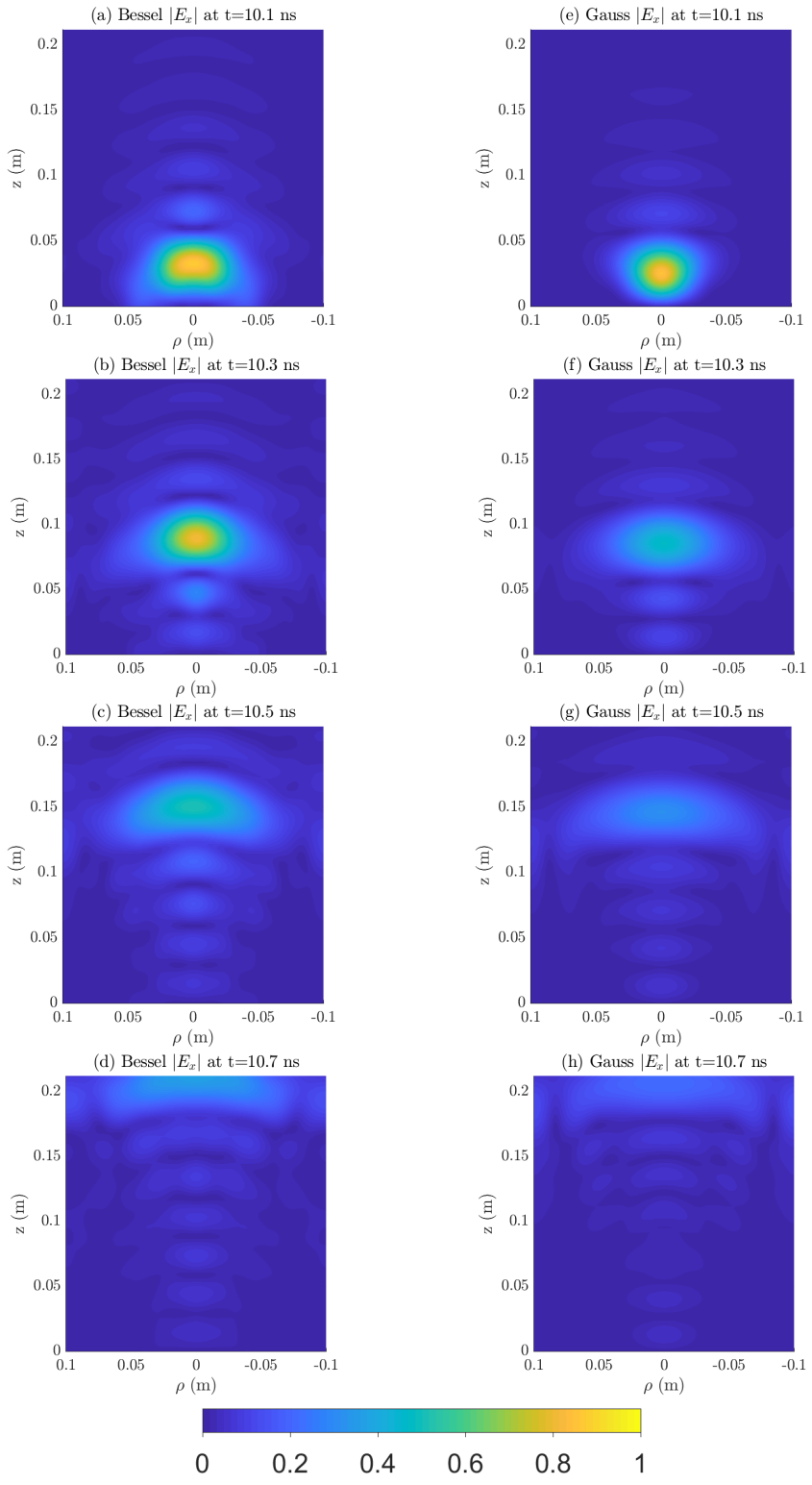

Figure A.2: (a-d) The evolution of the pulse emitted by the Bessel aperture observed at $t = 10.1$, 10.3, 10.5, and 10.7 ns, respectively. (e-h) The evolution of the pulse emitted by the Gaussian aperture observed at $t = 10.1$, 10.3, 10.5, and 10.7 ns, respectively.

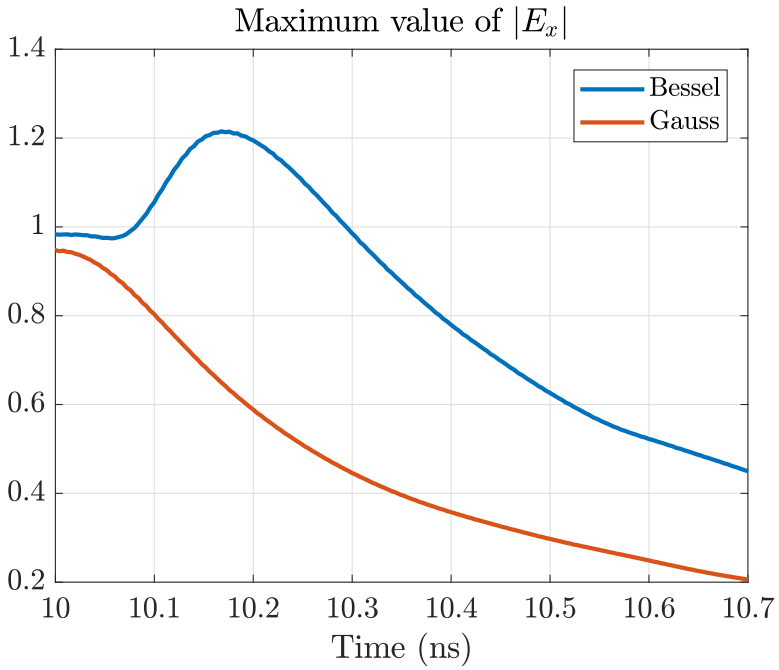

Figure A.3: The maximum value of the electric field amplitude of the two pulses emitted by Bessel and Gaussian apertures as a function of time.

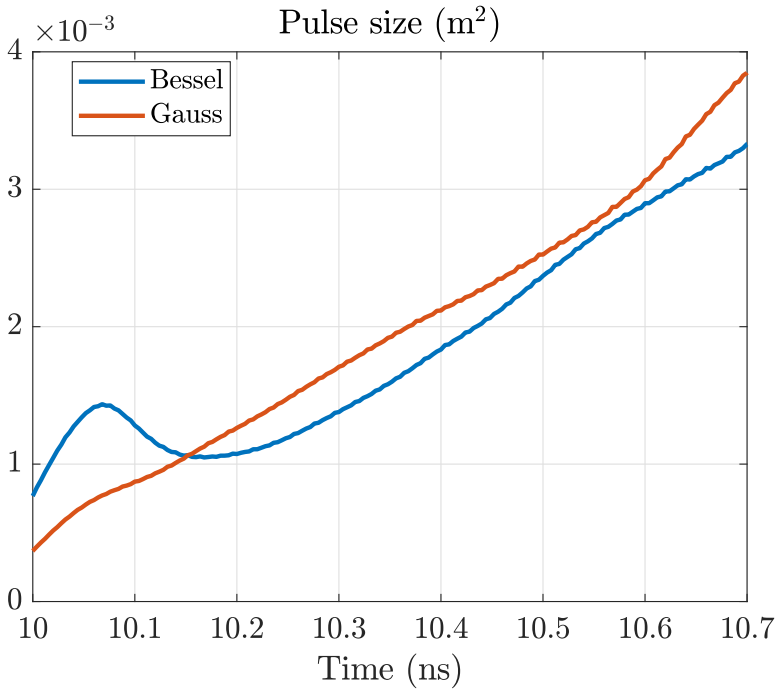

Figure A.4: The size of the two pulses emitted by Bessel and Gaussian apertures as a function of time.

APPENDIX B

Shape of Emitted Pulse

The wave function describing the longitudinal electric field (E_z) of the X wave is [13]

$$\chi(\rho, z, t) = \int_{-\infty}^{\infty} F(k_0) J_0\left(k_0 \sin\theta_2 \rho\right) e^{jk_0(ct - \cos\theta_2 z)} dk_0. \tag{B.1}$$

If the spectrum $F(k_0)$ is assumed to be uniform for wavenumbers in the interval $(k_{0,\min}, k_{0,\max})$ and zero otherwise, the wave function of the ideal X wave at $t = 0$ becomes

$$\chi^{\text{id}}(\rho, z) = \int_{k_{0,\min}}^{k_{0,\max}} J_0\left(k_0 \sin\theta_2 \rho\right) e^{-jk_0 \cos\theta_2 z} dk_0. \tag{B.2}$$

The intensity of the ideal X wave $|\chi^{\text{id}}(\rho, z)|^2$ for $(k_{0,\min}, k_{0,\max}) = (0, 2\pi\, 29\text{GHz}/c)$ is plotted along the $y = 0$ plane in Fig. B.1(a). The X wave is centered around $z = 0.35$ m and has $\theta_2 = 23^\circ$ to be comparable to the measured X wave which is presented later. The ideal X wave exhibits the expected X shape.

In Fig. B.1(b), the intensity of an X wave limited to the

$$(k_{0,\min}, k_{0,\max}) = (2\pi\, 19\text{GHz}/c, 2\pi\, 29\text{GHz}/c) \tag{B.3}$$

range is shown. This range corresponds to the experimentally measured bandwidth of the Bessel beam radiator. Simply by limiting the lower frequency of the X wave, a significantly different shape is observed. The longitudinal extent of the X wave has broadened due to the limited bandwidth, and the characteristic X signature is no longer visible.

As shown in [73], dispersion degrades the confinement of X waves. In the current framework, dispersion describes the dependence of the axicon angle, θ_2, on frequency. The axicon angle of the Bessel beam radiator, based on measured data along the $z = 0.325$ m plane (Fig. 4(e-h) of main text), is presented in Fig. B.1(c). Only a $\sim 2^\circ$ variation in the axicon angle is observed within the bandwidth of operation. As a result, the radiator exhibits very little dispersion. Incorporating dispersion into the expression for the X wave yields the wave function

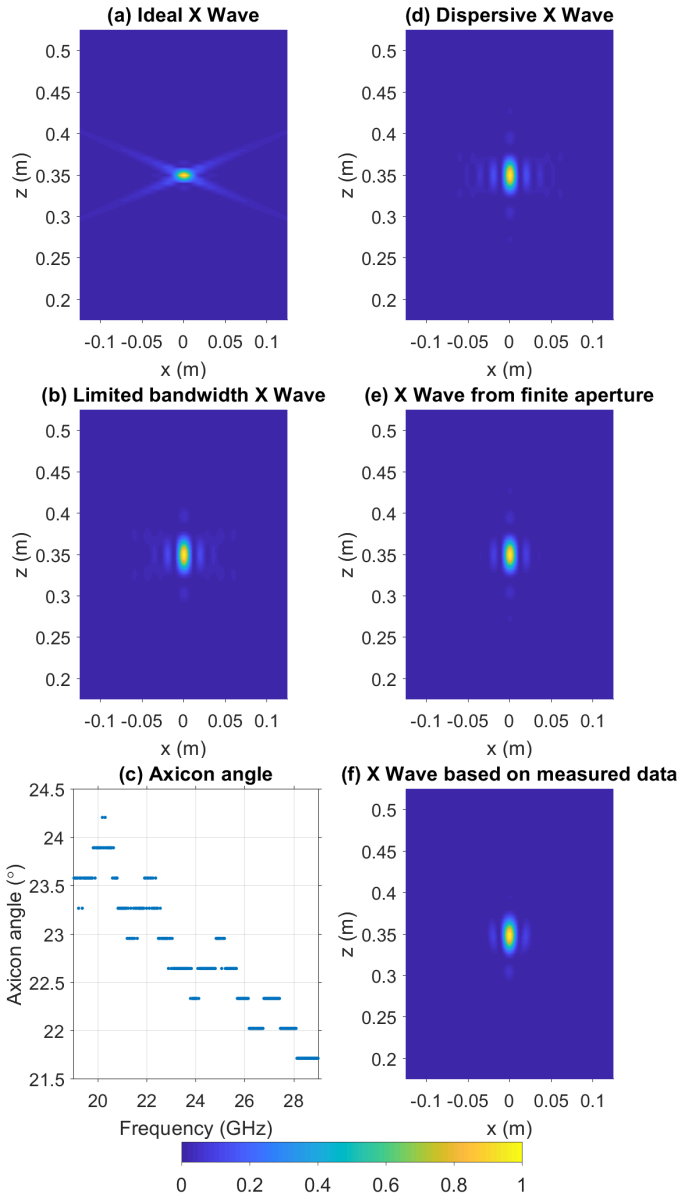

Figure B.1: (a) Ideal X wave with $\theta_2 = 23°$ (0 - 29 GHz), (b) X wave with limited bandwidth (19 - 29 GHz), (c) axicon angle of Bessel beam radiator as a function of frequency, (d) X wave produced by an an aperture exhibiting the dispersion of the Bessel beam radiator, (e) X wave produced by a Gaussian aperture with $\Delta\rho = 33$ mm, and (f) X wave calculated using the experimentally captured data. All X waves are plotted along the $y = 0$ plane.

$$\chi^{\text{dis}}(\rho, z) = \int_{k_{0,\min}}^{k_{0,\max}} J_0\left(k_0 \sin\theta_2(k_0)\rho\right) e^{-jk_0\cos\theta_2(k_0)z} dk_0. \tag{B.4}$$

Using the dispersion function in Fig. B.1(c), the intensity of a dispersive, bandwidth limited X wave is plotted in Fig. B.1(d). Due to the minimal dispersion exhibited by the Bessel beam radiator, the difference between the dispersionless (Fig. B.1(b)) and dispersive (Fig. B.1(d)) X waves is insignificant.

So far in (B.1)-(B.4), only X waves produced by infinite apertures have been examined. In reality, the radiating aperture is finite. Such an aperture produces Bessel beams over a finite region, which reduces the transversal extent of the X wave. This can be approximated mathematically by assuming a Gaussian apodization function

$$\chi^{\text{fin}}(\rho, z) = \int_{k_{0,\min}}^{k_{0,\max}} J_0\left(k_0 \sin\theta_2(k_0)\rho\right) e^{-\rho^2/(2\Delta\rho^2)} e^{-jk_0\cos\theta_2(k_0)z} dk_0. \tag{B.5}$$

The intensity of the X wave produced by a finite aperture with $\Delta\rho = 33$ mm is depicted in Fig. B.1(e). The transversal extent has been significantly reduced compared to the X wave of Fig. B.1(d). However, the region of higher intensity close to the z-axis is unaffected, resulting in a more bulletlike pulse.

The evolution of the X wave using the experimentally measured E_z along the $y = 0$ plane is calculated as

$$E_z(\rho, z, t) = \sum_{i=1}^{N_f} E_z(\rho, z, \omega_i) e^{j\omega_i t}, \tag{B.6}$$

where $\omega_1 = 2\pi\, 19$ GHz and $\omega_{N_f} = 2\pi\, 29$ GHz. The intensity of the X wave (computed using the experimental data) is shown in Fig. B.1(f). The similarity between the dispersive, bandwidth limited X wave emitted from a finite aperture in Fig. B.1(e) and the one based on measured data in Fig. B.1(f) is evident.

APPENDIX C

Time Domain Measurements

Time domain measurements of the Bessel beam radiator based on refractive optics were performed at the U.S. Naval Research Laboratory (NRL) by Scott Rudolph and Victor Mendez.

A block diagram of the experimental setup that is used for these measurements is presented in Fig. C.1(a). An arbitrary waveform generator (AWG) creates a sub-nanosecond pulse with a 7 GHz bandwidth, centered around 5.5 GHz. The output of the AWG is fed into the intermediate frequency (IF) port of a triple balanced mixer. A signal generator is used at the local oscillator (LO) port of the mixer, providing it with a 20 GHz LO frequency. The signal generator's sync signal serves as the trigger for the AWG. The mixer's output goes through a section of WR28 waveguide which acts as a bandpass filter (21.081-42.154 GHz). The output of the waveguide goes through a 10 dB directional coupler and a low noise amplifier (LNA). The signal at output of the LNA excites the Bessel beam radiator.

The signal generated by the Bessel beam radiator is received by a coaxial probe mounted on a 3D positioner, as shown in Fig. C.1(b). The probe is moved within a 0.25 x 0.25 x 0.35 m^3 volume in increments of 2.5 mm in the x- and y-directions and in increments of 5 mm in the z-direction. Absorbing material covers the base of the probe to reduce the scattering it causes.

The signal that serves as the input to the LNA and the signal received on the probe are captured on the oscilloscope at multiple points along the $y = 0$ plane. The transfer function at each of these points is calculated by dividing the Fourier transform of the output signal at that point with the Fourier transform of the corresponding input signal. The frequency spectrum of the sub-nanosecond pulse presented in the main text is then multiplied with the transfer function of each point. This yields the frequency domain spectrum at each point when the radiator is excited by a uniform spectrum pulse. An inverse Fourier transform is applied to this spectrum, resulting in the time domain response at each point along the $y = 0$ plane.

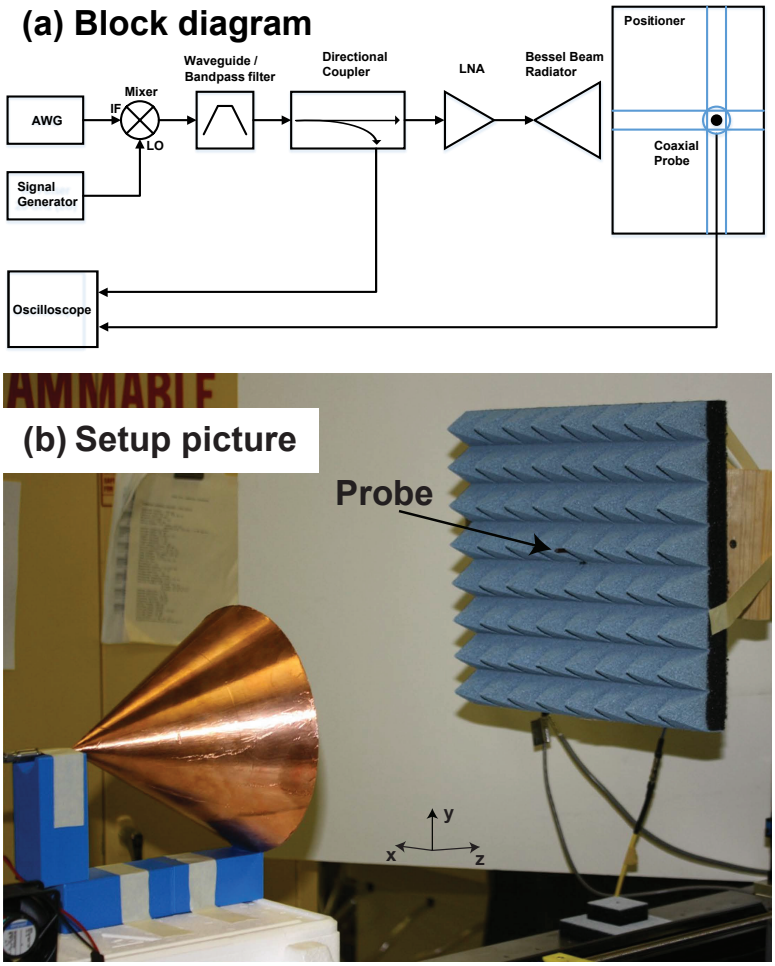

Figure C.1: Measurement setup used to obtain the time domain results presented in the main text: (a) the block diagram, and (b) a picture of the radiator and the coaxial probe mounted on the translation stage.

APPENDIX D

Mathematical Quantities

The D quantities in (5.39) are

$$D_n^{\mathrm{I}} = \frac{j\eta_0}{2k_0}\left(k_0^2 - k_{x,n}^2\right)\sum_u \frac{e^{-(G_{nu}+jk_z)r_x}}{d\,G_{nu}}$$

$$D_{nu}^{\mathrm{II}} = \frac{j\eta_0}{2k_0}k_{x,n}k_{y,u}\frac{e^{-(G_{nu}+jk_z)r_x}}{l\,G_{nu}}$$

$$D_{ns}^{\mathrm{III}} = \frac{j\eta_0}{2k_0}\sum_u \left[lk_0^2 - lk_{3,s}^2 - dk_{3,s}\left(2\pi\frac{u}{t} + k_3'\right)\right]$$

$$\frac{e^{-(G'_{su}+jk_z)r_x}}{t\,h\,G'_{su}}\mathrm{sinc}\left(s\frac{l^2}{h^2} + u - n\right)$$

$$D_g^{\mathrm{IV}} = \frac{j\eta_0}{2k_0}\left(k_0^2 - k_{y,g}^2\right)\sum_s \frac{e^{-(G_{sp}+jk_z)r_y}}{l\,G_{sg}}$$

$$D_{gs}^{\mathrm{V}} = \frac{j\eta_0}{2k_0}k_{y,g}k_{x,s}\frac{e^{-(G_{sg}+jk_z)r_y}}{d\,G_{sg}}$$

$$D_{gu}^{\mathrm{VI}} = \frac{j\eta_0}{2k_0}\sum_s \left[dk_0^2 - dk_{3,u}^2 + lk_{3,u}\left(2\pi\frac{s}{t} + k_3'\right)\right]$$

$$\frac{e^{-(G'_{us}+jk_z)r_y}}{t\,h\,G'_{us}}\mathrm{sinc}\left(u\frac{d^2}{h^2} - s - g\right)$$

$$D_b^{\mathrm{VII}} = \frac{j\eta_0}{2k_0}\left(k_0^2 - k_{3,b}^2\right)\sum_u \frac{e^{-(G'_{bu}+jk_z)r_3}}{t\,G'_{bu}}$$

$$D_{bs}^{\mathrm{VIII}} = \frac{j\eta_0}{2k_0}\sum_u \left(lk_0^2 - lk_{x,s}^2 - dk_{x,s}k_{y,u}\right)$$

$$\frac{e^{-(G_{su}+jk_z)r_3}}{d\,h\,G_{su}}\mathrm{sinc}\left(s\frac{h^2}{l^2} + u - b\right)$$

$$D_{bu}^{\mathrm{IX}} = \frac{j\eta_0}{2k_0} \sum_s \left(dk_0^2 - dk_{y,u}^2 - lk_{x,s}k_{y,u} \right)$$

$$\frac{e^{-(G_{su}+jk_z)r_3}}{l\,h\,G_{su}} \mathrm{sinc}\left(s\frac{h^2}{l^2} + u - b \right)$$

$$G_{su} = \sqrt{k_{x,s}^2 + k_{y,u}^2 - k_0^2}$$

$$G'_{su} = \sqrt{k_{3,s}^2 + (2\pi u/t + k'_3)^2 - k_0^2}$$

BIBLIOGRAPHY

[1] J. L. Volakis, C.-C. Chen, and K. Fujimoto, *Small antennas: miniaturization techniques & applications*. McGraw-Hill New York, 2010, vol. 1.

[2] R. C. Hansen, *Electrically small, superdirective, and superconducting antennas*. John Wiley & Sons, 2006.

[3] S. R. Best and A. D. Yaghjian, "The lower bounds on Q for lossy electric and magnetic dipole antennas," *IEEE Antennas and Wireless Propagation Letters*, vol. 3, no. 1, pp. 314–316, 2004.

[4] A. D. Yaghjian and S. R. Best, "Impedance, bandwidth, and Q of antennas," *IEEE Transactions on Antennas and Propagation*, vol. 53, no. 4, pp. 1298–1324, 2005.

[5] L. J. Chu, "Physical limitations of omni-directional antennas," *Journal of applied physics*, vol. 19, no. 12, pp. 1163–1175, 1948.

[6] A. Nordrum *et al.*, "Popular Internet of Things Forecast of 50 Billion Devices by 2020 Is Outdated," *IEEE Spectrum*, vol. 18, 2016.

[7] Y. Chen, N. Chiotellis, L.-X. Chuo, C. Pfeiffer, Y. Shi, R. G. Dreslinski, A. Grbic, T. Mudge, D. D. Wentzloff, D. Blaauw *et al.*, "Energy-autonomous wireless communication for millimeter-scale Internet-of-Things sensor nodes," *IEEE Journal on Selected Areas in Communications*, vol. 34, no. 12, pp. 3962–3977, 2016.

[8] L.-X. Chuo, Y. Shi, Z. Luo, N. Chiotellis, Z. Foo, G. Kim, Y. Kim, A. Grbic, D. Wentzloff, H.-S. Kim *et al.*, "7.4 A 915MHz asymmetric radio using Q-enhanced amplifier for a fully integrated $3\times3\times3\text{mm}^3$ wireless sensor node with 20m non-line-of-sight communication," in *2017 IEEE International Solid-State Circuits Conference (ISSCC)*. IEEE, 2017, pp. 132–133.

[9] M. Cho, S. Oh, S. Jeong, Y. Zhang, I. Lee, Y. Kim, L.-X. Chuo, D. Kim, Q. Dong, Y.-P. Chen *et al.*, "A $6\times5\times4\text{mm}^3$ general purpose audio sensor node with a 4.7 μW audio processing IC," in *2017 Symposium on VLSI Circuits*. IEEE, 2017, pp. C312–C313.

[10] T. Jang, G. Kim, B. Kempke, M. B. Henry, N. Chiotellis, C. Pfeiffer, D. Kim, Y. Kim, Z. Foo, H. Kim *et al.*, "Circuit and system designs of ultra-low power sensor nodes with illustration in a miniaturized GNSS logger for position tracking: Part I-Analog

circuit techniques," *IEEE Transactions on Circuits and Systems I: Regular Papers*, vol. 64, no. 9, pp. 2237–2249, 2017.

[11] ——, "Circuit and system designs of ultra-low power sensor nodes with illustration in a miniaturized GNSS logger for position tracking: Part II-Data communication, energy harvesting, power management, and digital circuits," *IEEE Transactions on Circuits and Systems I: Regular Papers*, vol. 64, no. 9, pp. 2250–2262, 2017.

[12] H. Kim, N. Chiotellis, E. Ansari, M. Faisal, T. Jang, A. Grbic, H.-S. Kim, D. Blaauw, and D. Wentzloff, "A receiver/antenna co-design for a 1.5mJ per fix fully-integrated $10\times10\times6\text{mm}^3$ GPS logger," in *2018 IEEE Custom Integrated Circuits Conference (CICC)*. IEEE, 2018, pp. 1–4.

[13] H. E. Hernández-Figueroa, M. Zamboni-Rached, and E. Recami, *Localized waves*. John Wiley & Sons, 2007, vol. 194.

[14] J. N. Brittingham, "Focus waves modes in homogeneous Maxwell's equations: Transverse electric mode," *Journal of Applied Physics*, vol. 54, no. 3, pp. 1179–1189, 1983.

[15] R. W. Ziolkowski, "Localized transmission of electromagnetic energy," *Physical Review A*, vol. 39, no. 4, p. 2005, 1989.

[16] T. T. Wu, "Electromagnetic missiles," *Journal of Applied Physics*, vol. 57, no. 7, pp. 2370–2373, 1985.

[17] H. E. Moses and R. T. Prosser, "Acoustic and electromagnetic bullets: derivation of new exact solutions of the acoustic and maxwell's equations," *SIAM Journal on Applied Mathematics*, vol. 50, no. 5, pp. 1325–1340, 1990.

[18] J. Durnin, "Exact solutions for nondiffracting beams. I. The scalar theory," *JOSA A*, vol. 4, no. 4, pp. 651–654, 1987.

[19] S. Monk, J. Arlt, D. Robertson, J. Courtial, and M. Padgett, "The generation of Bessel beams at millimetre-wave frequencies by use of an axicon," *Optics Communications*, vol. 170, no. 4, pp. 213–215, 1999.

[20] M. Ettorre and A. Grbic, "Generation of propagating Bessel beams using leaky-wave modes," *IEEE Transactions on Antennas and Propagation*, vol. 60, no. 8, pp. 3605–3613, 2012.

[21] M. Ettorre, S. M. Rudolph, and A. Grbic, "Generation of propagating Bessel beams using leaky-wave modes: Experimental validation," *IEEE Transactions on Antennas and Propagation*, vol. 60, no. 6, pp. 2645–2653, 2012.

[22] C. Pfeiffer and A. Grbic, "Controlling vector Bessel beams with metasurfaces," *Physical Review Applied*, vol. 2, no. 4, p. 044012, 2014.

[23] M. Q. Qi, W. X. Tang, and T. J. Cui, "A broadband Bessel beam launcher using metamaterial lens," *Scientific reports*, vol. 5, 2015.

[24] G. Scott and N. McArdle, "Efficient generation of nearly diffraction-free beams using an axicon," *Optical Engineering*, vol. 31, no. 12, pp. 2640–2643, 1992.

[25] F. Aieta, P. Genevet, M. A. Kats, N. Yu, R. Blanchard, Z. Gaburro, and F. Capasso, "Aberration-free ultrathin flat lenses and axicons at telecom wavelengths based on plasmonic metasurfaces," *Nano Letters*, vol. 12, no. 9, pp. 4932–4936, 2012.

[26] W. Williams and J. Pendry, "Generating Bessel beams by use of localized modes," *JOSA A*, vol. 22, no. 5, pp. 992–997, 2005.

[27] J. Turunen, A. Vasara, and A. T. Friberg, "Holographic generation of diffraction-free beams," *Applied Optics*, vol. 27, no. 19, pp. 3959–3962, 1988.

[28] J.-Y. Lu and J. F. Greenleaf, "Diffraction-limited beams and their applications for ultrasonic imaging and tissue characterization," in *San Diego '92*. International Society for Optics and Photonics, 1992, pp. 92–119.

[29] C. Pfeiffer and A. Grbic, "Generating stable tractor beams with dielectric metasurfaces," *Physical Review B*, vol. 91, no. 11, p. 115408, 2015.

[30] V. Grillo, J. Harris, G. C. Gazzadi, R. Balboni, E. Mafakheri, M. R. Dennis, S. Frabboni, R. W. Boyd, and E. Karimi, "Generation and application of Bessel beams in electron microscopy," *Ultramicroscopy*, vol. 166, pp. 48–60, 2016.

[31] A. Marcinkevičius, S. Juodkazis, S. Matsuo, V. Mizeikis, and H. Misawa, "Application of Bessel beams for microfabrication of dielectrics by femtosecond laser," *Japanese Journal of Applied Physics*, vol. 40, no. 11A, p. L1197, 2001.

[32] R. Li, K. F. Ren, X. E. Han, Z. Wu, L. Guo, and S. Gong, "Analysis of radiation pressure force exerted on a biological cell induced by high-order Bessel beams using Debye series," *Journal of Quantitative Spectroscopy and Radiative Transfer*, vol. 126, pp. 69–77, 2013.

[33] J.-Y. Lu and S. He, "Optical X wave communications," *Optics Communications*, vol. 161, no. 4, pp. 187–192, 1999.

[34] N. Chiotellis and A. Grbic, "A broadband, Bessel beam radiator," in *2016 IEEE International Symposium on Antennas and Propagation (APSURSI)*. IEEE, 2016, pp. 873–874.

[35] N. Chiotellis, V. Mendez, S. M. Rudolph, and A. Grbic, "Experimental demonstration of highly localized pulses (x waves) at microwave frequencies," *Physical Review B*, vol. 97, no. 8, p. 085136, 2018.

[36] N. Chiotellis and A. Grbic, "Metamaterial Bessel beam radiator," in *2017 IEEE International Symposium on Antennas and Propagation (APSURSI)*. IEEE, 2017, pp. 1735–1736.

[37] ——, "Metamaterial-based Bessel beam launcher," in *2017 11th International Congress on Engineered Materials Platforms for Novel Wave Phenomena (Metamaterials)*. IEEE, 2017, pp. 55–57.

[38] J.-Y. Lu and J. F. Greenleaf, "Nondiffracting X waves-exact solutions to free-space scalar wave equation and their finite aperture realizations," *IEEE Transactions on Ultrasonics, Ferroelectrics, and Frequency Control*, vol. 39, no. 1, pp. 19–31, 1992.

[39] A. V. Kildishev, A. Boltasseva, and V. M. Shalaev, "Planar photonics with metasurfaces," *Science*, vol. 339, no. 6125, p. 1232009, 2013.

[40] N. Yu and F. Capasso, "Flat optics with designer metasurfaces," *Nature Materials*, vol. 13, no. 2, pp. 139–150, 2014.

[41] X. Ni, A. V. Kildishev, and V. M. Shalaev, "Metasurface holograms for visible light," *Nature Communications*, vol. 4, 2013.

[42] B. H. Fong, J. S. Colburn, J. J. Ottusch, J. L. Visher, and D. F. Sievenpiper, "Scalar and tensor holographic artificial impedance surfaces," *IEEE Transactions on Antennas and Propagation*, vol. 58, no. 10, pp. 3212–3221, 2010.

[43] Y. Zhao and A. Alù, "Manipulating light polarization with ultrathin plasmonic metasurfaces," *Physical Review B*, vol. 84, no. 20, p. 205428, 2011.

[44] Z. Jakšić, S. Vuković, J. Matovic, and D. Tanasković, "Negative refractive index metasurfaces for enhanced biosensing," *Materials*, vol. 4, no. 1, pp. 1–36, 2010.

[45] C. Jansen, I. A. Al-Naib, N. Born, and M. Koch, "Terahertz metasurfaces with high Q-factors," *Applied Physics Letters*, vol. 98, no. 5, p. 051109, 2011.

[46] P.-Y. Chen and A. Alù, "Mantle cloaking using thin patterned metasurfaces," *Physical Review B*, vol. 84, no. 20, p. 205110, 2011.

[47] M. Selvanayagam and G. Eleftheriades, "Polarization control using tensor Huygens surfaces," *IEEE Transactions on Antennas and Propagation*, vol. 62, no. 12, pp. 6155–6168, 2014.

[48] D. Sjoberg and A. Ericsson, "A multi layer meander line circular polarization selective structure (MLML-CPSS)," in *2014 8th European Conference on Antennas and Propagation (EuCAP)*. IEEE, 2014, pp. 464–468.

[49] M. Bosiljevac, M. Casaletti, F. Caminita, Z. Sipus, and S. Maci, "Non-uniform metasurface Luneburg lens antenna design," *IEEE Transactions on Antennas and Propagation*, vol. 60, no. 9, pp. 4065–4073, 2012.

[50] G. Minatti, S. Maci, P. De Vita, A. Freni, and M. Sabbadini, "A circularly-polarized isoflux antenna based on anisotropic metasurface," *IEEE Transactions on Antennas and Propagation*, vol. 60, no. 11, pp. 4998–5009, 2012.

[51] N. Landy, S. Sajuyigbe, J. Mock, D. Smith, and W. Padilla, "Perfect metamaterial absorber," *Physical Review Letters*, vol. 100, no. 20, p. 207402, 2008.

[52] C. Pfeiffer and A. Grbic, "Cascaded metasurfaces for complete phase and polarization control," *Applied Physics Letters*, vol. 102, no. 23, p. 231116, 2013.

[53] ——, "Bianisotropic metasurfaces for optimal polarization control: Analysis and synthesis," *Physical Review Applied*, vol. 2, no. 4, p. 044011, 2014.

[54] ——, "Planar lens antennas of subwavelength thickness: Collimating leaky-waves with metasurfaces," *IEEE Transactions on Antennas and Propagation*, vol. 63, no. 7, pp. 3248–3253, 2015.

[55] N. Chiotellis and A. Grbic, "Analytical modeling of tensor metasurfaces," *JOSA B*, vol. 33, no. 2, pp. A51–A60, 2016.

[56] *Overview of the Internet of Things*, ITU-T Std. Y.2060, June 2012.

[57] C. A. Balanis, *Antenna Theory: Analysis and Design*. John Wiley & Sons, 2016.

[58] C. Pfeiffer, "Fundamental efficiency limits for small metallic antennas," *IEEE Transactions on Antennas and Propagation*, vol. 65, no. 4, pp. 1642–1650, 2017.

[59] D. Choudhury, "3D integration technologies for emerging microsystems," in *Microwave Symposium Digest (MTT), 2010 IEEE MTT-S International*. IEEE, 2010, pp. 1–4.

[60] T. Tsukiji and S. Tou, "On polygonal loop antennas," *IEEE Transactions on Antennas and Propagation*, vol. 28, pp. 571–575, 1980.

[61] I. Steiner, C. Bürgi, S. Werffeli, G. Dell'Omo, P. Valenti, G. Tröster, D. P. Wolfer, and H.-P. Lipp, "A GPS logger and software for analysis of homing in pigeons and small mammals," *Physiology & Behavior*, vol. 71, no. 5, pp. 589–596, 2000.

[62] i-Blue 747 GPS data logger. [Online]. Available: http://www.gvglobaltech.com/747spec.html

[63] W. McKinzie, "A modified Wheeler cap method for measuring antenna efficiency," in *1997 IEEE Antennas and Propagation Society International Symposium, 1997 Digest*, vol. 1. IEEE, 1997, pp. 542–545.

[64] *Propagation data and prediction methods for the planning of indoor radiocommunication systems and radio local area networks in the frequency range 300 MHz to 100 GHz*, ITU-R Std. P.1238-9, 2015.

[65] D. Micheli, A. Delfini, F. Santoni, F. Volpini, and M. Marchetti, "Measurement of electromagnetic field attenuation by building walls in the mobile phone and satellite navigation frequency bands," *IEEE Antennas and Wireless Propagation Letters*, vol. 14, pp. 698–702, 2015.

[66] M. Farwell, J. Ross, R. Luttrell, D. Cohen, W. Chin, and T. Dogaru, "Sense through the wall system development and design considerations," *Journal of the Franklin Institute*, vol. 345, no. 6, pp. 570–591, 2008.

[67] C. D. Taylor, S. J. Gutierrez, S. L. Langdon, K. L. Murphy, and W. A. Walton, "Measurement of RF propagation into concrete structures over the frequency range 100 MHz to 3 GHz," in *Wireless Personal Communications*. Springer, 1997, pp. 131–144.

[68] J. L. Bohorquez, A. P. Chandrakasan, and J. L. Dawson, "A 350μW CMOS MSK transmitter and 400μW OOK super-regenerative receiver for medical implant communications," *IEEE Journal of Solid-State Circuits*, vol. 44, no. 4, pp. 1248–1259, 2009.

[69] K. R. Sadagopan, J. Kang, S. Jain, Y. Ramadass, and A. Natarajan, "A 365nW -61.5 dBm sensitivity, 1.875 cm^2 2.4 GHz wake-up receiver with rectifier-antenna co-design for passive gain," in *2017 IEEE Radio Frequency Integrated Circuits Symposium (RFIC)*. IEEE, 2017, pp. 180–183.

[70] H. Jiang, P.-H. P. Wang, L. Gao, P. Sen, Y.-H. Kim, G. M. Rebeiz, D. A. Hall, and P. P. Mercier, "24.5 A 4.5 nW wake-up radio with -69dBm sensitivity," in *2017 IEEE International Solid-State Circuits Conference (ISSCC)*. IEEE, 2017, pp. 416–417.

[71] P. Saari and K. Reivelt, "Evidence of X-shaped propagation-invariant localized light waves," *Physical Review Letters*, vol. 79, no. 21, p. 4135, 1997.

[72] P. Bowlan, H. Valtna-Lukner, M. Lõhmus, P. Piksarv, P. Saari, and R. Trebino, "Measuring the spatiotemporal field of ultrashort Bessel-X pulses," *Optics Letters*, vol. 34, no. 15, pp. 2276–2278, 2009.

[73] W. Fuscaldo, S. C. Pavone, G. Valerio, A. Galli, M. Albani, and M. Ettorre, "Analysis of limited-diffractive and limited-dispersive X-waves generated by finite radial waveguides," *Journal of Applied Physics*, vol. 119, no. 19, p. 194903, 2016.

[74] D. Mugnai, A. Ranfagni, and R. Ruggeri, "Observation of superluminal behaviors in wave propagation," *Physical Review Letters*, vol. 84, no. 21, p. 4830, 2000.

[75] B. Allen, M. Dohler, E. Okon, W. Malik, A. Brown, and D. Edwards, *Ultra wideband antennas and propagation for communications, radar and imaging*. John Wiley & Sons, 2006.

[76] K. Stephan, J. Mead, D. Pozar, L. Wang, and J. Pearce, "A near field focused microstrip array for a radiometric temperature sensor," *IEEE Transactions on Antennas and Propagation*, vol. 55, no. 4, pp. 1199–1203, 2007.

[77] V. Chawla and D. S. Ha, "An overview of passive RFID," *IEEE Communications Magazine*, vol. 45, no. 9, pp. 11–17, 2007.

[78] S. Karimkashi and A. A. Kishk, "Focused microstrip array antenna using a Dolph-Chebyshev near-field design," *IEEE Transactions on Antennas and Propagation*, vol. 57, no. 12, pp. 3813–3820, 2009.

[79] D. Comite, W. Fuscaldo, S. Podilchak, V. Gómez-Guillamón Buendía, P. Hilario Re, P. Baccarelli, P. Burghignoli, and A. Galli, "Microwave generation of x-waves by means of a planar leaky-wave antenna," *Applied Physics Letters*, vol. 113, no. 14, p. 144102, 2018.

[80] J.-Y. Lu and J. F. Greenleaf, "Ultrasonic nondiffracting transducer for medical imaging," *IEEE Transactions on Ultrasonics, Ferroelectrics, and Frequency Control*, vol. 37, no. 5, pp. 438–447, 1990.

[81] J. Y. Lu and J. F. Greenleaf, "Evaluation of a nondiffracting transducer for tissue characterization," in *IEEE Symposium on Ultrasonics*. IEEE, Dec 1990, pp. 795–798 vol.2.

[82] J.-Y. Lu and J. F. Greenleaf, "Producing deep depth of field and depth-independent resolution in nde with limited diffraction beams," *Ultrasonic Imaging*, vol. 15, no. 2, pp. 134–149, 1993.

[83] A. M. Shaarawi, I. M. Besieris, and T. M. Said, "Temporal focusing by use of composite x waves," *JOSA A*, vol. 20, no. 8, pp. 1658–1665, 2003.

[84] J. M. Osepchuk, "A history of microwave heating applications," *IEEE Transactions on Microwave Theory and Techniques*, vol. 32, no. 9, pp. 1200–1224, 1984.

[85] F. Sterzer, "Microwave medical devices," *IEEE Microwave Magazine*, vol. 3, no. 1, pp. 65–70, 2002.

[86] C. Gao, T. Wei, F. Duewer, Y. Lu, and X.-D. Xiang, "High spatial resolution quantitative microwave impedance microscopy by a scanning tip microwave near-field microscope," *Applied Physics Letters*, vol. 71, no. 13, pp. 1872–1874, 1997.

[87] M. G. Backstrom and K. G. Lovstrand, "Susceptibility of electronic systems to high-power microwaves: Summary of test experience," *IEEE Transactions on Electromagnetic Compatibility*, vol. 46, no. 3, pp. 396–403, 2004.

[88] D. J. Daniels, "Ground penetrating radar," *Encyclopedia of RF and Microwave Engineering*, 2005.

[89] W. Fuscaldo, D. Comite, A. Boesso, P. Baccarelli, P. Burghignoli, and A. Galli, "Focusing leaky waves: A class of electromagnetic localized waves with complex spectra," *Physical Review Applied*, vol. 9, p. 054005, May 2018.

[90] J. B. Pendry, D. Schurig, and D. R. Smith, "Controlling electromagnetic fields," *Science*, vol. 312, no. 5781, pp. 1780–1782, 2006.

[91] J. Li and J. B. Pendry, "Hiding under the carpet: a new strategy for cloaking," *Physical Review Letters*, vol. 101, no. 20, p. 203901, 2008.

[92] M. Ebrahimpouri and O. Quevedo-Teruel, "Bespoke lenses based on quasi-conformal transformation optics technique," *IEEE Transactions on Antennas and Propagation*, vol. 65, no. 5, pp. 2256–2264, 2017.

[93] C. R. Garcia, J. Correa, D. Espalin, J. H. Barton, R. C. Rumpf, R. Wicker, and V. Gonzalez, "3d printing of anisotropic metamaterials," *Progress In Electromagnetics Research*, vol. 34, pp. 75–82, 2012.

[94] R. C. Rumpf, J. Pazos, C. R. Garcia, L. Ochoa, and R. Wicker, "3d printed lattices with spatially variant self-collimation," *Progress in Electromagnetics Research*, vol. 139, pp. 1–14, 2013.

[95] D. Isakov, Q. Lei, F. Castles, C. Stevens, C. Grovenor, and P. Grant, "3d printed anisotropic dielectric composite with meta-material features," *Materials & Design*, vol. 93, pp. 423–430, 2016.

[96] D. M. Pozar, *Microwave Engineering*. John Wiley & Sons, 2012.

[97] Dielectric parts for easy RF-prototyping — PREPERM®. [Online]. Available: https://www.preperm.com/products/stock-shapes/#filaments

[98] B. A. Munk, *Frequency selective surfaces: theory and design*. John Wiley & Sons, 2005.

[99] O. Luukkonen, C. Simovski, G. Granet, G. Goussetis, D. Lioubtchenko, A. V. Räisänen, and S. Tretyakov, "Simple and accurate analytical model of planar grids and high-impedance surfaces comprising metal strips or patches," *Antennas and Propagation, IEEE Transactions on*, vol. 56, no. 6, pp. 1624–1632, 2008.

[100] C. Simovski, S. Zouhdi, and V. Yatsenko, "Electromagnetic interaction in dipole grids and prospective high-impedance surfaces," *Radio Science*, vol. 40, no. 5, 2005.

[101] I. Anderson, "On the theory of self-resonant grids," *Bell System Technical Journal*, vol. 54, no. 10, pp. 1725–1731, 1975.

[102] A. J. Viitanen, I. Hänninen, and S. A. Tretyakov, "Analytical model for regular dense arrays of planar dipole scatterers," *Progress In Electromagnetics Research*, vol. 38, pp. 97–110, 2002.

[103] M. Selvanayagam and G. V. Eleftheriades, "Transmission-line metamaterials on a skewed lattice for transformation electromagnetics," *Microwave Theory and Techniques, IEEE Transactions on*, vol. 59, no. 12, pp. 3272–3282, 2011.

[104] D.-H. Kwon and C. D. Emiroglu, "Non-orthogonal grids in two-dimensional transmission-line metamaterials," *IEEE Transactions on Antennas and Propagation*, vol. 60, no. 9, pp. 4210–4218, 2012.

[105] T. A. Morgado, J. S. Marcos, S. I. Maslovski, and M. G. Silveirinha, "Negative refraction and partial focusing with a crossed wire mesh: Physical insights and experimental verification," *Applied Physics Letters*, vol. 101, no. 2, p. 021104, 2012.

[106] M. Kontorovich and V. Akimov, "Average boundary conditions on the surface of a planar wire mesh with oblique cells," *Radio Engineering and Electronic Physics*, vol. 22, pp. 22–31, 1977.

[107] S. Tretyakov, *Analytical modeling in applied electromagnetics*. Artech House, 2003.

[108] L. B. Felsen and N. Marcuvitz, *Radiation and scattering of waves*. John Wiley & Sons, 1994.

[109] D. A. Hill and J. R. Wait, "Electromagnetic scattering of an arbitrary plane wave by two nonintersecting perpendicular wire grids," *Canadian Journal of Physics*, vol. 52, no. 3, pp. 227–237, 1974.

[110] ——, "Electromagnetic scattering of an arbitrary plane wave by a wire mesh with bonded junctions," *Canadian Journal of Physics*, vol. 54, no. 4, pp. 353–361, 1976.

[111] R. W. P. King and T. T. Wu, "Analysis of crossed wires in a plane-wave field," *IEEE Transactions on Electromagnetic Compatibility*, vol. 4, pp. 255–265, 1975.

[112] S. N. Samaddar, "Babinet's principle for an anisotropic resistive surface using different approaches," *Journal of Modern Optics*, vol. 33, no. 9, pp. 1177–1192, 1986.

[113] G. Gok and A. Grbic, "Tensor transmission-line metamaterials," *IEEE Transactions on Antennas and Propagation*, vol. 58, no. 5, pp. 1559–1566, 2010.

[114] A. M. Patel and A. Grbic, "Modeling and analysis of printed-circuit tensor impedance surfaces," *IEEE Transactions on Antennas and Propagation*, vol. 61, no. 1, pp. 211–220, 2013.

[115] G. Borgiotti, "Maximum power transfer between two planar apertures in the Fresnel zone," *IEEE Transactions on Antennas and Propagation*, vol. 14, no. 2, pp. 158–163, 1966.

[116] F. Alsolamy, W. Alomar, and A. Grbic, "Cylindrical vector beams for wireless power transfer," in *2017 IEEE International Symposium on Antennas and Propagation (APSURSI)*. IEEE, 2017, pp. 1297–1298.